# CHARACTERIZATION OF BACTERIA CAUSING ACUTE OTITIS MEDIA USING RAMAN SPECTROSCOPY

By

Oscar Daniel Ayala

Dissertation

Submitted to the Faculty of the

Graduate School of Vanderbilt University

in partial fulfillment of the requirements

for the degree of

DOCTOR OF PHILOSOPHY

in

Biomedical Engineering

May 10, 2019

Nashville, TN

Approved:

Anita Mahadevan-Jansen, Ph.D.

E. Duco Jansen, Ph.D.

Eric P. Skaar, Ph.D., MPH

Jay A. Werkhaven, M.D.

Melissa C. Skala, Ph.D.

## DEDICATION

*To my parents, Oscar and Amparo Ayala, who have forever supported me in my endeavors, taught me to never stop learning, and further motivated me with their breakfast tacos.*

*To my siblings, Arturo, Olivia, and Erika who provided me with countless words of wisdom.*

*To my nephews and nieces, Christopher A. Suárez, Gabriella Hernandez, and Alejandro A. Ayala who brightened my day with their smiles.*

*To my Godchildren, Roman Xavier Iglesias and Sebastian Ezekiel Iglesias, who always brought happiness through the most challenging days.*

*To my loving wife, Sujata Ghosh Ayala, who moved to Nashville in 2015 to start our marriage together, and always pushed me to be more than I am and supported me to pursue my dreams.*

## ACKNOWLEDGEMENTS

I would like to thank my dissertation advisor, Dr. Anita Mahadevan-Jansen, and Dr. E. Duco Jansen for giving me the opportunity to visit Vanderbilt University and tell my story during the recruiting process. They welcomed me to their labs and guided me to develop into the researcher and scientist that I am today. Through my tenure at Vanderbilt, Dr. Mahadevan-Jansen taught me the importance of growing a thick skin as a researcher; for this, I am very grateful. Dr. Jansen always reminded me to keep a perspective on my dissertation research and its broader impact for both the scientific and general communities. I would like to extend my appreciation to the rest of my dissertation committee: Drs. Eric P. Skaar, Jay A. Werkhaven, and Melissa Skala who were instrumental in the development of my dissertation research project. I would like thank Dr. Jay A. Werkhaven and his team of nurses and clinical staff that were just as excited as I was about my research and allowed me to evaluate the feasibility and practicality of my work at Monroe Carell Jr. Children's Hospital at Vanderbilt.

My research while at Vanderbilt would not have been possible without funding support of Vanderbilt's Institute of Clinical and Translatable Research (VICTR) program funded by the National Center for Advancing Translational Sciences and a National Institutes of Health (NIH) and a Department of Defense, Air Force of Scientific Research, National Defense Science and Engineering Graduate (NDSEG) Fellowship.

One thing I learned early on in graduate school through my mentors was that you cannot complete the journey alone. I would agree and here is my story. I am forever thankful to Dr. Alexander J. Makowski, a Ph.D. graduate student in Dr. Mahadevan-Jansen's lab at the time, who taught me the fundamentals of Raman microspectroscopy instrumentation and introduced me to Dr. Eric P. Skaar, a professor in pathology, microbiology, and immunology at Vanderbilt who would later become a member of my dissertation committee. Dr. Skaar connected me with his post-doc fellow Dr. Catherine A. Wakeman who I am thankful for as she taught me how to work with bacteria in the lab. As my dissertation further developed, Dr. Wakeman introduced me to Dr. Jennifer A. Gaddy, an assistant professor of medicine in infectious diseases at Vanderbilt, who opened her lab to me and connected me with Dr. Ryan A. Doster, a physician and graduate student in her lab to collaborate on using Raman spectroscopy to investigate biofilms. As I continued to work in her lab, Dr. Gaddy introduced me to Drs. Kevin Mason and Sheryl S. Justice at Nationwide Children's Hospital in Columbus, OH who opened their research lab to collaborate for investigating an established animal model for otitis media. I will treasure their friendship and the instrumental role they played along my graduate path.

I am forever thankful of the constant support and dedication from my lab mates during my graduate work. Drs. Isaac J. Pence and Christine O'Brien committed their time and patience to teach me the intricacies of Raman spectroscopy. Through their friendship and mentorship, we developed a support system we needed to succeed in graduate school.

My development as a researcher while at Vanderbilt would not be complete without Dayna E. Every, a visiting master's student, and Elly Shin, an undergraduate student at Vanderbilt University who I mentored as a graduate student. They helped me develop into a stronger scientist by learning to be a better scientific communicator.

I would also like to express my gratitude to Dr. Don Brunson for his invaluable advice and the many discussions we had on the challenges of succeeding in graduate school. Both Dr. Brunson and Michele Cedzich gave me the opportunity to share my story as the first in my family to pursue a Ph.D. by traveling to conferences to recruit underrepresented minorities and connect them with opportunities at Vanderbilt. The drive to further diversify the student experience at Vanderbilt enhanced my graduate school experience, and for that I am forever grateful.

I will be forever thankful for my dear friends and advisors that were instrumental in the founding of the first chapter of the Society for the Advancement of Chicanos/Hispanics and Native Americans in Science (SACNAS) in Tennessee and Elementary Engineering. The Vanderbilt SACNAS Chapter serves to connect students from all backgrounds and especially those from Chicano/Hispanic and Native American backgrounds and provide resources as they grow through graduate school. The Vanderbilt SACNAS Chapter has developed to serve students across the sciences, engineering, and medical fields. Elementary Engineering is a platform that connects elementary school kids with graduate students in the science, technology, engineering, and mathematics (STEM) fields

to teach kids scientific principles through hands-on learning. Elementary Engineering has grown to be an integral part of the biomedical engineering outreach program at Vanderbilt.

Lastly, I would like to thank Dr. Thomas E. Milner, my undergraduate research advisor at The University of Texas at Austin, who introduced me to Vanderbilt University and connected me with Drs. Anita Mahadevan-Jansen and E. Duco Jansen. His sincere mentorship not only helped me develop as researcher, but also guided my interest in pursuing my passion for clinical research.

TABLE OF CONTENTS

Page

**DEDICATION** ..... iii
**ACKNOWLEDGEMENTS** ..... iv
**LIST OF TABLES** ..... xii
**LIST OF FIGURES** ..... xiii
**CHAPTER**
1. INTRODUCTION ..... 1
1.1 Motivation and Objectives ..... 1
1.2 Specific Aims ..... 3
1.3 Summary of Chapters ..... 5
2. BACKGROUND ..... 7
2.1 The Problem: Acute Otitis Media ..... 7
2.2 The Ear ..... 11
2.2.1 The Outer Ear ..... 12
2.2.2 The Middle Ear ..... 14
2.2.3 Tympanic Membrane ..... 15
2.2.4 The Inner Ear ..... 16
2.3 Current Clinical Methods to Diagnose and Treat AOM ..... 17
2.3.1 Clinical Guidelines to Diagnose AOM ..... 17
2.3.2 Pneumatic Otoscopy ..... 18
2.3.3 Tympanometry ..... 19
2.3.4 Acoustic Reflectometry ..... 20
2.3.5 Tympanocentesis ..... 20
2.3.6 Standard Treatment Protocol ..... 21
2.4 Optical Methods to Diagnose OM ..... 22
2.4.1. Diffuse Reflectance ..... 22
2.4.2 Optical Coherence Tomography ..... 22
2.5 Optical Techniques to Identify Bacteria ..... 23
2.5.1 Fluorescence Spectroscopy ..... 23

2.5.2 Fourier Transform Infrared Spectroscopy (FT-IR Spectroscopy) ..... 23
2.5.3 Raman Spectroscopy and Raman Microspectroscopy ..... 24
2.6 The Clinical Need ..... 24
2.7 The Solution ..... 25
2.8 References ..... 27
3. CHARACTERIZATION OF BACTERIA CAUSING ACUTE OTITIS MEDIA USING RAMAN MICROSPECTROSCOPY ..... 32
3.1 Abstract ..... 32
3.2 Introduction ..... 33
3.3 Materials & Methods ..... 37
3.3.1 Selection of Agar Growth Media ..... 37
3.3.2 Bacterial Species ..... 38
3.3.3 Human Middle Ear Effusion Samples ..... 39
3.3.4 Raman Microspectroscopy ..... 39
3.3.5 Data Analysis ..... 41
3.4 Results ..... 42
3.5 Discussion ..... 50
3.6 Acknowledgements ..... 55
3.7 References ..... 56
4. DRUG-RESISTANT *STAPHYLOCOCCUS AUREUS* STRAINS REVEAL DISTINCT BIOCHEMICAL FEATURES WITH RAMAN MICROSPECTROSCOPY ..... 60
4.1 Abstract ..... 60
4.2 Introduction ..... 61
4.3 Materials & Methods ..... 66
4.3.1 Bacterial Strains ..... 66
4.3.2 Raman Microspectroscopy ..... 70
4.3.3 Spectral Data Analysis ..... 72
4.4 Results & Discussion ..... 74
4.4.1 RS can Differentiate Two Virulent Strains of Group B *Streptococcus* (GBS). ..... 74

4.4.2 Genetically Modified Strains of *S. aureus* are Distinguished from WT. ..... 77
4.4.3 Antibiotic-resistant *S. aureus* Strains can be Identified using RS. ..... 81
4.4.4 Small-colony Variants (SCVs) can be Distinguished from WT Newman Strain. ..... 89
4.5 Acknowledgements ..... 99
4.6 References ..... 100
5. RAMAN MICROSPECTROSCOPY DIFFERENTIATES PERINATAL PATHOGENS ON *EX VIVO* INFECTED HUMAN FETAL MEMBRANE TISSUES ..... 106
5.1 Abstract ..... 106
5.2 Introduction ..... 106
5.3 Methods ..... 108
5.3.1 Bacterial Culture ..... 108
5.3.2 Human Fetal Membrane Co-Culture ..... 109
5.3.3 Raman Microspectroscopy ..... 109
5.3.4 Raman Data Processing & Spectral Analysis ..... 110
5.3.5 Scanning Electron Microscopy ..... 111
5.4 Results ..... 115
5.4.1 Raman Microspectroscopy (RμS) Differentiates Bacterial Species and Strains on Agar ..... 115
5.4.2 RμS Distinguishes Bacterial Infection in Explanted Fetal Membrane Tissues. ..... 117
5.5 Discussion ..... 121
5.6 Acknowledgements ..... 124
5.7 References ..... 126
6. CONCLUSIONS ..... 128
6.1 Summary ..... 128
6.2 Recommendations ..... 133
6.3 Contributions to the Field and Societal Impact ..... 136
APPENDIX 1 DEVELOPMENT OF AN IMAGING FIBER-OPTIC RAMAN PROBE FOR CHARACTERIZING RECURRENT OTITIS MEDIA IN VIVO ..... 139
A1.1 Abstract ..... 139

A1.2 Objectives ..... 139
A1.3 Methods ..... 140
A1.3.1 Raman Spectroscopy ..... 140
A1.3.2 Spectral Data Analysis ..... 144
A1.3.3 Patient Recruitment and Collection of Middle Ear Effusion Samples ..... 144
A1.3.4 Middle Ear Effusion Collection and Evaluation ..... 144
A1.4 Results ..... 145
A1.4.1 Bacteria Detected in MEE Samples using PCR ..... 145
A1.4.2 Raman Spectra Collected Using Raman Probe #1 ..... 150
A1.4.3 Raman Spectra Collected Using Raman Probe #2 ..... 159
A1.5 Discussion ..... 162

## LIST OF TABLES

Table Page

Table 3.1: Classification of *H. influenzae*, *M. catarrhalis*, and *S. pneumoniae* based on SMLR for each bacteria using 77 spectral features.. ..... 47

Table 3.2: Sensitivity and specificity for each bacterial type..... 47

Table 3.3: Probability of each clinical MEE sample involving one or more of the three main bacteria that cause AOM. ..... 50

Table 4.1: Summary of S. aureus strains evaluated using Raman microspectroscopy..... 68

Table 5.1: GBS strains used in this study. ..... 112

Table 5.2: Fetal membrane tissue sample overview. ..... 113

## LIST OF FIGURES

Figure Page

Figure 2.1: Collection of fluid in the middle ear space caused by OM. ..... 8

Figure 2.2: Etiology and pathogenesis of otitis media are multifactorial ..... 9

Figure 2.3: Obstruction of the eustachian tube ..... 10

Figure 2.4: Structure of the human ear ..... 12

Figure 2.5: Comparison of Eustachian tube angle for children compared to adults ..... 14

Figure 2.6: Otoscope view of a human tympanic membrane. ..... 19

Figure 2.7: Schematic of the energy states for Raman and Rayleigh scattering and absorption..... 26

Figure 3.1: Mean-normalized ± standard deviation Raman spectra of bacteria that cause AOM grown on chocolate agar (left column) and MH agar (right column). ..... 44

Figure 3.2: Raman spectra of the three main pathogens that cause acute otitis media and predicted class membership..... 46

Figure 3.3: Raman spectra and bacterial classification of middle ear effusion (MEE) clinical samples.. ..... 49

Figure 4.1: Strains of *S. aureus* streaked onto MH agar. ..... 69

Figure 4.2: Mean ± standard deviation Raman spectra of various bacteria. Spectral signatures of bacteria shown include WT JE2, GBS 1084, GBS 37, and *H. influenzae*. ..... 76

Figure 4.3: Mean ± standard deviation Raman spectra of WT JE2 and Δ*crtM*, a *S. aureus* mutant that lacks pigmentation.. ..... 79

Figure 4.4: Comparison of *S. aureus* mutants based on pigmentation and lipid features ..... 80

Figure 4.5: Spectral region analysis of *S. aureus* mutants based on PC correlation coefficients. ..... 83

Figure 4.6: Spectral regions of interest and subsequent discriminant analysis for *S. aureus* mutants and WT JE2.. ..... 87

Figure 4.7**:** Comparison of *S. aureus* methicillin-sensitive, methicillin-resistant strains, and mutants.. ..... 88

Figure 4.8: Comparison of SCVs based on DNA and pigmentation features..... 90

Figure 4.9: Spectral region analysis of SCVs based on PC correlation coefficients. ..... 93

Figure 4.10: Spectral regions of interest and subsequent discriminant analysis for SCVs and Newman. ..... 94

Figure 5.1: Flowchart of experimental approach divided into tissue sample preparation (orange), Raman data collection and processing (green), and spectral characterization and analysis (yellow). ..... 114

Figure 5.2: Raman spectra of GBS, MRSA, and *E. coli* bacterial colonies present distinct biochemical features. ..... 116

Figure 5.3: Raman microspectroscopy distinguishes infected versus uninfected fetal membrane tissues. ..... 119

Figure 5.4: Raman microspectroscopy of *ex vivo* infected fetal membrane tissues identifies and differentiates bacterial cells within tissues. ..... 120

Figure A1.1: Portable Raman spectroscopy (RS) system with a 785 nm excitation source and fiber-optic RS probe. ..... 142

Figure A1.2: Fiber-optic Raman probe used for clinical measurements of the tympanic membrane. ..... 143

Figure A1.3: Raman fiber-optic probe #2 design. ..... 143

Figure A1.4: Polymerase chain reaction (PCR) of MEE samples for detection of bacteria. ..... 147

Figure A1.5: Polymerase chain reaction (PCR) of MEE samples for detection of bacteria.. ..... 147

Figure A1.6: Polymerase chain reaction (PCR) of MEE samples for detection of bacteria. ..... 148

Figure A1.7: CLSM images of live (green) and dead (red) bacteria in MEE samples. ..... 149

Figure A1.8: White light images of a human tympanic membrane (red arrows) of patient #1 affected with recurrent otitis media with MEE in both ears. ..... 151

Figure A1.9: Cultures of middle ear effusion collected from patient #1. ..... 151

Figure A1.10: Raman spectra collected from the right ear (recurrent OM with MEE) of patient #1 using RS probe #1..... 152

Figure A1.11: White light images of a human tympanic membrane (red arrows) of patient #2 affected with recurrent otitis media with MEE in both ears. ..... 153

Figure A1.12: Raman spectra collected from the left ear (recurrent OM with MEE) of patient #2 using RS probe #1. ..... 153

Figure A1.13: Raman spectra collected from the right ear (recurrent OM with MEE) of patient #2 using RS probe #1..... 154

Figure A1.14: Culture of middle ear effusion collected from patient #1's left ear. ..... 154

Figure A1.15: White light images of a human tympanic membrane (red arrows) of patient #4 affected with recurrent otitis media with no MEE in either ear. ..... 155

Figure A1.16: Raman spectra collected from the left ear (recurrent OM with no MEE) of patient #4 using RS probe #1. ..... 156

Figure A1.17: Raman spectra collected from the right ear (recurrent OM with no MEE) of patient #4 using RS probe #1. ..... 156

Figure A1.18: White light images of a human tympanic membrane (red arrows) of patient #6 affected with recurrent otitis media with MEE.. ..... 157

Figure A1.19: Culture of middle ear effusion collected from patient #6's left ear. ..... 157

Figure A1.20: Raman spectra collected from the left ear (recurrent OM with MEE) of patient #6 using RS probe #1. ..... 158

Figure A1.21: Raman spectra collected from the right ear (recurrent OM with MEE) of patient #6 using RS probe #1. ..... 158

Figure A1.22: Fiber alignment of the RS probe #2 pointing at a neon argon source. ..... 159

Figure A1.23: Non-negative least squares coefficient plot to determine light penetration depth when measuring Raman signal of a vitamin E capsule under deli meat. ..... 160

Figure A1.24: Mean-normalized ± standard deviation Raman spectra of in vivo measurements of the TM comparing normal (no MEE) versus the presence of fluid (MEE). ..... 161

Figure A1.25: Non-normalized ± standard deviation Raman spectra of acetaminophen. ..... 163

Figure A1.26: Non-normalized Raman spectra of the tympanic membrane from patients affected by acute otitis media measured *in vivo*. ..... 163

# CHAPTER 1

## 1. INTRODUCTION

### 1.1 Motivation and Objectives

Otitis media (OM), an inflammatory disease of the middle ear, is the most frequent cause of physician visits and prescription of antibiotics for children.[1] The financial burden is estimated to add $2.88 billion in healthcare costs in the U.S.[2] One of the main challenges in diagnosing acute otitis media (AOM), caused by a bacterial infection, is that it presents symptoms that overlap with otitis media with effusion (OME), which is rarely caused by a bacterial infection. Current methods to diagnose AOM rely on varying symptoms and visual changes related to the tympanic membrane. More importantly, these current routine approaches do not identify bacteria that may be causing AOM, leading to treatment with broad spectrum drugs. This is critical because knowing the bacteria involved will direct physicians to prescribe a more targeted antibiotic if needed and eliminate unnecessary antibiotic treatment, which may reduce the rising number of bacteria that are resistant to antibiotics.

The three main bacteria that cause AOM, *Haemophilus influenzae* (Gram-negative)*, Moraxella catarrhalis* (Gram-negative)*, and Streptococcus pneumoniae* (Gram-positive)*,* are part of normal upper respiratory tract flora. However, under the right conditions these bacteria can thrive in middle ear effusion (MEE) and cause AOM. Furthermore, this disease can be further complicated by antibiotic

resistant bacteria causing an infection, which are more challenging to treat with broad-spectrum antibiotics. An additional barrier to proper recovery may also be due to chronic ear infections caused by the development of biofilms in the middle ear space, which are inherently protected against traditional antibiotics. These scenarios of ear infections demand a tool that is capable of non-invasively probing the molecular makeup of bacteria that cause AOM to identify bacterial species to aid in providing physicians with the information needed to prescribe the correct antibiotic and decrease the course of infection. To meet this need, we propose to use Raman spectroscopy (RS), an inelastic light scattering technique, to identify specific bacteria that may be causing AOM based on the biochemical information the method provides.

RS is able to non-invasively take a real-time measurement of the biochemical composition of a sample by monitoring the interaction of laser light with the vibrational modes of the chemical bonds that compose the sample. The change in energy after the light interacts with the chemical makeup of the sample corresponds to specific molecular features such as lipids, DNA, and amides among other things. Specifically for this study, it is known that Gram-positive bacteria have a thicker cell wall composed of peptidoglycan compared to Gram-negative bacteria. Furthermore, variation in biochemical features such as carbohydrates, surface protein antigens, teichoic acids, and fatty acids that are attached to the cell wall are indicative of differences among bacteria type. In addition, the guanine-cytosine (G+C) content in DNA varies for each of the bacteria that cause AOM.

1.2 Specific Aims

**Aim 1: Characterize the three main bacteria that cause acute otitis media (AOM) using Raman microspectroscopy.** The three most common bacteria that cause AOM (*H. influenzae, M. catarrhalis, and S. pneumoniae*) will be acquired and grown separately on Mueller-Hinton (MH) agar plates and characterized using Raman microscopy (RM), which provides high spectral resolution. Raman spectra will be collected from multiple bacterial colonies for each bacteria. A machine learning statistical model will be used for classification of bacterial strains and to determine important biochemical features for discrimination. Furthermore, this training data will be evaluated using clinical middle ear effusion samples from patients suffering from recurrent otitis media.

**Aim 2: Differentiate isogenic variants and small colony variants of *Staphylococcus aureus* using Raman microspectroscopy.** To evaluate the feasibility of identifying mutant forms of bacteria *in vitro* from ear infections, known isogenic variants of *S. aureus* and small colony variants (SCVs) will be cultured on Mueller-Hinton (MH) agar. Mutants of *S. aureus*, including methicillin-resistance and methicillin-sensitive strains, will be compared using Raman microspectroscopy. Strains from SCVs will include methicillin-sensitive and aminoglycoside-resistant or aminoglycoside-sensitive strains for evaluation. Data reduction analysis such as principal component analysis (PCA) will be used to reduce the high-dimensional data to identify spectral regions important for classification. A discriminant analysis will be implemented to evaluate classification of bacterial strains based on the designated spectral regions.

**Aim 3: Differentiate perinatal pathogens on *ex vivo* infected human fetal membrane tissues using Raman microspectroscopy.** With the development of bacterial biofilms in ear infections, an established biofilm model will be evaluated to determine the feasibility of identifying bacteria directly from tissue without needing to culture bacteria using Raman microspectroscopy. Bacterial strains from Group B *Streptococcus* (GBS) strains, *Escherichia coli*, and *Staphylococcus aureus* will be cultured on MH agar. Raman spectral measurements will be collected directly from bacterial colonies. Differences and similarities of Raman measurements of the colonies will be illustrated using a hierarchical cluster analysis (HCA). Next, an established biofilm tissue model that includes fetal membrane tissues excised from human placental tissues will be treated with antibiotics and then co-cultured with Group B *Streptococcus* (GBS), *Escherichia coli*, and *S. aureus* strains. Multiple spots on each tissue type will be measured using Raman microspectroscopy. Biofilm development in the region of spectral measurement will be validated using scanning electron microscopy (SEM). A machine learning algorithm will be utilized to identify biochemical features important for discriminating bacterial signatures for each tissue infection type.

The ultimate goal of this project is to use Raman spectroscopy to characterize bacteria as part of an active infection, identify mutant forms of bacteria related to ear infections, and determine the feasibility of discriminating bacteria in a relevant biofilm tissue model. The ability of this optical technique to non-invasively probe biochemical features will provide valuable information about bacteria involved in AOM while minimizing discomfort to the patient. This research

has the potential to non-invasively detect and identify bacteria in common ear infections, providing physicians with the diagnostic information needed to improve patient care.

## 1.3 Summary of Chapters

Following this chapter that gives an introduction to the dissertation, Chapter 2 provides relevant physiology and anatomy related to otitis media. In addition, current clinical diagnostic methods for otitis media are described and related to current optical approaches for characterizing otitis media.

Chapter 3 highlights the first report of using Raman microspectroscopy to characterize the three main bacteria that cause acute otitis media and validation of a classification model with clinical specimens (O. D. Ayala et al. 2017).

Chapter 4 extends on findings from Chapter 3 to investigate isogenic variants and resistant strains of bacteria related to those that cause otitis media. A quantitative approach for identifying spectral regions of Raman spectra and their related biochemical significance for identification of drug-resistant *Staphylococcus aureus* strains using Raman microspectroscopy is explored (O. D. Ayala et al. 2018).

Chapter 5 describes the ability of Raman microspectroscopy to differentiate perinatal pathogens on an established biofilm tissue model *ex vivo*. This approach is an important first step for determining the feasibility of characterizing and identifying bacteria in biofilm environments related to otitis media. Specifically, strains of group B *Streptococcus* (GBS), *Escherichia coli*, and methicillin-resistant

*Staphylococcus aureus* (MRSA) were utilized to develop *ex vivo* biofilms on placental tissue (O. D. Ayala *et al.* under review).

Chapter 6 summarizes the major findings from this dissertation and provides recommendations for future work needed to develop a point of care diagnostic tool to detect and identify bacteria in various environments.

Appendix 1 investigates the development of a fiber-optic Raman probe to characterize patients suffering from recurrent otitis media *in vivo*. An image-guided approach is also evaluated for guiding position and placement of this probe during optical measurements.

# CHAPTER 2

## 2. BACKGROUND

### 2.1 The Problem: Acute Otitis Media

There are over 700 million cases worldwide of acute otitis media (AOM) every year. Of these, 51% occur in children less than five years of age.[3] Furthermore, it is estimated that 80% of children will have at least one episode of AOM before the age of three.[4] AOM can have a larger impact than just the infection itself for the patient, especially in underdeveloped areas. The major burden for AOM patients living in developing countries is that they are at higher risk for developing complications such as mastoiditis, chronic suppurative otitis media (CSOM), and hearing impairment.[5] For children experiencing hearing impairment, this may further inhibit proper speech and language development at a critical stage in their lives.

Otitis media (OM) is an inflammatory disease of the middle ear. OM can be categorized as otitis media with effusion (OME) or AOM. Currently, classification as OME or AOM is based on the knowledge, complications, and sequelae of otitis media. OME is an inflammation of the middle ear with a buildup of liquid in the middle-ear space (Figure 2.1). AOM is described as the rapid onset of signs and symptoms, such as otalgia and fever, of acute infection within the middle ear.

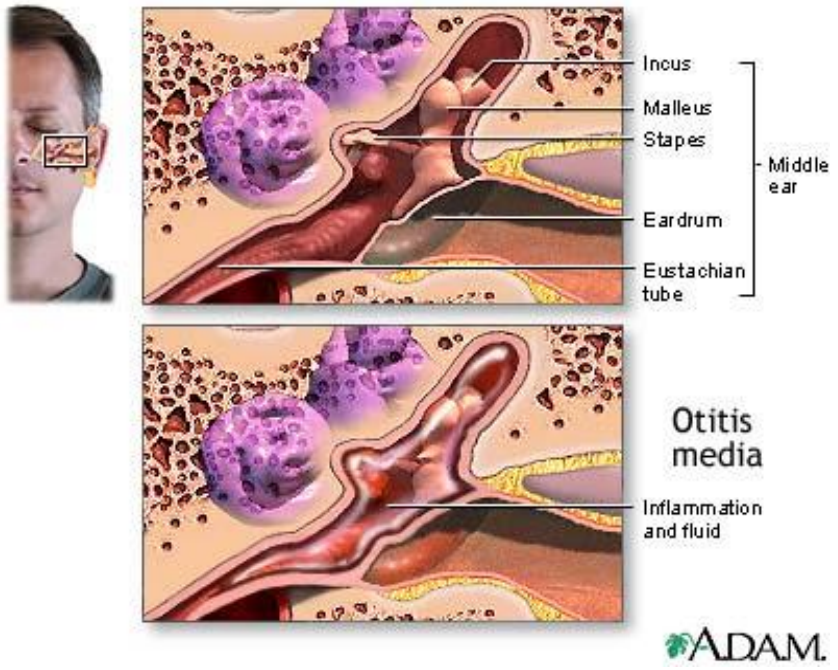


Figure 2.1: Collection of fluid in the middle ear space caused by OM.

There are many factors that make up the etiology and pathogenesis of OM (Figure 2.2). These include genetic factors, infections (bacterial and viral), allergies, environmental factors, and eustachian tube dysfunction.[6] The most important factors that are related to an increase incidence of otitis media in infants and children are Eustachian tube dysfunction and an underdeveloped immune system.

The pathogenesis of OM may be described by the following events: the patient starts with an upper respiratory tract viral infection which results in congestion of the respiratory mucosa of the nose, nasopharynx, and eustachian

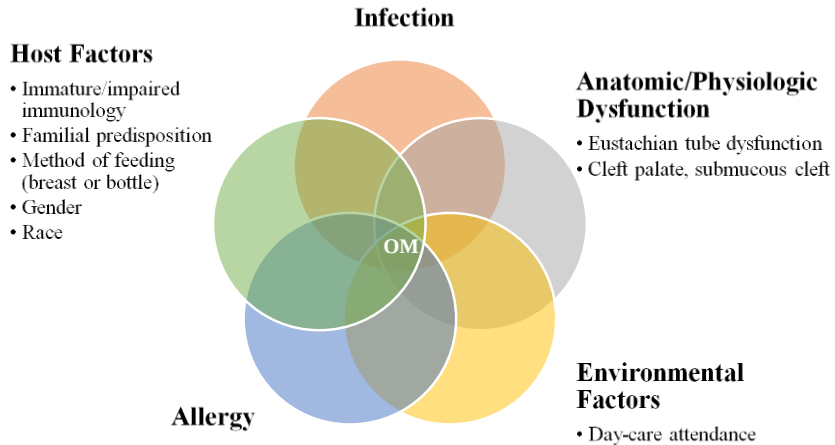


Figure 2.2: Etiology and pathogenesis of otitis media are multifactorial.[6]

tube. This buildup in the eustachian tube causes an obstruction of the isthmus, the narrowest portion of the tube (Figure 2.3).

The obstruction inhibits pressure regulation and results in negative middle-ear pressure, which causes a reflux of mucosal secretions leading to middle ear effusion[6]. If the resulting effusion in the middle ear space is asymptomatic, then it is called OME. However, if there is an active viral or bacterial infection in the upper respiratory tract then these viruses and bacteria causing this infection can be refluxed into the middle ear space and cause AOM. The three main bacteria that cause AOM include *Haemophilus influenzae, Moraxella catarrhalis,* and *Streptococcus pneumoniae*. Although these bacteria are part of the normal upper respiratory tract flora, they may be aspirated into the middle ear space and cause AOM. There are other bacteria types, such as *Staphylococcus aureus* that may

cause AOM, but they are rare. In addition, the percentage of bacteria type that are involved in AOM may vary depending on their geographical location.

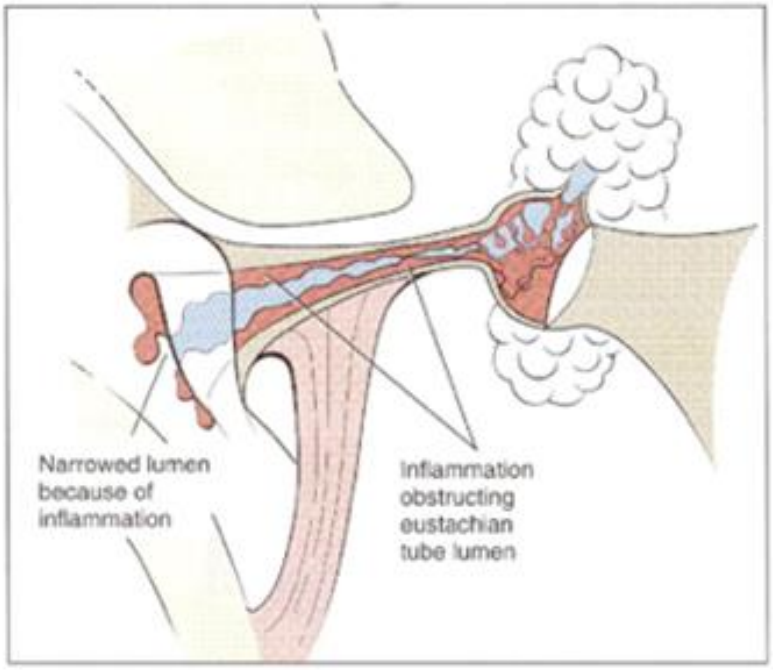


Figure 2.3: Obstruction of the eustachian tube.[6]

The current approach for diagnosing AOM and differentiating it from OME relies on varying symptoms and visual changes. These subtle visual indicators and symptoms make diagnosing AOM challenging. Furthermore, OME is usually not due to an active infection, but may be a sequela of AOM. Currently, the standard for diagnosing AOM is pneumatic otoscopy, which applies pressure to observe the degree of mobility of the tympanic membrane. However, many physicians find the instrument inconvenient due to complications with establishing an air seal with the external auditory canal, which is needed to apply both negative and positive pressure.[7] For severe or recurrent cases, physicians may culture collected ear

effusion to identify bacteria causing an infection. Collecting this fluid requires a needle to be inserted through the tympanic membrane (tympanocentesis), which may be painful for the patient and requires 24-48 hours to culture the fluid obtained. These methods to diagnose AOM rely on evaluating varying symptoms and are an indirect measure of the source of the infection since they lack identification of bacteria causing AOM.

An inaccurate diagnosis between AOM and OME may lead to antibiotic treatment that is not necessary which may lead to antibiotic resistance. To put this in perspective, a large prospective study showed that two out of three children will recover without antibiotics.[8] This sheds light on the importance of identifying bacteria causing an infection not only with the regard of determining if antibiotics are needed, but also in prescribing a more targeted antibiotic if resistant forms are the source.

The following sections describe the anatomy of the ear, which will be important for creating a relevant phantom tympanic membrane model and identifying design constraints for a fiber-optic Raman probe to ultimately perform measurements *in vivo.*

## 2.2 The Ear

The ear is the organ that detects sound by using its three functional parts: the outer (external) ear, middle ear, and inner (internal) ear (Figure 2.4). These structures of the ear are set in the petrous portion of the temporal bone of the

human skull. The petrous part of the temporal bone is one of the densest bones in the human body.

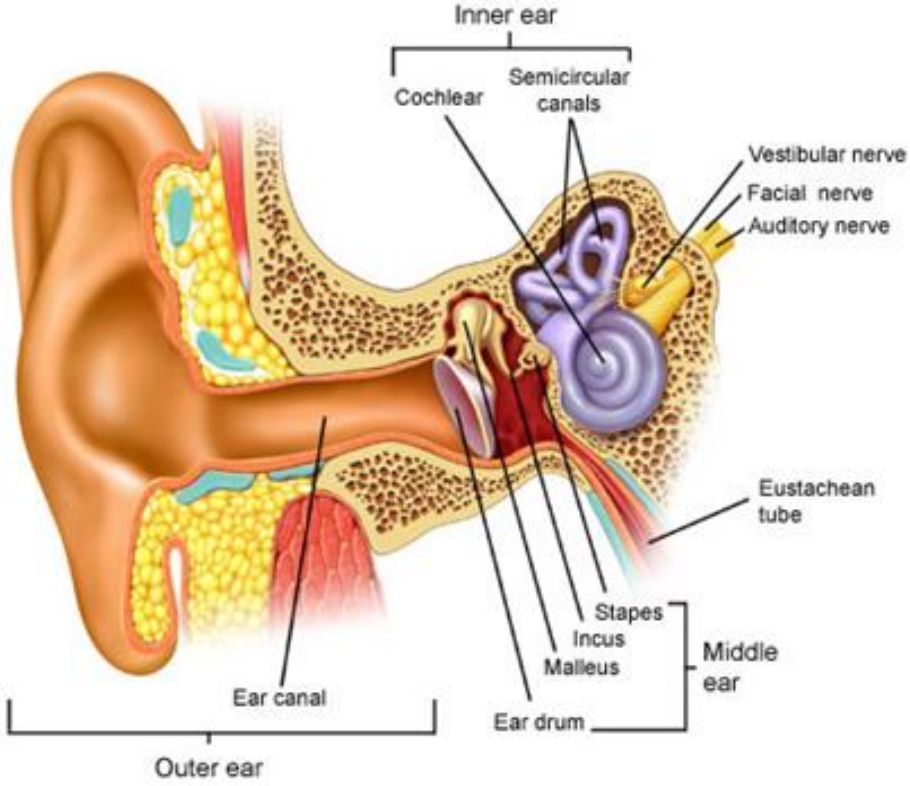


Figure 2.4: Structure of the human ear. (Courtesy of Forward Thinking PT)

### 2.2.1 The Outer Ear

The outer ear consists of the pinna or auricle and the ear canal. The entrance to the ear canal begins at the major pinna depression called the concha, which aids in funneling sound into the canal. The concha has an average diameter that ranges from 15 – 20 mm with an average depth of 13 mm.[9] The ear canal is an “S” shaped duct that provides a path for acoustic waves to meet the tympanic

membrane. The angle of the eustachian tube in reference to the horizontal plane is 45˚ for adults compared to 10˚ in children (Figure 2.5). The outermost one third of the ear canal is comprised of cartilage. This part of the ear canal is lined with 0.5 – 1 mm of skin and contains multiple sebaceous glands, ceruminous (wax) glands, and hair follicles[10]. The innermost two thirds of the ear canal are surrounded by the temporal bone. This is called the osseous part of the canal and is covered with ~0.2 mm of skin[11] with no secretion producing glands or hairs. The skin of the ear canal is innervated by the branches of three cranial nerves, which include the auriculotemporal (mandibular) nerve, facial nerve, and vagus nerve. The average length of an adult ear canal is ~25 ± 2 mm.[12] The canal is oval in shape with an average diameter of 7 – 8 mm.[12-14] The shape and cross sectional dimensions of the ear canal change over its distance with an opening average dimensions of 9 mm by 6.5 mm and becoming narrower along the canal toward the tympanic membrane.[15] At the opening of the ear canal the cross-sectional area is ~0.45 $cm^2$ and decreases to ~0.4 $cm^2$ in the middle of the ear canal. The narrowest point of the ear canal comes at the isthmus, located past the second bend of the ear canal and ~4 mm from the tympanic membrane.[16] After reaching the tympanic membrane it marks the end of the ear canal. The tympanic membrane makes a 45˚ to 60˚ with the floor of the canal.[16-20] This angle of the

tympanic membrane causes the ear canal to be ~6 mm shorter at the top of the ear canal compared to the bottom part.

### 2.2.2 The Middle Ear

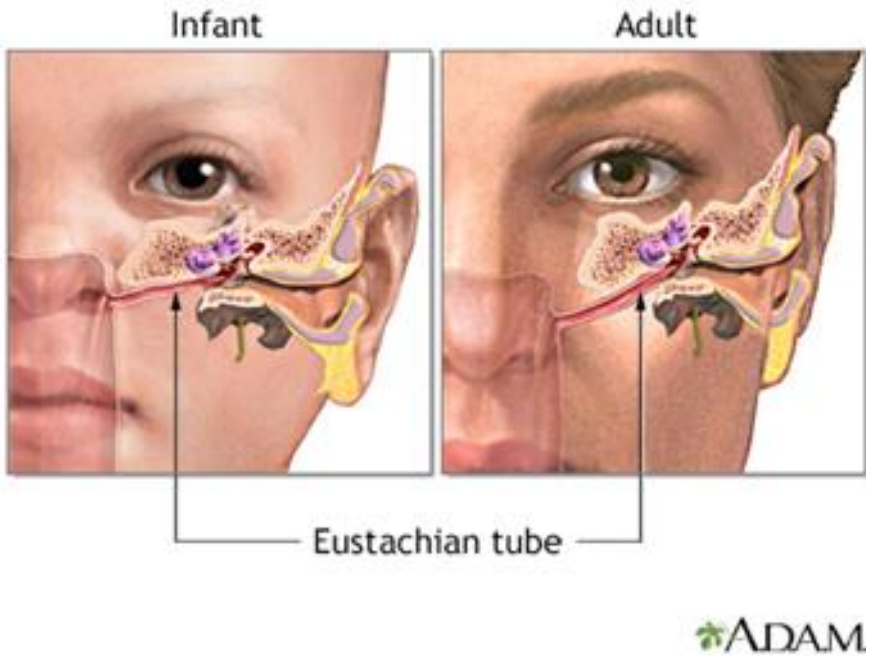


Figure 2.5: Comparison of Eustachian tube angle for children compared to adults. The angle of the eustachian tube for adults is 45˚ compared to 10˚ in children.

The middle ear is an air-filled cavity behind the tympanic membrane called the tympanic cavity. The cavity is lined with mucous membrane tissue with an overall volume of ~2 $cm^3$.[14,21,22] The air in the middle ear cavity remains below atmospheric pressure due to a connection between the tympanic cavity and the upper part of the throat by the eustachian tube. The tympanic cavity houses a group of three small bones (ossicles) called the malleus, incus, and stapes as can

be seen in Figure 4. The floor of the tympanic cavity contains the jugular fossa, a depression in the inferior part of the base of the skull that lodges the bulb of the internal jugular vein.

### 2.2.3 Tympanic Membrane

The tympanic membrane or eardrum is a thin, oval membrane that is normally transparent and separates the outer ear from the middle ear. The conically shaped membrane has a tip, called the umbo, which extends ~1.5 – 2 mm out towards the middle ear.[12,20] Most of the tympanic membrane is attached to the temporal bone except for a narrow area called the notch of Rivinus. The dimensions of the tympanic membrane along its two major perpendicular axes are ~9 – 10 mm and ~8 – 9 mm.[17,23] The average surface area of the tympanic membrane is ~64 $mm^2$, but ranges from 55 – 90 $mm^2$.[14,24] Due to the conical shape of the tympanic membrane, the effective area is less at 55 $mm^2$.[14,16] The normal tympanic membrane has an average thickness of 70 µm, but can range from 30 – 120 µm with the thinnest part at the center and thickest part at the edges.[25-28]

The tympanic membrane is composed of four tissue layers. These include the outer epithelial layer that is continuous with the skin of the ear canal, two middle fiber layers consisting of radial and concentric fibers, responsible for the stiffness of the membrane, and the inner mucous layer that is continuous with the lining of the middle ear cavity. The external layer of the membrane is innervated by the auriculotemporal nerve. Along the surface of the tympanic membrane there is not a uniform stiffness. The surface is divided into two regions: 1) the small lax

triangular area located at the top of the membrane called the pars flaccida and 2) the larger and stiffer region called the pars tensa. This stiffer region is involved in the transmission of acoustic energy from the outer to the middle ear. The modulus of elasticity of a normal tympanic membrane at the center region is ~0.02 – 0.03 GPa.[13,29]

### 2.2.4 The Inner Ear

The inner ear is a complex system of bony structures and labyrinths that is located behind the medial wall of the middle ear. There are three main components which include the semicircular canals, vestibule, and cochlea (Figure 2.4). There are many small blood vessels that provide for the inner ear. Although there are three main components in the inner ear, there are two functionally important elements, which are the cochlea and vestibular system. The cochlea is the sensor organ for hearing and the vestibules are the sensory organs for balance and motion. Below is a table that summarizes important human anatomical factors for designing a fiber-optic Raman probe (Table 2.1).

Table 2.1**:** Anatomical parameters of the human ear canal and tympanic membrane.

| | **Ear Canal** | **Tympanic Membrane** |
|---|---|---|
| **Dimensions** | ~25 mm (length), ~7.5 mm (diameter) | ~9.5 mm x ~8.5 mm, ~70 µm (normal thickness), but can range from 30 – 120 µm (normal) |
| **Composition** | Cartilage, sebaceous glands, hair follicles | Four tissue layers (epithelial, two layers of concentric and radial fibers, and mucus) |

## 2.3 Current Clinical Methods to Diagnose and Treat AOM

### 2.3.1 Clinical Guidelines to Diagnose AOM

Until recently, diagnosis of AOM was based solely on symptomatology. As of 2013, the American Academy of Pediatrics (AAP) and the American Academy of Family Physicians (AAFP) have issued guidelines for the diagnosis of AOM. To diagnose AOM, it requires moderate to severe bulging of the tympanic membrane, new onset of otorrhea not caused by otitis externa, or mild bulging of the tympanic membrane associated with recent onset of ear pain (less than 48 hours) or erythema.[30] This approach to diagnosing AOM has an evidence rating of C, according to AAP and AAFP, which means there is an insufficient amount of published literature, lack of clinical trials, or is based on a physician panel

consensus. This further motivates the need for the development of a novel tool to accurately and reliable diagnose AOM.

### 2.3.2 Pneumatic Otoscopy

Currently, the standard tool for diagnosing AOM and OME is pneumatic otoscopy, which applies pressure to observe the degree of mobility of the tympanic membrane. The ideal pneumatic otoscope should have a light source and create a tight air seal that allows for physicians to create positive/negative pressure. The mobility is proportional to the pressure applied after squeezing and releasing the attached bulb. For normal tympanic membranes, pressure application causes the tympanic membrane to rapidly move inward then outward. However, if there is accumulation of pus or fluid in the tympanic cavity it will cause a significant decrease in tympanic membrane mobility.

The application of pneumatic otoscopy allows the assessment of the contour of the tympanic membrane (normal, retracted, full, or bulging), its color (gray, yellow, pink, amber, white, red, or blue), its translucency (translucent, semiopaque, or opaque), and mobility (normal, increased, decreased, or absent)[31]. A normal tympanic membrane is translucent and pearly gray as seen in Figure 2.6A. However, with the progression in severity of a possible infection, bulging and coloration change (Figure 2.6). The use of pneumatic otoscopy for the diagnosis of AOM and OME is 70% - 90% sensitive and specific for determining middle ear effusion buildup[31-35]. Basic otoscopy, which relies only on subtle visual changes of the tympanic membrane, has a sensitivity and specificity of 60% - 70%.[33,34]

Although pneumatic otoscopy is the current standard of diagnosis of AOM, creating an air-tight seal may be complicated, it relies on symptomatic changes that do not correlate with bacteria involved in the infection, and it does not identify the bacteria involved. This may increase the risk for misdiagnosis between AOM and OME and the course of infection.

### 2.3.3 Tympanometry

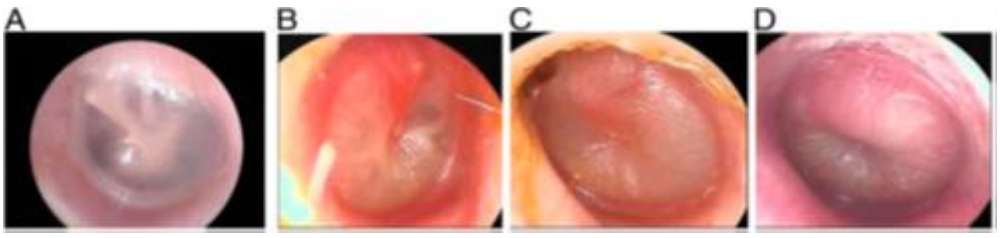


Figure 2.6: Otoscope view of a human tympanic membrane (TM). A) Normal TM, B) TM with mild bulging, C) TM with moderate bulging, and D) TM with severe bulging.[31]

Tympanometry is an objective test of the middle-ear function that measures the compliance of the tympanic membrane. By sending a specific frequency into the ear canal and hitting the tympanic membrane some of the sound waves are reflected back and detected by the device. If the tympanic membrane is stiffer than normal it will cause more sound waves to be reflected back to the detector. The resulting sound waves are converted to admittance and plotted on a tympanogram. In a routine clinical setting, this device can be used to determine the presence of middle ear effusion. Tympanometry has a sensitivity and specificity of 70% - 90% for the detection of middle ear fluid.[36] However, this is dependent on patient cooperation and does not identify bacteria causing the infection.

### 2.3.4 Acoustic Reflectometry

Acoustic reflectometry is a test used to identify the presence of fluid behind the tympanic membrane by emitting sound waves and detecting the reflected sound. The setup includes a built-in speaker, microphone, and microprocessor to collect and analyze data. One study of using this technique in children prior to myringotomy showed a sensitivity and specificity of 83.33% and 68.18%, respectively.[37] Although this technique may be easier and less expensive than tympanometry, its performance was lower in the study referenced and must be correlated with clinical examination. In addition, acoustic reflectometry indirectly measures middle ear effusion. Furthermore, this method is not able to identify the bacteria causing an infection in AOM.

### 2.3.5 Tympanocentesis

Tympanocentesis uses an invasive technique that punctures a hole in the inflamed tympanic membrane to extract middle ear effusion. The collected fluid is then prepared and cultured to identify bacteria causing an infection. Currently, this is the only technique that is used and is the “gold standard” to identify bacteria causing an infection. In addition to the invasive nature of the procedure, not all fluid may be collected and more importantly not all middle ear effusion is culturable. A range of studies have shown that collected MEE was culturable in 21 – 70% of samples.[38-43] Although this may infer that bacteria may not play a role in cases of OME, it has been shown there is the presence of bacterial DNA using PCR.[44] However, this approach may also be an inaccurate representation of the MEE as

remnants of nucleic acids may not necessary correlate with viable bacteria. Therefore, further exploration has been dedicated to investigating biofilm formation and their role on AOM and OME. Tympanocentesis is rarely practiced and only performed when antibiotic treatment is repeatedly unsuccessful.

### 2.3.6 Standard Treatment Protocol

When a patient presents with possible symptoms of AOM, the severity of the infection is determined given the following criteria.[30] Antibiotics can be automatically prescribed based on symptoms such as moderate or severe otalgia, otalgia for at least 48 hours, or temperature of 102.2 ˚F or higher (for children who are six months or older). For children less than two years of age with bilateral AOM regardless of additional symptoms, antibiotics are also prescribed. For children with non-severe symptoms, antibiotics are not prescribed and they enter a watchful waiting period. A high-dose amoxicillin is typically the first line of treatment. However, a patient may have a more severe bacterial infection causing AOM. If this occurs, the patient may be prescribed amoxicillin-clavulanate, which includes treatment for β-lactamase positive organisms. Additional prescriptions may be made if the infection is not managed. Failure of prescribing a targeted antibiotic to treat AOM increases the risk antibiotic resistance, a growing problem for treatments. The last resort if previous antibiotics were unsuccessful is to perform tympanocentesis to identify the bacteria involved in the infection and then prescribe a targeted antibiotic.

For recurrent cases of infection, ear tubes may be surgical placed inside of the tympanic membrane to allow for drainage of any fluid in the tympanic cavity. Tube placements may be dislodged and the procedure may need to be repeated. This may result in scarring and damage of the tympanic membrane, ultimately effecting hearing, speech, and language development in children.

## 2.4 Optical Methods to Diagnose OM

### 2.4.1. Diffuse Reflectance

Diffuse reflectance is based on the reflection of scattered light from various angles of the surface of a sample. This technique has been used to investigate erythema of the tympanic membrane *in vivo* for diagnosing OM in children[45]. They were able to distinguish between otitis media with mucous versus otitis media with serous effusion. However, color of the tympanic membrane was not taken into account, which could affect classification results. Furthermore, this approach was not able to identify bacteria that caused AOM.

### 2.4.2 Optical Coherence Tomography

Optical coherence tomography (OCT) is an imaging method that provides high-resolution micro-scale structure images based on tissue reflectivity and is comparable to histology. OCT has been used to measure the thickness of the tympanic membrane at different infection states *in vivo*.[46] Their system used an 830 nm source to scan the tympanic membrane and determine thickness. They

were able to classify normal, acute, and chronic states in adult patients. Furthermore, they were able to identify possible biofilm formation behind a tympanic membrane in a chronic infection. Although this approach is able to differentiate different types of OM, it does not identify the bacteria causing the infection. Therefore, treatment is limited to the current approach performed in the clinic.

## 2.5 Optical Techniques to Identify Bacteria

### 2.5.1 Fluorescence Spectroscopy

Fluorescence spectroscopy is based on analyzing the emitted fluorescence intensity as a function of wavelength for a fluorophore. Fluorescence has been used to investigate *S. pneumoniae, S. aureus, M. catarrhalis,* and *H. influenzae in vitro*.[47] They were able to show fluorescent signals for these bacteria, but presenting unique profiles of mixed bacteria samples may be more challenging due to broadband and subtle differences commonly seen with fluorescence spectroscopy. Furthermore, fluorescence spectroscopy does not provide a specific biochemical signature of a sample such as bacteria.

### 2.5.2 Fourier Transform Infrared Spectroscopy (FT-IR Spectroscopy)

FT-IR spectroscopy utilizes infrared (IR) light to probe a sample based on absorption of the excitation source. FT-IR has been mainly applied on dry bacteria samples.[48] This setup requires time and preparation of the sample. Furthermore,

because there is high absorption of water in the IR range, it makes this method challenging to use for practical applications, such as in investigating bacteria in MEE.

### 2.5.3 Raman Spectroscopy and Raman Microspectroscopy

The technique of Raman spectroscopy (RS) is based on in-elastically scattered light to provide biochemical information about a sample. Raman microspectroscopy (RMS) has been used to identify and characterize bacteria in microbial colonies with the goal of detecting their presence in a shorter incubation time.[49] Confocal RMS has also been used to investigate the biochemical features of bacterial biofilms.[50] A fiber-optic probe-based Raman system has been used to identify bacteria in bacterial colonies and determine spectral features that were important in distinguishing Gram-positive bacteria from Gram-negative bacteria.[51]

## 2.6 The Clinical Need

Current routine clinical practice for diagnosing AOM is based on evaluating varying symptoms. Basing a diagnosis on symptoms or pairing with current techniques has not been shown to be reliable. There is no standard method to diagnose AOM at this time. The only method that was able to determine bacteria involved in a possible case of AOM is used only in severe cases. By not identifying the specific bacteria causing an infection, it increases the risk of antibiotic resistance because a broad spectrum antibiotic is used as the first line of treatment. If this medication does not work, then another antibiotic is prescribed at

a higher concentration. This is repeated as the course of infection continues and bacteria gain resistance towards these antibiotics. This may have immediate and long-term implications for children that affects their speech and language development. Furthermore, critical infections may lead to more traumatic cases such as mastoiditis seen commonly in developing countries. There is a critical need to detect the presence of and identify bacteria causing otitis media to provide physicians with the information needed to prescribe the correct antibiotic.

## 2.7 The Solution

Raman spectroscopy is an optical technique that uses in-elastically scattered light to provide biochemical information of a particular sample. An excitation source is used for this method to interact with the vibrational modes of the molecules in the sample. An excitation photon may either gain energy or lose energy from the molecule it interacts with and therefore change the emitted frequency (Figure 2.7). This change in energy transfer is unique to each vibrational conformation that is specific for a molecular structure. Therefore, this technique is very sensitive to biochemical markers in a sample and can be used to determine the sample. A Raman spectrum shows the scattered light intensity versus the Raman shift, of scattered photons. Therefore, this technique is wavelength independent because it measures a change in energy after light interaction with the molecule. The x-axis is presented in units of wavenumbers ($cm^{-1}$), which is the reciprocal of wavelength. The intensity for each wavenumber corresponds to the number of Raman scattered photons at that specific wavenumber.

As a biochemically specific technique, RS is an ideal candidate for this project to identify bacteria. Cellular components such as N-acetylglucosamine (NAG) and N-acetylmuramic acid (NAM) which are amino sugars that form a crystal lattice structure to make a bacterial cell wall may be important in classifying

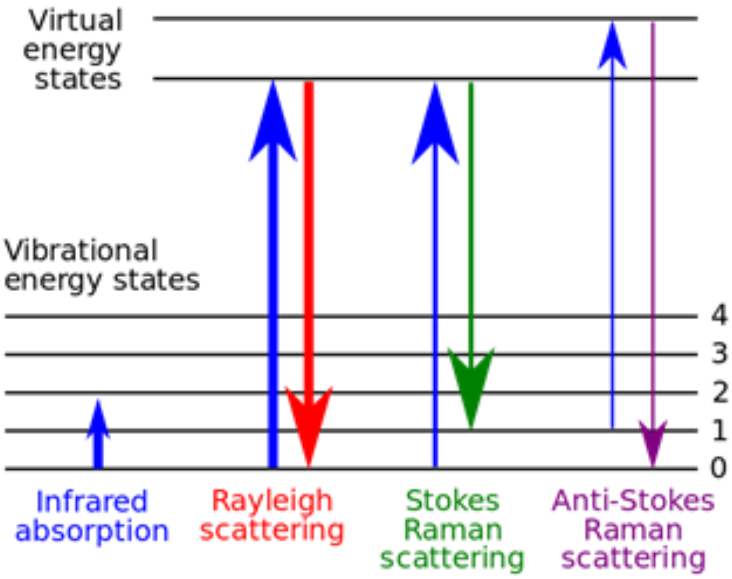


Figure 2.7: Schematic of the energy states for Raman and Rayleigh scattering and absorption.

Gram-positive and Gram-negative bacteria. Peptidoglycan may have a higher Raman peak intensity in Gram-positive bacteria since they have a greater concentration compared to Gram-negative bacteria. Teichuronic acid is also specific to Gram-positive bacteria. Additional unique cell wall chemical features for Gram-negative bacteria include an O-antigen complex and lipoprotein.[52] These biochemical differences in bacteria in addition to relative DNA features motivate the use of Raman spectroscopy to identify bacteria that cause AOM.

## 2.8 References


1. J. O. Klein, The burden of otitis media, Vaccine, 2001, 19:S2-S8.

2. S. Ahmed, Incremental health care utilization and costs for acute otitis media in children, The Laryngoscope, 2014, 124:301-305.

3. L. Monasta, et al., Burden of disease caused by otitis media: systematic review and global estimates. PLoS One, 2012, 7(4):e36226.

4. H. L. Burrows, et al., Otitis Media Guideline Team. University of Michigan Health System otitis media guideline, 2013, http://www.med.umich.edu/1info/fhp/practiceguides/om/OM.pdf.

5. S. Berman, Otitis media in developing countries. Pediatrics, 1995, 96:126-131.

6. C. D. Bluestone and J. O. Klein, Otitis Media and Eustachian Tube Dysfunction. In: Bluestone CD, Simons JP, Healy GB, eds. Pediatric Otolaryngology. 5th ed. Shelton, Conn: People's Medical Publishing House; 2014:633-759.

7. M. E. Pichichero, Acute Otitis Media: Part I. Improving Diagnostic Accuracy. American Family Physician, 2000, 61(7):2051-2056.

8. F. Marchetti, L. Ronfani, S. C. Nibali, et al.; Italian Study Group on Acute Otitis Media. Delayed prescription may reduce the use of antibiotics for acute otitis media: a prospective observational study in primary care. Arch Pediatr Adolesc Med. 2005, 159(7):679-684.

9. M. D. Burkhard and R. M. Sachs. Anthropometric manikin for acoustic research. Journal of the Acoustical Society of America, 1975, 58:214-222.

10. F. E. Lucente, (1995). Anatomy, histology, and physiology. In: *The External Ear,* Lucente, FE, Lawson, W, and Novick, NL (Eds.). Philadelphia: W.B. Sounders Company.

11. C. Muller, Tympanoplasty, Grand Rounds paper. Houston: Department of Otolaryngology. University of Texas. Retrieved November 4, 2015 from http://www.utmb.edu/otoref/Grnds/T-plasty-030115/T-plastyslides-030115.pdf.

12. L. S. Alvord and B. L. Farmer, Anatomy and orientation of the human external ear. Journal of the American Academy of Audiology, 1997, 8:383-390.

13. G. von Bekesy. The structure of the middle ear and hearing of one's own voice by bone conduction. Journal of the Acoustical Society of America, 1949, 21:217-232.

14. W. R. Zemlin. (1997). *Speech and Hearing Science: Anatomy and Physiology* (4th Ed.). Boston: Allyn and Bacon.

15. E. A. G. Shaw. (1974). The external ear. In: *Handbook of Sensory Physiology (Vol. VI): Auditory System,* Keidel, WD and Neff, WD (Eds.). New York: Springer-Verlag.

16. J. A. Seikel, D. W. King, and D. G. Drumright. (2000). *Anatomy and Physiology for Speech, Language, and Hearing.* San Diego: Singular Publishing Group.17. Gray, H. (1918). *Anatomy of the Human Body,* 20th edition. Philadelphia: Lea and Febiger.

18. M. R. Stinson and B. W. Lawton, Specification of geometry of the human ear canal for the predication of sound-pressure level distribution. Journal of the Acoustical Society of America, 1989, 85:2492-2503.

19. E. F. Decreamer, J. J. Dirckx, and W. R. Funnell, Shape and derived geometrical parameters of the adult, human tympanic membrane measure with a phase-shift moiré interferometer. Hearing Research, 1991, 51:107-121.

20. M. Sundberg (2008). Optical methods for tympanic membrane characterization. Linkoping Studies in Science and Technology, Dissertation No. 1173. Linkoping (Sweden) L Liu-Tryck.

21. P. Dallos. (1973). *The Auditory Periphery.* New York: Academic Press.

22. W. Yost and D. Nielson (1977). *Fundamentals of Hearing: An Introduction.* New York: Holt, Rinehart, and Winston.

23. H. Gelfand (1998). *Hearing: An Introduction to Psychological and Physiological Acoustics.* New York: Mercel Decker.

24. J. D. Harris. (1986). *Anatomy and Physiology of the Peripheral Auditory Mechanism.* Austin, TX: Pro-Ed.

25. J. A. Donaldson and J. M. Miller. (1980). Anatomy of the ear. In: *Otolaryngology,* Pararella, M and Shumrick, D (Eds.), *Basic Sciences and Related Disciplines,* 1:26-42. Philadelphia: Sounders.

26. Y. Kojo, Morphological studies of the human tympanic membrane. Journal of Oto-Rhino-Laryngological Society of Japan, 1954, 57:115-126.

27. D. J. Lim, Human tympanic membrane: An ultrastructural observation. Acta Otolaryngologica, 1970, 70:176-186.

28. E. Waver and M. Lawrence. (1954). *Physiological Acoustics.* Princeton, NJ: Princeton University Press.

29. W. F. Dacraemer, M. A. Maes, and V. J. Vanhuyse, An elastic stress-strain relation for soft biological tissues based on a structural model, Journal of Biomechanics, 1980, 13:463-468.

30. K. M. Harmes, R. A. Blackwood, H. L. Burrows, J. M. Cooke, R. van Harrison, and P. P. Passamani. Otitis media: diagnostics and treatment. American Family Physician, 2013, 88(7):435-440.

31. A. S. Lieberthal, A. E. Carroll, T. Chonmaitree, T. G. Ganiats, A. Hoberman, M. A. Jackson, M. D. Jofee, D. T. Miller, R. M. Rosenfold, X. D. Sevilla, R. H. Schwartz, P. A. Thomas, and D. E. Tunkel. The diagnosis and management of acute otitis media. Pediatrics, 2013, e964-e999.

32. K. A. Daly and G. S. Giebink. Clinical epidemiology of otitis media. Journal of Pediatric Infectious Diseases, 2000, 19(5):S31-S36.

33. P. G. Shekelle, G. Takata, S. J. Newberry, T. Coker, M. A. Limbos, L. S. Chan, M. M. Timmer, M. J. Suttorp, J. Carter, A. Motala, D. Valentine, B. Johnson, and R. Shanman. Management of acute otitis media: update. Evidence Report/Technology Assessment, 2010, 198:1-426.

34. American Academy of Family Physicians; American Academy of Otolaryngology-Head and Neck Surgery; American Academy of Pediatrics Subcommittee on Otitis Media with Effusion. Otitis media with effusion. *Pediatrics*. 2004, 113(5):1412-1429.

35. S. I. Pelton, Otoscopy for the diagnosis of otitis media. Journal of Pediatric Infectious Diseases, 1998, 17(6):540-543.

36. G. W. Watters, J. E. Jones, and A. P. Freeland, The predictive value of tympanometry in the diagnosis of middle ear effusion. Clinical Otolaryngology Allied Science, 1997, 22(4):343-345.

37. S. Kimball. Acoustic reflectometry: spectral gradient analysis for improved detection of middle ear effusion in children. Journal of Pediatric Infectious Diseases, 1998, 17(6):552-555.
38. G. M. Matar, N. Sidani, M. Fayad, U. Hadi, Two-step PCR-based assay for identification of bacterial etiology of otitis media with effusion in infected Lebanese children. Journal of Clinical Microbiology, 1998, 36:1185–1188.

39. L. Hall-Stoodley, F. Z. Hu, A. Gieseke, L. Nistico, D. Nguyen, J. Hayes, et al., Direct detection of bacterial biofilms on the middle-ear mucosa of children with chronic otitis media, JAMA, 2006, 296:202–211.

40. L. P. Schousboe, T. Ovesen, L. Eckhardt, L. M. Rasmussen, C. B. Pedersen, How does endotoxin trigger inflammation in otitis media with effusion? Laryngoscope, 2001, 111:297–300.

41. U. Gok, Y. Bulut, E. Keles, S. Yalcin, M. Z. Doymaz, Bacteriological and PCR analysis of clinical material aspirated from otitis media with effusions, Int. J. Pediatr. Otorhinolaryngology, 2001, 60:49–54.

42. D. M. Poetker, D. R. Lindstrom, C. E. Edmiston, C. J. Krepel, T. R. Link, J. E. Kerschner, Microbiology of middle ear effusions from 292 patients undergoing tympanostomy tube placement for middle ear disease, Int. J. Pediatr. Otorhinolaryngol. 69 (2005) 799–804.

43. C. D. Bluestone, J. S. Stephenson, L. M. Martin, Ten-year review of otitis media pathogens, Pediatr. Infect. Dis. J. 11 (8 Suppl.) (1992) S7–S11.

44. M. Daniel, S. Imtiaz-Umer, N. Fergie, J. P. Birchall, and R. Bayston, Bacterial involvement in otitis media with effusion. International Journal of Pediatric Otorhinolaryngology, 2012, 76:1416-1422.

45. M. Sundberg, M. Peebo, P. A. Oberg, P. G. Lundquist, and T. Stromberg, Diffuse reflectance spectroscopy of the human tympanic membrane in otitis media, Physiological Measurement, 2004, 25:1473-1483.

46. G. L. Monroy, R. L. Shelton, R. M. Nolan, C. T. Nguyen, M. A. Novak, M. C. Hill, D. T. McCormick, and S. A. Boppart, Noninvasive depth-resolved optical measurements of the tympanic membrane and middle ear for differentiating otitis media, The Laryngoscope, 2015, 125:e276-e282.

47. M. J. Sorrel, J. Tribble, L. Reinisch, J. A. Werkhaven, and R. H. Ossoff, Bacteria identification of otitis media with fluorescence spectroscopy, Lasers in Surgery and Medicine, 1994, 14:155-163.

48. K. Maquelin, C. Kirschner, L-P. Choo-Smith, N. van den Braak, H. Ph. Endtz, D. Naumann, and G. J. Puppels, Identification of medically relevant microorganisms by vibrational spectroscopy, Journal of Microbiological Methods, 2002, 51:255-271.
49. K. Maquelin, L-P. Choo-Smith, T. van Vreeswijk, H. Ph. Endtz, B. Smith, R. Bennett, H. A. Bruining, and G. J. Puppels, Raman spectroscopic method for identification of clinically relevant microorganisms growing on solid culture medium, Analytical Chemistry, 2000, 72:12-19.

50. C. Sandt, T. Smith-Palmer, J. Pink, L. Brennan, and D. Pink, Confocal Raman microspectroscopy as a tool for studying the chemical heterogeneities of biofilms in situ, Journal of Applied Microbiology, 2007, 103:1808-1820.

51. F. S. de Siqueira e Oliveira, H. E. Giana, and L. Jr. Silveira, Discrimination of selected species of pathogenic bacteria using near-infrared Raman spectroscopy and principal components analysis, Journal of Biomedical Optics, 2012, 17(10):107004-1:8.

52. M. O'Leary, Practical Handbook of Microbiology, (CRC Press, Inc., Boca Raton, FL, 1989), p. 352-353.

# CHAPTER 3

## 3. CHARACTERIZATION OF BACTERIA CAUSING ACUTE OTITIS MEDIA USING RAMAN MICROSPECTROSCOPY

### 3.1 Abstract

Otitis media (OM) is a prevalent disease that is the most frequent cause of physician visits and prescription of antibiotics for children. Current methods to diagnose OM and differentiate between the two main types of OM, acute otitis media (AOM) and otitis media with effusion (OME), rely on interpreting symptoms that may overlap between them. Since AOM requires antibiotic treatment and OME does not, there is a clinical need to distinguish between AOM and OME to determine whether antibiotic treatment is necessary and guide future prescriptions. We used an optical spectroscopy technique, Raman spectroscopy (RS), to identify and characterize the biochemical features of the three main pathogens that cause AOM *in vitro*. A Renishaw inVia confocal Raman microscope at 785 nm was used to spectrally investigate the Raman signatures of *Haemophilus influenzae*, *Moraxella catarrhalis*, and *Streptococcus pneumoniae*. Biochemical features or biomarkers important for classification of each bacterial species were identified and yielded a 97% accuracy of discrimination. To test the effectiveness of Raman-based bacterial classification in a clinical sample, human middle ear effusion (MEE) from patients affected by recurrent AOM was collected, cultured, and measured using RS. The probability of bacterial involvement from

each of the three main bacteria that cause AOM was determined from the clinical MEE samples. These results suggest the potential of utilizing RS to aid in accurately diagnosing AOM and providing physicians with bacterial identification to guide treatment.

## 3.2 Introduction

Otitis media (OM), an inflammatory disease of the middle ear, is the leading cause of acute physician visits and prescription of antibiotics for children.[1] Worldwide, there are over 700 million cases of acute otitis media (AOM) every year with 51% of these cases occurring in children less than five years of age.[2] The impact of AOM can extend beyond an infection, possibly leading to complications such as mastoiditis, chronic suppurative otitis media (CSOM), and hearing impairment, which may be severely debilitating for child development.[3] Otitis media with effusion (OME) is one of the two types of OM and is described as asymptomatic inflammation of the middle ear with a build-up of fluid in the middle ear space. Contrary to OME, AOM presents with a rapid onset of signs and symptoms, such as fever, associated with acute infection within the middle ear. AOM is commonly caused by an active bacterial infection in the upper respiratory tract that is refluxed into the middle ear space. Antibiotic therapy is prescribed to manage AOM in children six months and older presenting severe signs and symptoms, while antibiotic treatment is not recommended for children with OME. Currently, clinical diagnosis of AOM is based on visual evaluation of the tympanic membrane (TM) and symptoms caused by the infection. Clinical guidelines issued

by the American Academy of Family Physicians (AAFP) and American Academy of Pediatrics (AAP) are based on visual evidence such as bulging of the TM with recent onset of ear pain or erythema to diagnose AOM.[4] These symptoms are further assessed using a pneumatic otoscope, the current standard tool for diagnosing OM. Additionally, diagnosis relies on the assessment of the contour, color, translucency, and mobility of the TM.[5] Pneumatic otoscopy allows the physicians to view the TM and apply pressure to observe its mobility. Pneumatic otoscopy is 70% - 90% sensitive and specific for determining accumulation of middle ear effusion (MEE) in the middle ear, which usually develops post-infection.[5–9] Basic otoscopy, which relies only on subtle visual changes of the tympanic membrane, has a sensitivity and specificity of 60% - 70%.[7-8] Although pneumatic otoscopy improves visualization of symptomatic changes in the TM, findings are not able to identify or correlate with bacteria causing an infection. Other techniques, though less commonly implemented in routine clinical care include: tympanometry, which measures TM compliance using sound; acoustic reflectometry, which seeks to identify the presence of fluid behind the TM by emitting and detecting the reflected sound; and tympanocentesis, which is an invasive technique used to extract MEE through the tympanic membrane to be cultured for identification of bacteria causing an infection. Pneumatic otoscopy and tympanometry are limited in their performance and do not detect or identify bacteria in ear effusion. Tympanocentesis then, is currently the “gold standard” for identifying bacteria causing an ear infection. In addition to the invasive nature of the procedure, not all fluid may be collected and more importantly not all MEE is

easily cultured, delaying identification of bacteria causing an infection. In fact, tympanocentesis is rarely practiced and only performed when antibiotic treatment is repeatedly unsuccessful, which can still result in not identifying the causative microorganisms. This gap of diagnostic information may cause physicians to over-prescribe antibiotics for cases of OME, which are rarely caused by a bacterial infection, or prescription of antibiotics to pathogens that have developed resistance to specific classes of antibiotics in acute infections.

Optical spectroscopy has in recent years received significant attention for disease diagnosis. Optical methods that have been explored for detecting OM include diffuse reflectance spectroscopy, fluorescence spectroscopy, and optical coherence tomography (OCT). Diffuse reflectance spectroscopy utilizing a coupled fiber-optic bundle with an otoscope has been used to distinguish the color of the tympanic membrane for diagnosis of AOM in 15 normal and 15 AOM patients.[10] While this group was able to distinguish between OM with mucous versus serous effusion, the performance of the technique to differentiate between AOM and OME was limited since it relied primarily on detecting the inflammatory state of the TM. Fluorescence spectroscopy has also been used *in vitro* to characterize the main bacteria that cause OM and to create a library of fluorescence features of these pathogens.[11] In a subsequent publication, fluorescence was measured from 12 chinchilla AOM models *in vivo* with limited success.[12] OCT, an optical imaging method that provides high-resolution real-time *in vivo* images of tissue microstructures, has been used to measure the thickness of the human TM at different infection states *in vivo*.[13] Researchers of this study

were able to classify normal, acute, and chronic states of OM in adult patients based on TM thickness and biofilm formation for chronic cases. Performance accuracy of 70-80% was achieved due in part to the lack of consistency in biofilm growth across the TM and in all patients. Although all three optical methods were researched with the goal of *in vivo* application, these approaches are limited by their poor specificity and inability to detect and identify bacteria that cause AOM.

Raman spectroscopy (RS) is an optical technique that uses inelastically scattered light to provide biochemical information of a particular sample. This technique is sensitive to biochemical features such as nucleic acids, lipids, proteins, and carbohydrates and is able to provide a biochemical profile without the need of added contrast agents. RS has been used for many years to probe the biochemistry of various biological molecules.[14] and more recently for disease detection.[15–17] More specifically, RS has been applied to characterize and identify bacteria *in vitro* as a proof of concept design. One example includes utilizing RS to characterize bacterial signatures in microbial colonies with the goal of detecting their presence in a shorter incubation time.[18] Another research group used a benchtop confocal Raman microscopy to identify bacteria within a mixed bacteria biofilm model.[19] Furthermore, Raman microspectroscopy has been used for *Mycoplasma pneumoniae* strain typing to distinguish between multiple clusters of strains.[20] The feasibility of implementing a fiber-optic probe-based Raman system to characterize spectral signatures of bacterial colonies has also been shown and used to determine biochemical features important for distinguishing between Gram-positive and Gram-negative bacteria.[21] Interrogation of bacterial

components such as surface wall features have also been investigated using surface-enhanced RS (SERS), which involves the addition of nanoparticles to the sample to enhance the Raman signal of targeted biomarkers.[22] Although these studies have shown the potential of RS for bacterial detection and identification, no studies to date have investigated bacteria that cause AOM and none have focused on the potential development for *in vivo* application. Currently, there is no tool available to rapidly and non-invasively detect the presence and identity of bacteria causing a middle ear infection. The goal of this study is to determine the feasibility of discriminating between the three main bacteria that cause AOM. Successful classification of these species was accomplished by spectrally characterizing their biochemical composition. We present the ability to classify bacteria causing AOM using Raman microspectroscopy and assess the feasibility of developing this technique for the diagnosis of AOM.

## 3.3 Materials & Methods

### 3.3.1 Selection of Agar Growth Media

Two of the most common agar types for bacterial culture, chocolate and Mueller-Hinton, were tested to determine their ability to grow all three bacteria while having the least spectral interference. Chocolate agar medium (Thermo Fisher Scientific, Waltham, MA), which is derived from lysed red blood cells and mainly used for fastidious organisms, was purchased in prepared 85 mm monoplates to culture bacteria. Chocolate agar was compared to Mueller-Hinton

(MH) agar, which is a non-selective, non-differential microbiological growth medium that contains basic nutrients and no additives. MH agar was prepared by suspending 11 g of MH (BD, Franklin Lakes, NJ) powder and 7.5 g (15% agar/L) of agar (Thermo Fisher Scientific, Waltham, MA) in 500 mL of distilled water while heating (180˚F) and stirring. The mixture was then autoclaved at 121 ˚C for 10 minutes. Bacteria were streaked separately on both MH agar and chocolate agar plates for comparison of agar and subsequent spectroscopic analysis of the bacterial strains.

### 3.3.2 Bacterial Species

The three main bacteria that cause acute otitis media (AOM) were purchased from American Type Culture Collection (ATCC): nontypeable *Haemophilus influenzae* (ATCC #49766), *Moraxella catarrhalis* (ATCC #49143), and *Streptococcus pneumoniae* (ATCC #6301). Propagation methods as recommended by ATCC were used for each strain in preparation for bacteria cultures. Each bacterial species was streaked separately onto MH agar and chocolate agar plates. *H. influenzae* is a fastidious organism that requires lysed red blood cells not found in MH agar, therefore it is commonly grown on chocolate agar. To effectively grow *H. influenzae* on MH agar, hemin and nicotinamide adenine dinucleotide (NAD)-rich disks (Hardy Diagnostics, Santa Maria, CA) were added to MH agar plates using steel tweezers that were disinfected between the additions of disks. Chocolate and MH agar plates were cultured for 24 hours at 37 ˚C with 5% $CO_2$.

### 3.3.3 Human Middle Ear Effusion Samples

As a proof of concept model to determine the ability of Raman microspectroscopy to identify bacteria derived from clinical samples, de-identified middle ear effusion (MEE) was collected from patients scheduled for myringotomy with tympanostomy at Monroe Carell Jr. Children's Hospital at Vanderbilt. A protocol for collection of discarded, de-identified MEE specimens was approved by the Vanderbilt University Institutional Review Board (IRB# 130960) as non-human subjects research. To test the feasibility of our approach, three MEE samples were captured using a sterile Juhn Tym-Tap middle ear fluid device (Medtronic Inc., Minneapolis, MN) with an aspirator. A swab was used to spread MEE on MH agar plates with added hemin and NAD-rich disks and allowed to incubate for 72 hours at 37 ˚C with 5% $CO_2$. Viable colonies were then collected using sterile loop and streaked on a new MH agar plate with hemin and NAD-rich disks for a subsequent 24 hour culture at 37 ˚C with 5% $CO_2$. Evaluation of colony morphology was used as the standard for bacterial identification from MEE samples.

### 3.3.4 Raman Microspectroscopy

Raman spectra were acquired using a confocal Raman microscope (inVia Raman Microscope, Renishaw plc, Gloucestershire, UK) with a 785 nm laser diode (Renishaw plc, Gloucestershire, UK). A 100X (N PLAN EPI, NA=0.85, Leica, Weltzlar, Germany) objective was used to focus a ~1 μm laser spot onto the

bacterial colony on the agar surface at 27 mW. Raman scattered light was epi-detected through the same objective, then passed through a 35 µm slit and dispersed by a holographic grating (1200 lines/mm) onto a thermoelectrically cooled (-70 ˚C) deep-depleted, CCD that provided a 1 $cm^{-1}$ spectral resolution. The theoretical spatial resolution of the confocal Raman microscope system is ~0.6 µm. System alignment and light throughput to the sample was confirmed before and after experimental measurements with an internal silicon standard intensity at 520 $cm^{-1}$ and laser power at the sample.

Raman microspectroscopy was used to investigate the bacteria of interest since it provides high resolution for each wavenumber, an important feature to accurately characterize the spectral signature of the pathogens. Spectral measurements of pure bacteria included three acquisitions per spot, three spots per colony, and three colonies per bacteria, which presented an optimal standard deviation for each bacterial strain. Spectral acquisition parameters included a 30-second photobleach followed by a 15-second exposure with 7 accumulations from 700–1800 $cm^{-1}$. Cosmic ray removal from collected Raman spectra was performed using a custom MATLAB script (Mathworks, Natick, MA). Raman spectra were then processed to remove background fluorescence using a least squares modified polynomial fitting algorithm[23] and smoothed for noise with a second-order Savitzky-Golay filter.[24] Post-processed spectra were mean normalized to each individual Raman spectrum for comparative analysis.

### 3.3.5 Data Analysis

To quantify the spectral analysis, a Bayesian machine learning algorithm, sparse multinomial logistic regression (SMLR), was implemented to classify collected Raman spectra as *H. influenzae*, *M. catarrhalis,* or *S. pneumoniae*. SMLR is a supervised learning algorithm that reduces high dimensional multiclass data into features needed for distinguishing between classes.[25] SMLR calculates a weight value for each spectral feature in a given spectral range based on its ability to separate classes within a given training data set. The statistical model also outputs how often (frequency) spectral features are utilized from the training data to determine classification across all cross-validations. SMLR was selected for our application since it provides the tools to classify multiclass data and identify spectral biomarkers important for discrimination. Both of these features were important for characterizing the three main pathogens that cause AOM.

To evaluate the importance of spectral features used for classification, a scaled version (from 0 to 1) of both the weight and how often spectral features were found from SMLR was utilized. The product of these values is used to calculate the SMLR feature importance, which is a quantitative metric that considers both the biochemical differences across the three bacterial strains characterized in this study and spectral heterogeneity among the same bacteria.[26] The sparsity (λ) for SMLR, which controls the capacity for the number of spectral features used for classification, was adjusted to minimize data overfitting. SMLR feature importance was calculated for *H. influenzae*, *M. catarrhalis*, and *S. pneumoniae* using 77 features (λ=1.0) (Figure 3.2). From the total spectral

features available to use, about 8% were used for classification. A total of 917 spectral features from each Raman measurement were available for evaluation. Classification was based on implementing a leave-one-colony-out cross-validation approach. To accomplish this, a k-fold cross-validation was implemented, which separates the original data into *k* equally sized partitions called subsamples. This cross-validation technique retains one of the *k* subsamples and uses it to test the model while the remaining *k*-1 subsamples are utilized as the training data set. A 9-fold cross-validation was used for Raman spectral data analysis. This approach translates to classifying a bacterial colony belonging to a specific bacteria type and would more accurately evaluate a predictive model.

## 3.4 Results

Figure 3.1 shows the average Raman spectra collected from the three main bacteria that cause AOM, *H. influenzae*, *M. catarrhalis*, and *S. pneumoniae*, after being cultured on chocolate agar and MH agar. A qualitative analysis of bacteria cultured in chocolate agar shows many broad spectral regions with higher standard deviations compared to bacteria cultured on MH agar. Spectral regions that were challenging to discern in chocolate agar are indicated in figure 3.1A, C, and E. with a dashed vertical line. Raman peaks in this same spectral region for bacteria cultured on MH agar were identified as indicated. A 10-fold reduction in spectral noise was calculated for Raman spectra of bacteria grown in MH agar compared to chocolate agar by using the standard deviation of the mean normalized intensity between 1500 $cm^{-1}$ and 1504 $cm^{-1}$, which contained minimal

Raman features. Spectral analysis of bacteria grown in MH agar resulted in identifiable, reproducible peaks for the three bacterial strains under investigation that were originally not possible in chocolate agar as shown with arrows in Figure 3.1B, D, and F. Raman features included 827 $cm^{-1}$ (Tyrosine), 1298 $cm^{-1}$ (lipid), and 1447 $cm^{-1}$ ($CH_2$ and $CH_3$ deformations in proteins) for *H. influenzae*, 852 $cm^{-1}$ (CCH aromatic) and 1339 $cm^{-1}$ ($CH_2$ and $CH_3$ fatty acids and proteins) for *M. catarrhalis*, and 783 $cm^{-1}$(Cytosine, uracil) and 1317 $cm^{-1}$ (Guanine) for *S. pneumoniae*. The signal base line of Raman spectra and spectral peaks highlighted above from MH agar cultures were not affected by the addition of hemin and NAD disks, which were required for growth of *H. influenzae*. From these findings, MH agar was selected as the agar of choice for growing bacteria that cause AOM based on its minimal spectral interference and reduction in noise compared to chocolate agar.

Raman spectra from the three main pathogens that cause AOM were characterized to identify possible biochemical features that may be important in classifying these bacteria. Features of interest based on different peak intensities from mean normalized spectra included cytosine and uracil (ring stretching) at 783 $cm^{-1}$, tyrosine at 828 $cm^{-1}$, tryptophan and exopolysaccharide at 1555 $cm^{-1}$, and adenine, guanine (ring stretching), and C-O vibration modes of peptidoglycan at 1574 $cm^{-1}$ (Figure 3.1). These spectral features presented visual differences and were representative of biochemical components of bacteria. Since traditional differences in peak intensities may not capture all of the information found in

spectra and informative spectral changes between bacteria types, multivariate statistical analysis was utilized for feature selection and bacterial classification.

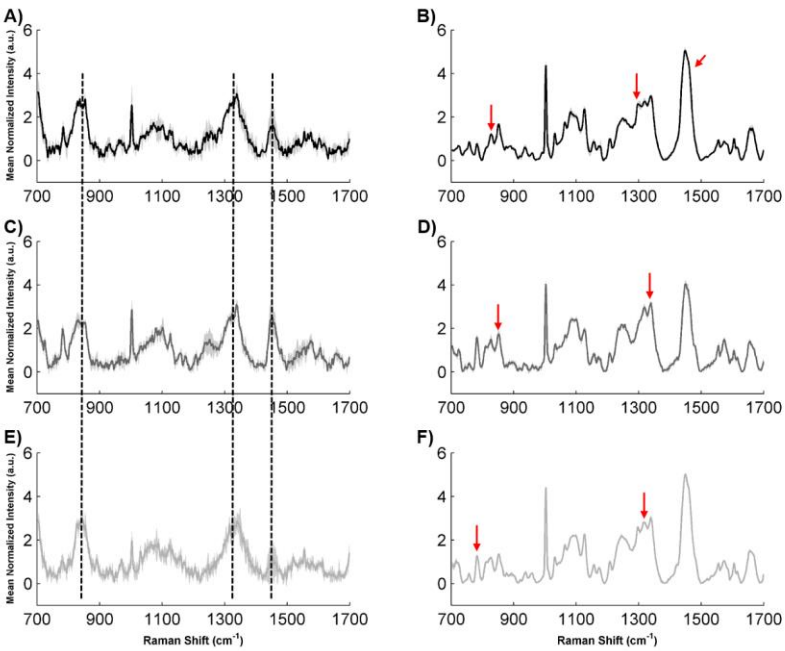


Figure 3.1: Mean-normalized ± standard deviation Raman spectra of bacteria that cause AOM grown on chocolate agar (left column) and MH agar (right column). (A-B) Haemophilus influenzae cultured on chocolate agar (A) and MH agar (B); (C-D) Moraxella catarrhalis cultured on chocolate agar (C) and MH agar (D); (E-F) Streptococcus pneumoniae cultured on chocolate agar (E) and MH agar (F). Vertical dashed lines on the left column represent spectral features from bacteria cultured on chocolate agar that are not discernable, while the arrows in the right column identify these features from the same bacteria cultured on MH agar. A 10x reduction in noise in MH agar compared to chocolate agar was calculated by using the standard deviation of the mean normalized intensity between 1500 $cm^{-1}$ and 1504 $cm^{-1}$.

Figure 3.2 highlights wavenumbers or spectral features that were most important in classification of each bacterial strain denoted with gray vertical bands on the Raman spectra. The gradient of the vertical gray band in Figure 3.2A represents the SMLR feature importance, where darker bands indicate spectral features that were both strongly weighted from their regression coefficients and identified frequently for successful classification. The following peaks were most important in classification of bacteria that cause AOM as determined by SMLR: *H. influenzae* – 783 $cm^{-1}$ (Cytosine, uracil ring stretching), *M. catarrhalis* – 1431 $cm^{-1}$ (symmetric $CH_2$ bending and wagging), and *S. pneumoniae* – 840 $cm^{-1}$ (pyranose in peptidoglycan). Furthermore, the positive and negative slope of the 1449 $cm^{-1}$ ($CH_2/CH_3$ deformations in lipids/proteins) peak was consistent in classifying each of the three main bacteria that causes AOM. The predicted probability of class membership for each bacteria type is shown in Figure 3.2B. This SMLR classification was based on 77 spectral features (λ, sparsity =1.0) after implementing SMLR analysis on a total of 81 spectra collected from the three main otopathogens that cause AOM (27 spectra from each bacteria type) shown in Figure 3.2B. Table 3.1 presents the classification results as a confusion matrix, which describes the performance of a classification model based on the actual and predicted values.

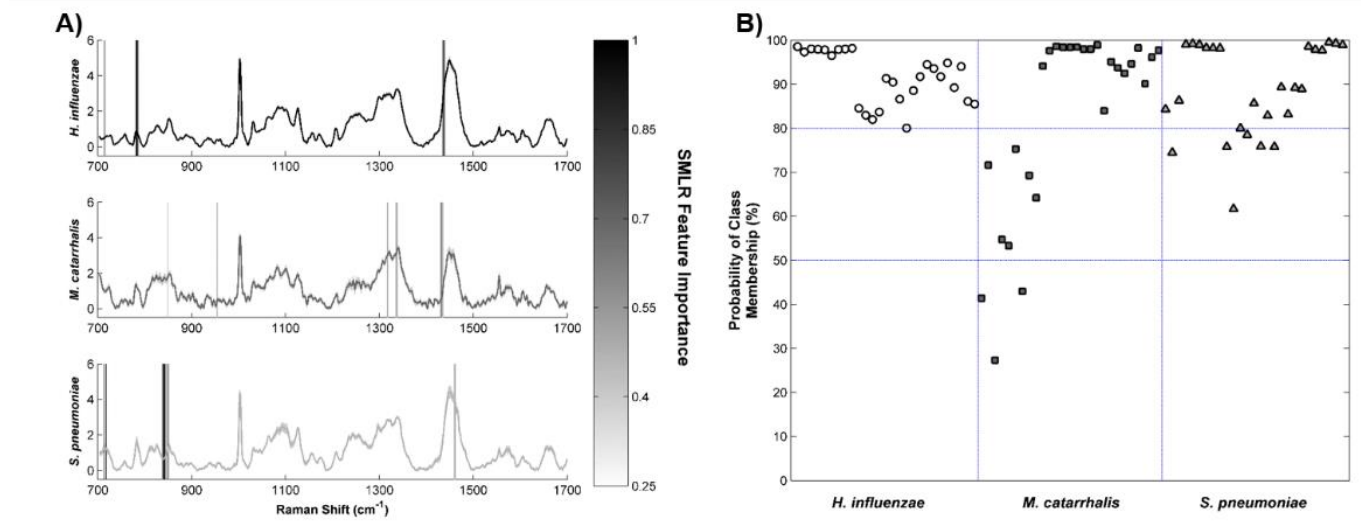


Figure 3.2: Raman spectra of the three main pathogens that cause acute otitis media and predicted class membership. (A) Mean ± standard deviation Raman spectra of H. influenzae, M. catarrhalis, and S. pneumoniae grown on MH agar. Gray bands represent spectral features used for SMLR classification of each bacteria type by using a sparsity value of λ=1.0 for the SMLR input. The band gradient was based on SMLR feature importance. (B) Posterior probability of class membership from SMLR classification for each bacteria based on leave-one-colony-out cross-validation.

Table 3.1: Classification of *H. influenzae*, *M. catarrhalis*, and *S. pneumoniae* based on SMLR for each bacteria using 77 spectral features. Rows represent known bacteria types, while columns represent output from the classifier.

| **λ=1.0, 50% Threshold** | ***H. influenzae*** | ***M. catarrhalis*** | ***S. pneumoniae*** |
|---|---|---|---|
| *H. influenzae* | 27 | 0 | 0 |
| *M. catarrhalis* | 0 | 24 | 3 |
| *S. pneumoniae* | 0 | 0 | 27 |

Sensitivity and specificity were also calculated based on the classification using a 50% threshold probability for class membership (Table 3.2). From the 81 total spectral measurements across all bacteria, less than 5% were misclassified as seen in *M. catarrhalis*. To our knowledge, this is the first report that characterizes the three main bacteria that cause AOM using Raman spectroscopy.

Table 3.2: Sensitivity and specificity for each bacterial type.

| **λ=1.0, 50% Threshold** | **Sensitivity** | **Specificity** |
|---|---|---|
| *H. influenzae* | 100% | 100% |
| *M. catarrhalis* | 89% | 100% |
| *S. pneumoniae* | 100% | 89% |

Clinical MEE samples were also analyzed based on the spectral characterization of *H. influenzae*, *M. catarrhalis*, and *S. pneumoniae* (Figure 3.3).

As shown in Figure 3.3A, mean normalized Raman spectra with standard deviation of MEE samples presented distinct biochemical features used to identify bacteria involved in a MEE sample. After culturing the MEE samples, only one bacterial colony grew from MEE sample #1. For MEE sample #2 and #3, 27 spectra were collected from each across three bacterial colonies. The classification of a bacterial colony belonging to one or more of the three main pathogens that cause AOM was based on spectral characterization of these bacteria, which was utilized for SMLR analysis as shown in Figure 2.2A. The probability of a MEE sample spectrum belonging to one or more bacteria was analyzed using a posterior probability plot (Figure 3.3B) and summarized in Table 3. The first two Raman spectra of MEE sample #1 were not classified since their classification probability was below the threshold of 50%. All three MEE samples showed high probability of belonging to *M. catarrhalis* according to both Raman spectroscopy (Table 3.3) and based on features identified from colony morphology using the standard hockey puck test[27] and light microscopy. These findings show the importance of characterizing the three main bacteria that cause AOM and implementing a proof of concept model to non-destructively identify bacteria in cultured MEE specimens using Raman microspectroscopy.

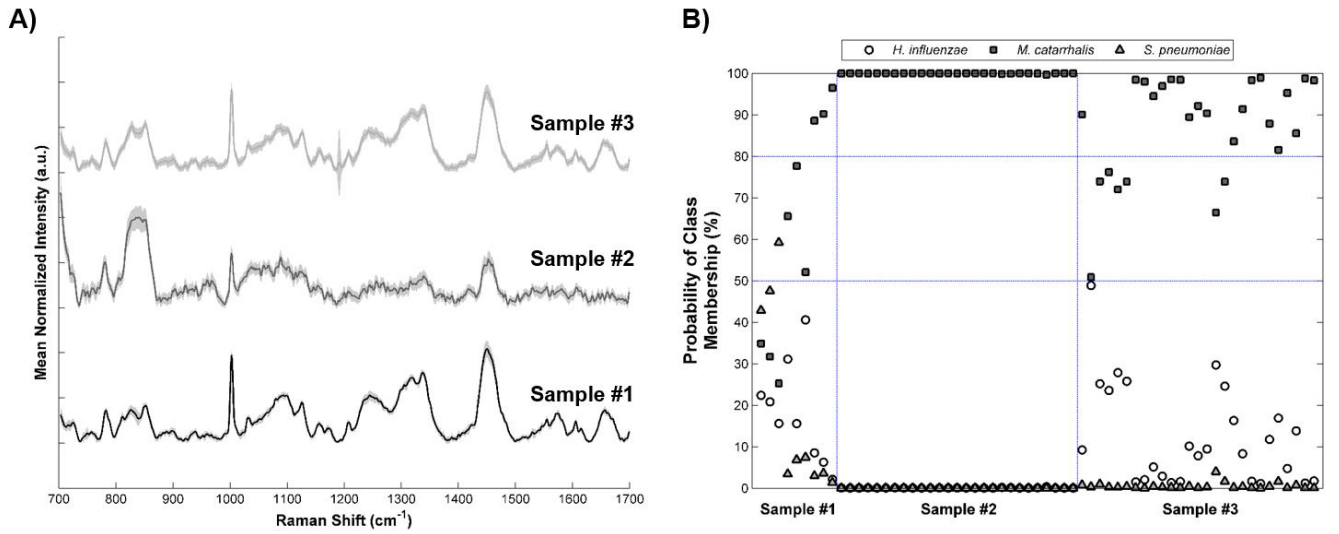


Figure 3.3: Raman spectra and bacterial classification of middle ear effusion (MEE) clinical samples. (A) Mean ± standard deviation Raman spectra of bacterial colonies from clinical MEE samples cultured on MH agar. (B) Posterior probability of class membership of clinical MEE samples to each of the three main pathogens that cause AOM.

Table 3.3: Probability of each clinical MEE sample involving one or more of the three main bacteria that cause AOM.

| λ=1.0, 50% Threshold | Sample #1 | Sample #2 | Sample #3 |
|---|---|---|---|
| **Probability of *H. influenzae*** | 0% | 0% | 0% |
| **Probability of *M. catarrhalis*** | 67% | 100% | 100% |
| **Probability of *S. pneumoniae*** | 11% | 0% | 0% |

## 3.5 Discussion

Current methods to diagnose OM rely primarily on visual assessment and focus on predicting the presence of fluid in the middle ear space. The challenge is distinguishing whether there are active bacteria causing an acute infection (AOM) or only effusion, which is rarely caused by a bacterial infection (OME). Antibiotic treatment should only be prescribed for patients with AOM and not OME since they target a broad range of active bacteria. The inability to determine the presence and identity of bacteria causing AOM has led to an overprescription of antibiotics, leading to antibiotic-resistant bacteria.[28] These antibiotic-resistant bacteria along with development of biofilms in the middle ear mucosa lead to the development of chronic OM infections. Action to investigate the middle ear effusion for bacterial identification is rarely practiced, serving as a last resort, and may be misleading due to obtaining negative cultures.[29–31] A method that can characterize and classify bacteria that cause AOM will provide physicians with information on

bacteria involved in an ear infection, allowing them to prescribe more targeted antibiotics and reducing antibiotic resistance. This Chapter focuses on determining the feasibility of using RS to discriminate between the three main bacteria that cause AOM, *H. influenzae*, *M. catarrhalis*, and *S. pneumoniae* by characterizing their biochemical signatures. Preliminary findings show promise for implementing this technique as an *in vivo* diagnostic tool.

Prior to investigating bacteria using RS, it was important to first select a culture agar medium that would be able to grow all three of the main bacteria that cause AOM while minimizing agar spectral contribution within the typical fingerprint window (700-1800 $cm^{-1}$). Although chocolate agar is one of the most common agar types to use for culturing bacteria, bacterial colonies grown in this agar type absorb light more strongly as an opaque medium compared to a translucent medium such as MH agar. The combination of the absorption by bacteria of the additional ingredients used in chocolate agar and the darker medium of the agar led to lower signal quality compared to that of MH agar. This resulted in less photons being Raman scattered and therefore Raman spectra with higher signal noise, making it more challenging to discern spectral peaks as shown in Figure 3.1. While *M. catarrhalis* and *S. pneumoniae* can grow in other agar types, *H. influenzae*, a fastidious organism, requires hemin and NAD to grow, which is released from the lysed RBCs as part of the chocolate agar media. Therefore, these factors were added to MH agar to grow *H. influenzae*. Spectral features of bacteria grown in MH agar as shown in Figure 3.1 can be easily identified with lower spectral noise compared to the same bacteria grown in

chocolate agar. Spectral contribution of MH agar was minimal compared to the spectral features found in the main bacteria that cause AOM. Signal from underlying culture media has been investigated with the goal of minimizing incubation time while still obtaining spectral features from bacteria of interest. Although this was not the goal of this paper, Maquelin *et al.* investigated the potential of identifying bacteria in agar within 6 hours post-culture.[18] Since colonies from that study were ~10-100 μm in diameter and limited in thickness, there was an overwhelming signal from the underlying culture medium interfering with strain identification. Therefore, they developed and applied a vector correction algorithm on first derivative spectra to remove signal contributions from culture medium in bacterial microcolonies. Although this method may be applied for known bacteria, clinical samples may take more than 6 hours to culture and involve polymicrobial infections, which may limit the application of this algorithm.

We have reported the characterization and identification of the three main pathogens that cause AOM using Raman microspectroscopy. As can be seen in Figure 3.2A, our SMLR feature importance (SMLR-FI) algorithm extracted specific spectral features critical for identification. A threshold of at least 25% importance was set to present more important biomarkers used for classification. The nontypeable *H. influenzae* (NTHi) strain showed 100% sensitivity and specificity. The biomarker with the highest SMLR-FI used for identification of *H. influenzae* was at 783 $cm^{-1}$ (Cytosine, uracil ring stretching). Identification of *M. catarrhalis* in MH agar was found with 89% sensitivity and 100% specificity. As can be seen from Figure 3.2B, three spectral measurements fell below 50% for the probability

of belonging to specific bacteria class (*H. influenzae*, *M. catarrhalis*, and *S. pneumoniae*). This may be due to phase variation in bacteria, which alters protein expression in different regions of a bacterial population. One example of phase variation commonly seen in *M. catarrhalis* is the UspA1 protein, which affects adherence factors that facilitate adhesion to other cells and surfaces.[32] This type of phase variation has been shown to occur in an *in vitro* environment when individual colonies were tagged using monoclonal antibodies for the UspA1 protein.[33] Although there may have been phase variation between *M. catarrhalis* colonies, multiple spectral features were identified for classifying this bacteria. The spectral feature identified to be the most important for classification of *M. catarrhalis* using SMLR-FI was 1431 $cm^{-1}$ (symmetric $CH_2$ bending and wagging). Classification for the third main strain that causes AOM, *S. pneumoniae*, presented a 100% sensitivity and 89% specificity. As can be seen from Figure 3.2A, the most important spectral marker for discrimination of *S. pneumoniae* was at 840 $cm^{-1}$, which is tentatively assigned as pyranose, a sugar commonly found in the cell wall structure of bacteria.[34] This sugar may be found more predominantly in peptidoglycan from Gram-positive bacteria, such as *S. pneumoniae*, and may be important for determining bacterial susceptibility.[34]

The spectral characterization of the main bacteria that cause AOM was used to identify those same bacteria involved in MEE from patients suffering from recurrent OM. This proof of concept approach was able to identify bacteria from cultured MEE samples. For MEE sample #1, only 9 spectra were collected since only one bacterial colony grew post-culture from this sample. Although two of the

spectra collected from sample #1 had a probability of less than 50% for belonging to a specific type of bacteria, the remaining 7 spectra had at least a 50% chance of belonging to *M. catarrhalis.* For MEE samples #2 and #3, 100% of the 27 spectra collected were categorized as *M. catarrhalis*. Overall, nearly 80% of Raman spectra collected across all clinical MEE samples had ≥80% probability of belonging to *M. catarrhalis*. These results were also supported by a hockey puck test[27], which uses a sterile wooden stick to push the colonies across the MH agar plate. The bacterial colonies easily slid across the agar plate, which indicated a positive outcome for *M. catarrhalis*. A major challenge for bacterial identification from clinical samples is the difficulty associated with culturing bacteria. This is more frequently presented with bacteria immersed in a biofilm environment, which limits the ability to culture particular clinical samples. Ultimately, the inability to culture bacteria in a biofilm state may limit our diagnosis of bacteria involved in chronic infections. This drawback highlights the importance of being able to detect the presence and identity of bacteria directly in a biofilm without the need to culture the bacteria. The potential impact of this solution may increase bacterial identification accuracy and decrease diagnostic time and cost.

Our findings from characterizing the biochemical features of the three main otopathogens that cause AOM and accurately identifying them shows the potential application of RS as a diagnostic tool for patients suffering from OM. While additional bacteria species and isogenic variants that cause AOM will need to be interrogated, non-destructive spectral identification and classification of the three main bacteria that cause AOM is a critical first step for developing a diverse

spectral database to accurately detect and identify bacteria causing AOM. This work sets the stage for other applications of RS where bacterial identification may also be utilized as a research tool to investigate bacterial growth patterns, antibiotic susceptibility, or characterize biochemical changes in mutant forms of bacteria. Spectral results from these experiments may serve to create a better understanding of the microbial pathogenesis of other clinical bacterial infections. These studies provide insight into the biochemical changes occurring at the micro-scale and portends to the global application of this technique for the development of targeted antibiotics for susceptible and antibiotic-resistant bacteria. Numerous reports have been published recently describing the effects of over-prescription of broad-spectrum antibiotics and prescriptions of antibiotics for pathogens causing AOM that are no longer susceptible to them.[28,35–38] This is a major problem that has led to antibiotic resistance in many bacteria and even multi-drug resistant (MDR) microorganisms. Providing a rapid technique that accurately detects and identifies pathogens causing AOM will aid in OM diagnostic efforts and inform physicians on proper treatment.

## 3.6 Acknowledgements

The authors would like to acknowledge the support in part by the National Center for Advancing Translational Sciences of the National Institutes of Health under Award Number UL1 TR000445. This research was conducted with Government support under and awarded by DoD, Air Force of Scientific Research, National Defense and Engineering Graduate (NDSEG) Fellowship, 32 CFR 168a.

3.7 References


1. M. M. Rovers, The burden of otitis media, Vaccine **26,** 2–8 (2008).

2. L. Monasta, *et al.* Burden of disease caused by otitis media: Systematic review and global estimates. PLoS One **7,** (2012).

3. S. Berman. Review Otitis Media in Developing Countries. **96,** (1995).

4. K. M. Harmes, *et al.* Otitis media: diagnosis and treatment. Am. Fam. Physician **88,** 435–40 (2013).

5. A. S. Lieberthal, *et al.* The Diagnosis and Management of Acute Otitis Media. Pediatrics **131,** e964–e999 (2013).

6. K. A. Daly and G. S. Giebink, Clinical epidemiology of otitis media. Pediatr. Infect. Dis. J. **19,** S31–S36 (2000).

7. P. G. Shekelle, G. Takata, S. J. Newberry, T. Coker, M. A. Limbos, L. S. Chan, M. J. Suttorp, M. J., Carter, J., Motala, A., Valentine, D., and Breanne Johnsen, R. S. Management of acute otitis media. *Evid. Rep. Technol. Assess. (Full. Rep).* 1–426 (2010).

8. American Academy of Family Physicians, American Academy of Otolaryngology-Head and Neck Surgery, and American Academy of Pediatrics Subcommittee on Otitis Media With Effusion. *Pediatrics* **113,** 1412–1429 (2004).

9. S. I. Pelton, Otoscopy for the diagnosis of otitis media. Pediatr. Infect. Dis. J. **17,** 540–543 (1998).

10. M. Sundberg, M. Peebo, P. Å. Öberg, P. G. Lundquist, and T. Strömberg, Diffuse reflectance spectroscopy of the human tympanic membrane in otitis media. Physiol. Meas. **25,** 1473–1483 (2004).

11. M. J. Sorrell, J. Tribble, L. Reinisch, J. A. Werkhaven, and R. H. Ossoff, Bacteria identification of otitis media with fluorescence spectroscopy. Lasers Surg. Med. **14,** 155–163 (1994).

12. B. C. Spector, L. Reinisch, D. Smith, and J. A. Werkhaven. Noninvasive fluorescent identification of bacteria causing acute otitis media in a chinchilla model. Laryngoscope **110,** 1119–1123 (2000).

13. G. L. Monroy, *et al.* Noninvasive depth-resolved optical measurements of the tympanic membrane and middle ear for differentiating otitis media.

Laryngoscope **125,** E276–E282 (2015).

14. J. Twardowski and P. Anzenbacher, *Raman and IR spectroscopy in biology and biochemistry*. (1994).

15. D. I. Ellis, D. P. Cowcher, L. Ashton, S. O'Hagan, and R. Goodacre, Illuminating disease and enlightening biomedicine: Raman spectroscopy as a diagnostic tool. Analyst **138,** 3871–84 (2013).

16. C. Krafft, S. Dochow, B. I. Latka, B., and J. P. Dietzek, Diagnosis and screening of cancer tissues by fiber-optic probe Raman spectroscopy. Biomed. Spectrosc. Imaging **1,** 39–55 (2012).

17. Q. Tu and C. Chang, Diagnostic applications of Raman spectroscopy. Nanomedicine Nanotechnology, Biol. Med. **8,** 545–558 (2012).

18. K. Maquelin, T. Vreeswijk, H. van Endtz, and B. Smith, Raman spectroscopic method for identification of clinically relevant microorganisms growing on solid culture medium, *Anal. Chem* **72,** 12–19 (2000).

19. C. Sandt, T. Smith-Palmer, J. Pink, L. Brennan, and D. Pink, Confocal Raman microspectroscopy as a tool for studying the chemical heterogeneities of biofilms in situ. *J. Appl. Microbiol.* **103,** 1808–1820 (2007).

20. K. Maquelin, K. *et al.* Raman spectroscopic typing reveals the presence of carotenoids in Mycoplasma pneumoniae. *Microbiology* **155,** 2068–2077 (2009).

21. F. S. de Siqueira e Oliveira, H. E. Giana, and L. Silveira, Discrimination of selected species of pathogenic bacteria using near-infrared Raman spectroscopy and principal components analysis. *J. Biomed. Opt.* **17,** 107004 (2012).

22. R. M. Jarvis, A. Brooker, and R. Goodacre, Surface-enhanced Raman scattering for the rapid discrimination of bacteria. *Faraday Discuss.* **132,** 281–292 (2006).

23. C. A. Lieber and A. Mahadevan-Jansen, Automated Method for Subtraction of Flourescence from Biological Raman Spectra. *As* **57,** 1363–1367 (2003).

24. A. Savitzky and M. J. E. Golay, Smoothing and Differentiation of Data by Simplified Least Squares Procedures. *Anal. Chem.* **36,** 1627–1639

(1964).

25. B. Krishnapuram, L. Carin, M. A. T. Figueiredo, and A. J. Hartemink, Sparse multinomial logistic regression: Fast algorithms and generalization bounds. *IEEE Trans. Pattern Anal. Mach. Intell.* **27,** 957–968 (2005).

26. I. J. Pence, C. A. Patil, C. A. Lieber, and A. Mahadevan-Jansen, Discrimination of liver malignancies with 1064 nm dispersive Raman spectroscopy. *Biomed. Opt. Express* **6,** 2724–37 (2015).

27. P. R. Murray, E. J. Baron, J. H. Jorgensen, and M. L. Landry, *Manual of Clinical Microbiology*. (ASM Press, 2007).

28. C. L. Ventola, The antibiotic resistance crisis: part 1: causes and threats. *P T A peer-reviewed J. Formul. Manag.* **40,** 277–83 (2015).

29. J. C. Post, *et al.* Molecular analysis of bacterial pathogens in otitis media with effusion. *JAMA* **273,** 1598–1604 (1995).

30. G. M. Matar, N. Sidani, M. Fayad, and U. Hadi, Two-step PCR-based assay for identification of bacterial etiology of otitis media with effusion in infected Lebanese children. *J. Clin. Microbiol.* **36,** 1185–1188 (1998).

31. M. G. Rayner, *et al.* Evidence of bacterial metabolic activity in culture-negative otitis media with effusion. *JAMA* **279,** 296–9 (1998).

32. M. W. van der Woude and A. J. Bäumler, Phase and Antigenic Variation in Bacteria Phase and Antigenic Variation in Bacteria. *Clin. Microbiol. Rev.* **17,** 581–611 (2004).

33. E. R. Lafontaine, *et al.* Expression of the Moraxella catarrhalis UspA1 Protein Undergoes phase Variation and Is Regulated at the Transcription Level. *J. Bacteriol.* **183,** 1540–1551 (2001).

34. A. Oust, *et al.* Fourier Transform Infrared and Raman Spectroscopy for Characterization of Listeria monocytogenes Strains. *Society* **72,** 228–232 (2006).

35. E. Leibovitz, A. Broides, D. Greenberg, and N. Newman, Current management of pediatric acute otitis media. *Expert Rev. Anti. Infect. Ther.* **8,** 151–161 (2010).

36. Z. Grossman, *et al.* Antibiotic prescribing for upper respiratory infections: European primary paediatricians' knowledge, attitudes and practice. *Acta Paediatr. Int. J. Paediatr.* **101,** 935–940 (2012).

37. B. Zielnik-Jurkiewicz and A. Bielicka, Antibiotic resistance of Streptococcus pneumoniae in children with acute otitis media treatment failure. *Int. J. Pediatr. Otorhinolaryngol.* **79,** 2129–2133 (2015).

38. R. Dagan, Treatment of acute otitis media - Challenges in the era of antibiotic resistance. *Vaccine* **19,** 2–9 (2000).

# CHAPTER 4

## 4. DRUG-RESISTANT *STAPHYLOCOCCUS AUREUS* STRAINS REVEAL DISTINCT BIOCHEMICAL FEATURES WITH RAMAN MICROSPECTROSCOPY

### 4.1 Abstract

*Staphylococcus aureus* is a leading cause of hospital-acquired infections, such as bacteremia, pneumonia, and endocarditis. Treatment of these infections can be challenging since strains of *S. aureus*, such as methicillin-resistant *S. aureus* (MRSA), have evolved resistance to antimicrobials. Current methods to identify infectious agents in hospital environments often rely on time-consuming, multi-step culturing techniques to distinguish problematic strains (i.e. antimicrobial resistant variants) of a particular bacterial species. Therefore, a need exists for a rapid, label-free technique to identify drug-resistant bacterial strains to guide proper antibiotic treatment. Here, our findings demonstrate the ability to characterize and identify microbes at the subspecies level using Raman microspectroscopy, which probes the vibrational modes of molecules to provide a biochemical "fingerprint". This technique can distinguish between different isolates of species such as *Streptococcus agalactiae* and *S. aureus*. To determine the ability of this analytical approach to detect drug-resistant bacteria, isogenic variants of *S. aureus* including the comparison of strains lacking or expressing antibiotic resistance determinants were evaluated. Spectral variations observed

may be associated with biochemical components such as amino acids, carotenoids, and lipids. Mutants lacking carotenoid production were distinguished from wild-type *S. aureus* and other strain variants. Furthermore, spectral biomarkers of *S. aureus* isogenic bacterial strains were identified. These results demonstrate the feasibility of Raman microspectroscopy for distinguishing between various genetically distinct forms of a single bacterial species *in situ*. This is important for detecting antibiotic-resistant strains of bacteria and indicate the potential for future identification of other multi-drug resistant pathogens with this technique.

## 4.2 Introduction

Healthcare-associated infections (HAIs), i.e. infections that patients obtain while receiving medical or surgical treatment in a healthcare facility, are a major threat to patient health. They have led to high rates of morbidity and mortality and annual healthcare costs of nearly $45 billion.[1] The most common HAIs in U.S. acute care hospitals include but are not limited to pneumonia, surgical site infections, bloodstream infections, and gastrointestinal illness.[2] Among surgical complications, wound infections account for 29% of these events and over 10% of all adverse events.[3]

Infections caused by *Staphylococcus aureus* are of particular interest since they are a major burden to U.S. hospitals specifically for high-risk patients. In one study, hospitalized patients with an *S. aureus* infection experienced three times the length of hospital stay, three times the amount of total charges, and five times

the risk of in-hospital death compared to patients that did not have this type of infection.[4] The development of antibiotic-resistant strains such as methicillin-resistant *S. aureus* (MRSA) further contribute to this growing problem by creating an additional barrier against treatment. Methicillin resistance is mediated by the staphylococcus cassette chromosome (SCC mec), which encodes for penicillin binding protein PBP2a.[5,6] Although the number of nosocomial infections by *S. aureus* increased by 62% per year, the number of MRSA infections in hospitals increased by 119% per year from 1999-2005.[7] This rapid increase in antibiotic resistance motivates the need of pathogen surveillance for early detection of outbreaks in hospital and community associated infections.

One subpopulation of bacteria that causes persistent infections in patients with acute and chronic illnesses are bacterial variants of *S. aureus* called small-colony variants (SCVs). These SCVs display increased tolerance to particular classes of antibiotics such as aminoglycosides and therefore often arise in response to therapeutic intervention.[8] These SCVs, which take on fastidious growth requirements, present with a phenotype that is different from their parent strain characterized by colonies with decreased pigmentation that are approximately one-tenth the size of wild-type *S. aureus* colonies.

The current approach for detecting and identifying bacterial strains like *S. aureus* in clinical samples involves a multi-step process to evaluate specific targets of the sample. Typically, samples are cultured on blood agar and characterized based on morphological features, as seen through microscopy, and biochemical tests that evaluate biosynthesis pathways. Identification of bacteria at the species

level and determination of antibiotic susceptibility requires additional targeted biochemical testing (e.g. catalase test, coagulase test, and DNase test to identify *S. aureus*) since specificity is critical for proper diagnosis and treatment. These techniques are time-consuming due to incubation times and subsequent manual tests requiring interpretation of biochemical reactions. In addition to atypical colony morphologies, SCVs require extended culture periods and various biochemical assays to accurately detect and identify. These tests, which evaluate the response from various biochemical reactions, may be difficult to interpret due to altered metabolic pathways of SCVs.[9] Furthermore, the gold standard for determining whether bacteria are susceptible/resistant to specific antimicrobials is through antimicrobial susceptibility testing (AST), which evaluates the isolated bacteria with various antimicrobials for growth inhibition. Specific strategies that promote growth and minimize reversion to normal colony phenotypes have also been developed to test AST from *S. aureus* SCVs, commonly seen in chronic infections.[10] Again, these approaches can be time-consuming (days to weeks), involve bacterial cultures that have limited growth, and are challenging to interpret especially for mutant strains. More recently, a custom-built automated dark-field microscope was used to acquire time-lapse images of bacteria flowing in a multichannel fluidic cassette to evaluate phenotypical parameters to identify bacterial pathogens from patients affected by ventilator-associated pneumoniae[11] and characterize various *S. aureus* strains associated with antibiotic resistance and susceptibility.[12] Although this approach obtained 100% sensitivity and 97%

specificity for detection of high-risk pneumoniae organisms, it required expert image interpretation to analyze antibiotic susceptibility testing.

To obtain near 100% specificity for bacterial identification, researchers routinely rely on polymerase chain reaction (PCR) to amplify deoxyribonucleic acid (DNA) from bacteria.[13] However, PCR is dependent on target genes, that may not be available for specific bacterial mutants, is vulnerable to contamination, and is not able to distinguish between live versus dead bacteria in a clinical sample.[14] These factors negatively affect the sensitivity of PCR for accurate identification of bacteria.

Optical techniques such as fluorescence spectroscopy have previously been used for detecting bacteria in a saline solution.[15] Although the authors report identification of *S. aureus*, fluorescence fingerprints of *S. aureus* and other strains presented overlapping features. More recently, a similar study evaluated fluorescence spectroscopy for characterization of clinically important bacteria, including *S. aureus*, and found that tryptophan could be used for detecting bacteria, but not for specifically identifying *S. aureus*.[16] Fluorescence spectroscopy is unable to provide specific biochemical features important for discrimination of bacteria and may be further complicated with intrinsic fluorophores that may saturate system detectors. An accurate biochemical characterization of these strains is critical for accurate detection and discrimination amongst other species and isogenic variants. Although other UV wavelengths could be used as an excitation source to detect the resonance effect of the absorption band at 478 nm[17] for staphyloxanthin, the main pigment in WT *S. aureus*, there is an increased risk

of deleterious effects such as fluorescence saturation and breaking of covalent bonds. This could cause misrepresentation of the biochemical profile of the bacterial strain and make it challenging for accurately discerning bacteria at the species level. Therefore, there is a need for a rapid (seconds to minutes), non-invasive technique able to accurately detect and identify bacterial species and drug-resistant strains to guide proper treatment.

Raman spectroscopy (RS) is an inelastic light scattering technique that provides molecular specificity and has been used extensively for characterizing bacteria.[18–22] Its ability to provide accurate and reproducible spectral information of a sample, perform rapid measurements, and create a biochemical profile of a sample have paved the way for biological applications. Biochemical features such as proteins, DNA, lipids, and polysaccharides have been detected using RS to probe bacterial components at the single-cell level.[23] Using confocal Raman microspectroscopy, metabolic changes in microorganisms have been characterized based on the high spatial resolution (~1 μm) the technique provides. Studies have been performed to evaluate changes in cell culture composition such as an increase in polysaccharides during the cell cycle process, highlighting the diversity in microbial subpopulations.[24,25] Researchers have also investigated the biochemical response of antibiotics at varied concentrations on bacteria using Raman microspectroscopy.[26] Furthermore, bacterial strains at the subspecies level have been characterized using Raman microspectroscopy and successfully classified with a support vector machine (SVM) algorithm.[27,28] This study builds upon previous research as one of the first, to our knowledge, to investigate

isogenic variants of bacteria of clinical importance using Raman microspectroscopy. More specifically, the hypothesis that Raman microspectroscopy could discriminate wild-type versus single gene mutant strains of the same species of bacteria using a label-free, non-invasive approach was tested and evaluated. The goal of this work is to utilize Raman microspectroscopy to characterize the spectral features of different isolates of the same species and demonstrate the ability of this technique to distinguish between them. Specifically, isogenic and small colony variants of *S. aureus* were investigated *in situ* using spectral regions for analysis. Our results show that Raman microspectroscopy can be used to identify genetic variants of *S. aureus*, discriminate between methicillin-resistant and methicillin-sensitive strains, and determine biochemical features important for discrimination of various bacterial strains.

## 4.3 Materials & Methods

### 4.3.1 Bacterial Strains

Multiple pathogens were characterized using Raman microspectroscopy and their biochemical profile was used to determine if clinically relevant strains could be identified. The following bacteria were evaluated using Raman microspectroscopy: wild-type *Staphylococcus aureus* (WT JE2), *Streptococcus agalactiae* (also known as Group B *Streptococcus,* GBS), GBS 1084 and GBS 37, and nontypeable *Haemophilus influenzae* (ATCC #49766).

*S. aureus* mutants were also investigated using Raman microspectroscopy. One of these genetic variants included Δ*mecA,* which lacked resistance to β-lactam antibiotics and is commonly referred to as methicillin-sensitive *S. aureus* (MSSA).[29,30] The second *S. aureus* mutant investigated was Δ*ispA,* a geranyltransferase gene, which generates non-pigmented bacterial colonies.[31] The third *S. aureus* gene studied, *fmtA*, is a member of the *S. aureus* core cell wall stimulon and inactivation of *fmtA* (Δ*fmtA*) affects the cell wall structure[32] and diminishes the ability of *S. aureus* to form biofilms.[33] The fourth *S. aureus* mutant studied included Δ*crtM*, which encodes for dehydrosqualene synthase and disrupts biosynthesis of carotenoids, resulting in non-pigmented bacterial colonies.[34] The fifth *S. aureus* mutant, Δ*SAUSA300-0918*, where *SAUSA300-0918* encodes for glycerolipid metabolism and is involved in the formation of membrane glycolipids. *S. aureus* small-colony variants (SCVs) were also examined to determine if Raman characterization could be used to biochemically discriminate this type of antibiotic-tolerant variant from other *S. aureus* strains. The SCVs tested included a cytochrome double knockout strain Δ*cyd* Δ*qox*[35] as well as a heme biosynthesis-deficient strain Δ*hemB*[36] and a menaquinone biosynthesis-deficient strain Δ*menB.*[37] The parental strain of these SCVs, Newman[38], was also spectrally analyzed using Raman microspectroscopy. These strains were summarized (Table 4.1) and streaked on Mueller-Hinton agar plates for comparison (Figure 4.1).

Each strain was streaked onto Mueller-Hinton (MH) agar, which was prepared by suspending 11 g of MH (BD, Franklin Lakes, NJ) powder and 7.5 g

(15% agar/L) of agar (Thermo Fisher Scientific, Waltham, MA) in 500 mL of distilled water while heating (180 ˚F) and stirring. The mixture was then autoclaved at 121 ˚C for 10 minutes. After plating, bacteria were incubated for 24 hours at 37 ˚C.

Table 4.1: Summary of S. aureus strains evaluated using Raman microspectroscopy.

| Strain | Description | Pigmentation | Drug-Resistant/Sensitive |
|---|---|---|---|
| **JE2 (wild-type)** | Methicillin-resistant *S. aureus* | + | Methicillin-resistant; Aminoglycoside-sensitive |
| **Δ*crtM*** | *crtM* gene codes for dehydrosqualene synthase; Δ*crtM* mutant disrupts biosynthesis pathway of carotenoids | - | Methicillin-resistant; Aminoglycoside-sensitive |
| **Δ*fmtA*** | *fmtA* gene is part of the core wall stimulon; identified as a factor for methicillin-resistance, and involved in biofilm formation; Δ*fmtA* leads to increased sensitivity to antibiotics | + | Methicillin-sensitive; Aminoglycoside-sensitive |
| **Δ*ispA*** | *ispA* encodes for geranyltransferase gene; Δ*ispA* causes non-pigmented colonies | - | Methicillin-resistant; Aminoglycoside-sensitive |
| **Δ*mecA*** | *mecA* encodes for resistance to non-β-lactam antibiotics; Δ*mecA* increases sensitivity to antibiotics | + | Methicillin-sensitive; Aminoglycoside-sensitive |
| **Δ*SAUSA300-0918*** | *SAUSA300-0918* encodes for glycerolipid metabolism; Δ*SAUSA300-0918* causes a decrease in lipid production | + | Methicillin-resistant; Aminoglycoside-sensitive |
| **Newman** | Methicillin-sensitive *S. aureus* | + | Methicillin-sensitive; Aminoglycoside-sensitive |
| **Δ*cyd* Δ*qox*** | *cyd/qox* code for cytochromes; reduced proton motive force creates aminoglycoside-resistance | + | Methicillin-sensitive; Aminoglycoside-resistant |

| | | | |
|---|---|---|---|
| **Δ*hemB*** | *hemB* is a biosynthetic gene for hemin biosynthesis; Δ*hemB* produces a heme biosynthesis-deficient strain; reduced proton motive force creates aminoglycoside-resistance | + | Methicillin-sensitive; Aminoglycoside-resistant |
| **Δ*menB*** | *menB* encodes for dihydroxynaphthoic acid synthetase; Δ*menB* produces a menaquinone biosynthesis-deficient strain; reduced proton motive force creates aminoglycoside-resistance | + | Methicillin-sensitive; Aminoglycoside-resistant |

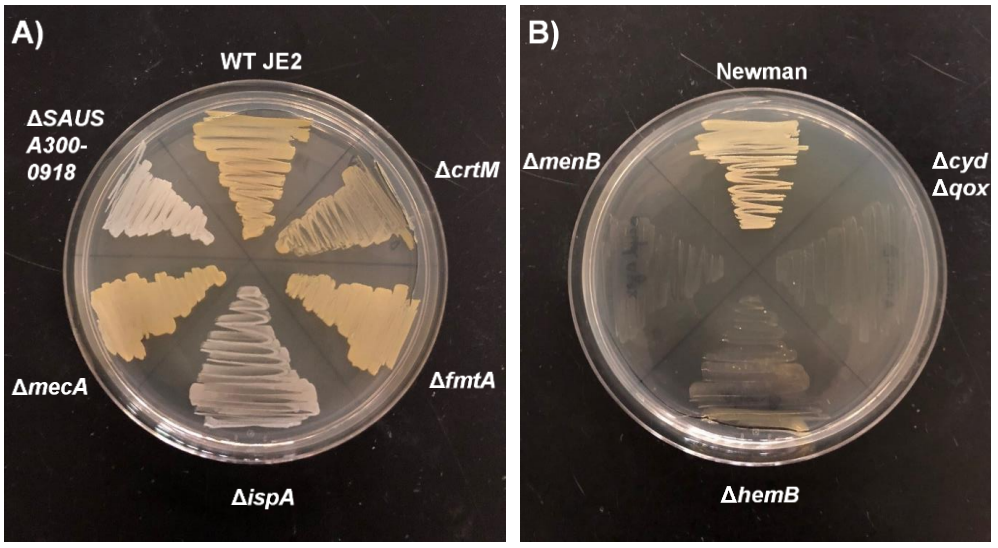


Figure 4.1: Strains of *S. aureus* streaked onto MH agar. (A) *S. aureus* wild-type (WT) and mutants Δ*crtM*, Δ*fmtA*, Δ*ispA*, Δ*mecA*, and Δ*SAUSA300-0918* streaked on a MH agar plate. (B) *S. aureus* Newman and small colony variant (SCV) strains Δ*cyd* Δ*qox*, Δ*hemB*, and Δ*menB* streaked on a MH agar plate. Streaked plates were incubated at

4.3.2 Raman Microspectroscopy

Acquisition of Raman spectra was performed using a Raman microscope (inVia Raman Microscope, Renishaw plc, Gloucestershire, UK) with a 785 nm laser excitation (Renishaw plc, Gloucestershire, UK). To interrogate the bacterial colonies, a 100X (N PLAN EPI, NA=0.85, Leica, Weltzlar, Germany) objective was used to focus a laser spot directly on the bacterial colony on the agar surface at 27 mW. Although the spot size of the beam was theoretically calculated to be ~ 1 µm based on the beam spot diameter equation, experimentally the beam spot was ~30-40 µm in diameter when focused on the sample. Based on Monte Carlo simulations to characterize the effects of beam width on penetration depth in tissue (which may be more highly scattering compared to agar and bacteria), a uniform penetration depth is achievable when the beam radius is three times the penetration depth.[39] Therefore, the depth at which there is an estimated uniform penetration depth at the beam center is ~5-7 µm, which would hypothetically allow signal collection from hundreds to thousands of *S. aureus* bacterial cells in the beam path. Raman scattered light was detected through the same objective, then passed through a 55 µm slit and dispersed by a holographic grating (1200 lines/mm) onto a thermoelectrically cooled (-70 ˚C) deep-depleted, CCD that provided ~1 $cm^{-1}$ spectral resolution. System alignment and light throughput to the sample was confirmed before and after experimental measurements with an internal silicon standard at 520 $cm^{-1}$ and laser power at the sample.

Spectral measurements included three acquisitions per spot, three spots per colony, and three colonies per bacteria for *S. aureus* mutants for a total of 162

spectra with 917 wavenumbers per spectrum. All Raman spectra for the *S. aureus* genetic variants and SCVs were collected from different bacterial colonies of the same growth. Measurement parameters for SCVs included three spots per colony and three colonies per bacterial strain for a total of 36 spectra with 917 wavenumbers per spectrum. First, the 785 nm laser was focused onto the bacterial colony for a 30 second photobleach of the sample to minimize fluorescence from MH agar. Subsequent spectral acquisition parameters included a 15 second exposure with 7 accumulations from 700-1800 $cm^{-1}$. Cosmic ray removal from collected Raman spectra was performed using a custom MATLAB script (Mathworks, Natick, MA, USA). Raman spectra were then processed to remove background fluorescence using a least squares modified polynomial fitting algorithm[40] and smoothed for noise with a second-order Savitsky-Golay filter.[41] To optimize background fluorescence subtraction, each raw spectrum from SCVs was divided into three segments. These segments included: (a) 700 – 1141 $cm^{-1}$ (b) 1141 – 1477 $cm^{-1}$ and (c) 1470 – 1700 $cm^{-1}$. The 7 $cm^{-1}$ overlap of regions (b) and (c) was adjusted by using only the fitting from 1478 – 1700 $cm^{-1}$ for region (c). Segment (a) used an $8^{th}$ degree modified polynomial fitting compared to segments (b) and (c), which implemented a $5^{th}$ degree modified polynomial fit for fluorescence subtraction. After spectral processing was performed for SCV data, spectral segments were reconstructed into one Raman spectrum for each measurement. Post-processed spectra were mean-normalized to each individual Raman spectrum for comparative analysis.

### 4.3.3 Spectral Data Analysis

Mean-normalized Raman spectra of bacterial colonies were analyzed for classification. For preliminary analysis, peak ratios were calculated based on distinct Raman peaks and the phenylalanine peak across all *S. aureus* mutants and SCVs. The means of the peak ratios were compared using a one-way analysis of variance (ANOVA) and corrected using a Tukey test to determine significance for multiple comparisons. To limit bias from hand-selecting peaks, a full-spectrum principle component analysis (PCA) was performed on the Raman spectra of the *S. aureus* mutants and SCVs. Since spectra from these pathogens included more spectral features (variables) compared to observations, PCA scores and correlation coefficients (loadings) were calculated using singular value decomposition (SVD).[42] Implementation of SVD for PCA reduces the large volume of data and minimizes the loss of precision that is typically seen when using the covariance matrix approach. To use PCA via SVD, the means of the mean-normalized spectral data matrix were subtracted from each dimension to center the data. Then, the SVD of the mean-centered matrix was calculated to determine the eigenvalues and eigenvectors to interpret the scores and loadings of the original input matrix.

While the full-spectrum analysis provided a global picture of the Raman data, the model was tested to prevent over fitting the data since there are more spectral features than measurements. Therefore, loadings, which measure the correlation between the principal component score and the original variables, were used to identify spectral regions of interest for downstream analysis. The use of

PCA loadings (correlation coefficients) to determine important spectral features for classification has been previously used for identifying molecular distributions in biological samples.[43] The approach for determining these spectral regions of interest involved the following steps. First, the two maximum (absolute value) correlation coefficients from the first two PCs were identified. If the spectral region between any of those peaks contained correlation coefficients that were at least 50% of the second maximum correlation coefficient and the region in consideration was not greater than 15% of the total features available (wavenumbers), then that spectral region could be used for evaluation. Otherwise, the spectral region of interest would be defined by the width of the peak determined by the PC correlation coefficient.

After the spectral regions were designated for both *S. aureus* mutants and SCVs, PCA via SVD was performed on these regions. The PC scores from each spectral region were used for a discrimination analysis. A variant of Fisher's linear discriminant analysis, quadratic discriminant analysis (QDA), was applied to determine the ability of each designated spectral region to classify the various microorganisms. The use of QDA has been implemented in applications such as classifying Raman spectra of human cancer cell lines[44] and Raman imaging of naïve versus activated T-cells.[45] First, a quadratic classifier was created based on designated classes (each of the *S. aureus* mutants and SCVs) using the PCA scores from each spectral region as input parameters. Next, the coefficients of the respective quadratic boundaries were determined. The coefficients (K, constant; L, linear; Q, quadratic) were used in equation 4.1 to generate the curves to

determine boundaries for discrimination amongst classes for each *S. aureus* mutants and SCVs.

$$K + [x_1\ x_2]L + [x_1\ x_2]Q\begin{bmatrix}x_1\\x_2\end{bmatrix} = 0 \qquad (4.1)$$

## 4.4 Results & Discussion

### 4.4.1 RS can Differentiate Two Virulent Strains of Group B *Streptococcus* (GBS).

Raman microspectroscopy was used to characterize and differentiate various bacterial species such as wild-type *S. aureus* (WT JE2), *Streptococcus agalactiae*, commonly known as group B *Streptococcus* (GBS), and *Haemophilus influenzae* (Figure 4.2). The strain WT JE2 presents two main peaks at 1159 $cm^{-1}$ and 1523 $cm^{-1}$ resembling carotenoid bands, which we tentatively assigned as C-C stretching and C=C stretching, respectively, based on previous RS measurements of *S. aureus*[46] (Figure 4.2). In addition to WT JE2, two strains of GBS were spectrally measured (GBS 1084 and GBS 37). For GBS 1084, two unique peaks at 1121 $cm^{-1}$ and 1504 $cm^{-1}$ were tentatively assigned as C-C stretching and C=C stretching, respectively, based on a similar 12 double bonded polyene[47] (Figure 4.2). These resonantly enhanced peaks may be related to the GBS pigment that is composed of a 676-Da ornithine rhamno-polyene with a linear chain of 12 conjugated double bonds.[48] As can be seen in figure 4.2, these two narrow peaks for GBS 1084 are red-shifted in the Raman spectrum compared to similar bands (carotenoids) for WT JE2. The decrease in stretching frequency may

be due to a higher conjugation of the 12 double bonds in GBS 1084 pigment compared to the pigmentation in WT JE2 (staphyloxanthin) that does not contain as much conjugation throughout the molecule. A frequency red-shift caused by conjugation length was previously found in Raman spectra of *t*-butyl capped polyenes for higher *N*-enes, where *N* is the number of double bonds of a molecular structure.[47] For GBS 37, a non-pigmented strain, various biochemical features assigned as pyrimidine ring breathing (783 $cm^{-1}$) and C-O-O symmetric and asymmetric stretching in peptidoglycan (1379 $cm^{-1}$) were observed (Figure 4.2). *H. influenzae* shows distinct Raman features such as tyrosine ring breathing (852 $cm^{-1}$) and $CH_2$ fatty acids twisting (1299 $cm^{-1}$) that are important for identification compared to the other bacterial spectra[49] (Figure 4.2). The dramatic spectral differences between the two strains of GBS, *H. influenzae*, and WT JE2, indicate the potential of Raman microspectroscopy to distinguish bacterial isolates at the subspecies level. This finding motivates the application of this technique to discriminate single genetic variations in *S. aureus* mutants.

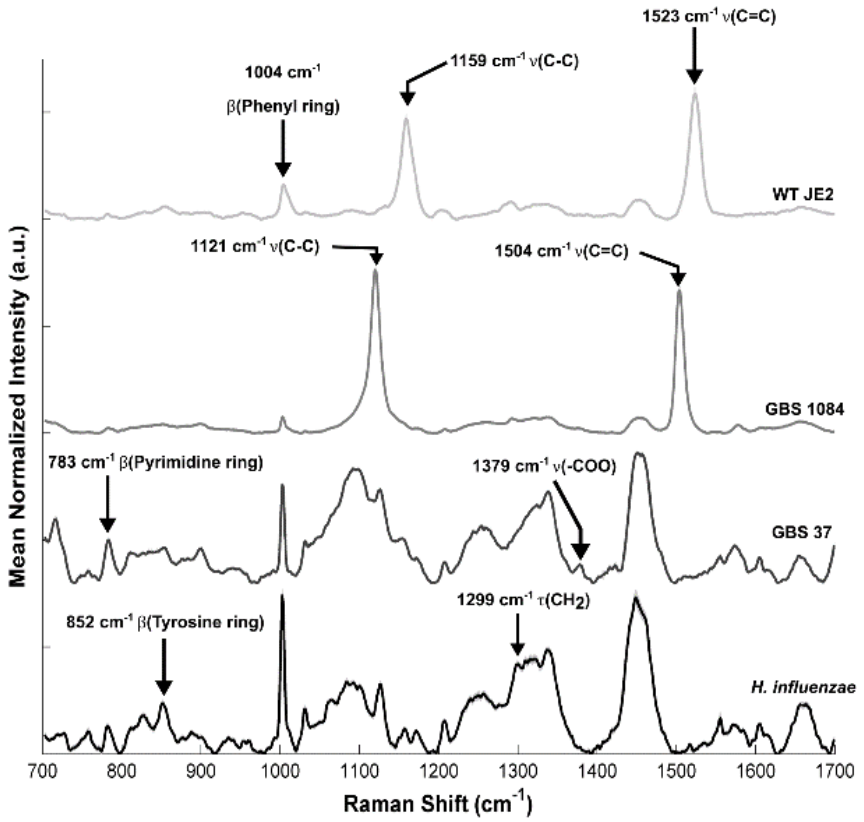


Figure 4.2: Mean ± standard deviation Raman spectra of various bacteria. Spectral signatures of bacteria shown include WT JE2, GBS 1084, GBS 37, and *H. influenzae*. Different spectral features are identified for each bacterial measurement. β, breathing; τ, twisting; ν, stretching.

4.4.2 Genetically Modified Strains of *S. aureus* are Distinguished from WT.

Various *S. aureus* mutants (WT JE2, Δ*crtM*, Δ*ispA*, Δ*SAUSA300-0918*, Δ*mecA*, and Δ*fmtA*) were studied using Raman microspectroscopy. To test the ability of using this technique to distinguish between single gene mutations, Raman spectra from *S. aureus* Δ*crtM* are analyzed. This mutant was chosen as a positive control since deletion of *crtM* disrupts biosynthesis of the carotenoid staphyloxanthin, which is responsible for the golden pigment of *S. aureus* and predicted to contribute to the two main *S. aureus* Raman peaks at 1159 $cm^{-1}$ and 1523 $cm^{-1}$. Figure 4.3 shows the absence of these Raman peaks in the Δ*crtM* mutant compared with the strong presence of these features in WT JE2 spectra, which supports the assignment to this specific carotenoid pigment that differs between mutant samples (Figure 4.3). These carotenoids are not only an important factor for the cell membrane's integrity, but also play a role in the virulence of *S. aureus*.[34] Another mutant chosen for this study includes Δ*ispA,* an unpigmented *S. aureus* strain predicted to display a similar Raman profile to that of Δ*crtM* due to the lack of staphyloxanthin production. The phenotypic profile of this mutant was visually indistinguishable from that of Δ*crtM* (Figure 4.4A). Finally, to assess whether a unique lipid signature could be detected in *S. aureus* using Raman microspectroscopy, Δ*SAUSA300-0918*, a putative lipid metabolism mutant, was compared to the parental strain. To quantify the various Raman peaks seen in the *S. aureus* mutants, peak ratios of mean-normalized intensities highlighted by the gray bands in Figure 4.4A, were calculated. The lipid mutant strain (Δ*SAUSA300-0918*) was evaluated using a peak ratio of 876 $cm^{-1}$ to 1004 $cm^{-1}$ (asymmetric

stretching $N^{+}(CH_3)_3$/phenyl ring breathing as part of phenylalanine). The Raman peak at 876 $cm^{-1}$ has been shown to be relevant for characterizing membrane lipids, specifically phosphatidylcholine.[50] This lipid peak ratio demonstrates a significant ($p<0.0001$) decrease when Δ*SAUSA300-0918* is compared to *S. aureus* mutants and WT JE2 (Figure 4.4B). Since this gene is part of the glycerolipid metabolism pathway in *S. aureus*, deletion of the gene could negatively impact lipid production related to cell wall composition.

To determine the differences in pigmentation in *S. aureus* mutants, the peak ratio of 1523 $cm^{-1}$ to 1004 $cm^{-1}$ (carotenoid/phenylalanine) was analyzed. This peak ratio shows a statistically significant ($p<0.0001$) increase in pigmentation due to staphyloxanthin in WT JE2 as compared to Δ*ispA,* Δ*crtM*, and the other *S. aureus* mutants (Figure 4.4C). In addition, the lack of pigmentation in Δ*ispA* and Δ*crtM* due to their respective genetic mutations is confirmed using the peak ratio described. These results confirm the ability of Raman microspectroscopy to interrogate bacterial colonies and distinguish between strains of *S. aureus* with a one-gene mutation. Based on these findings, we sought to determine whether antibiotic-resistant and sensitive mutants could be distinguished using Raman microspectroscopy *in situ* as this ability would have significant clinical implications.

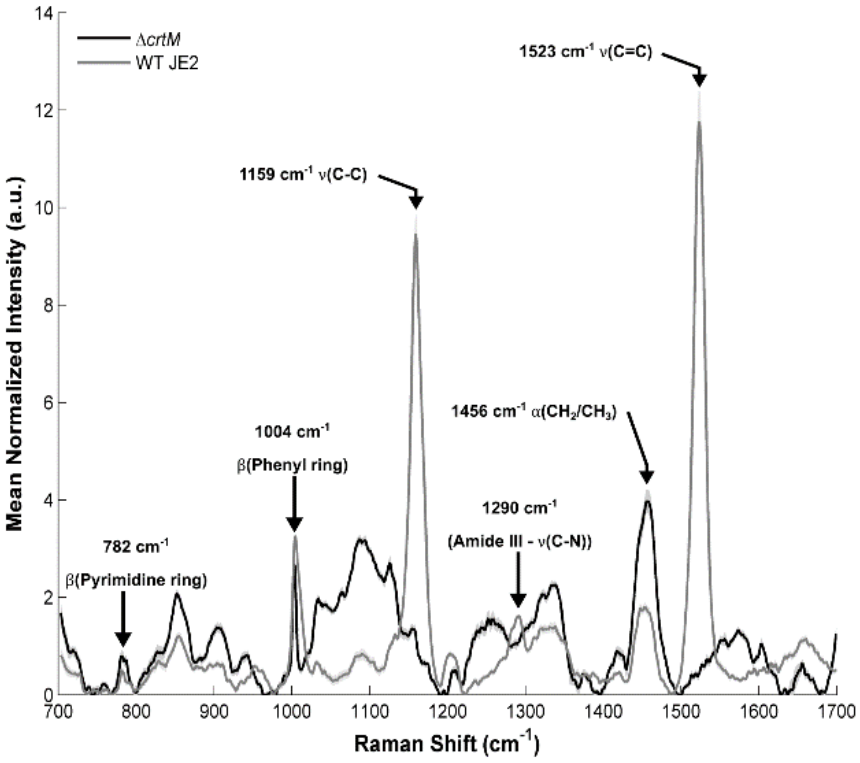


Figure 4.3: Mean ± standard deviation Raman spectra of WT JE2 and ΔcrtM, a S. aureus mutant that lacks pigmentation. Two major Raman bands, located at 1159 $cm^{-1}$ ν(C-C) and 1523 $cm^{-1}$ ν(C=C), are present in WT JE2 and absent in ΔcrtM. α, bending; β, breathing; ν, stretching.

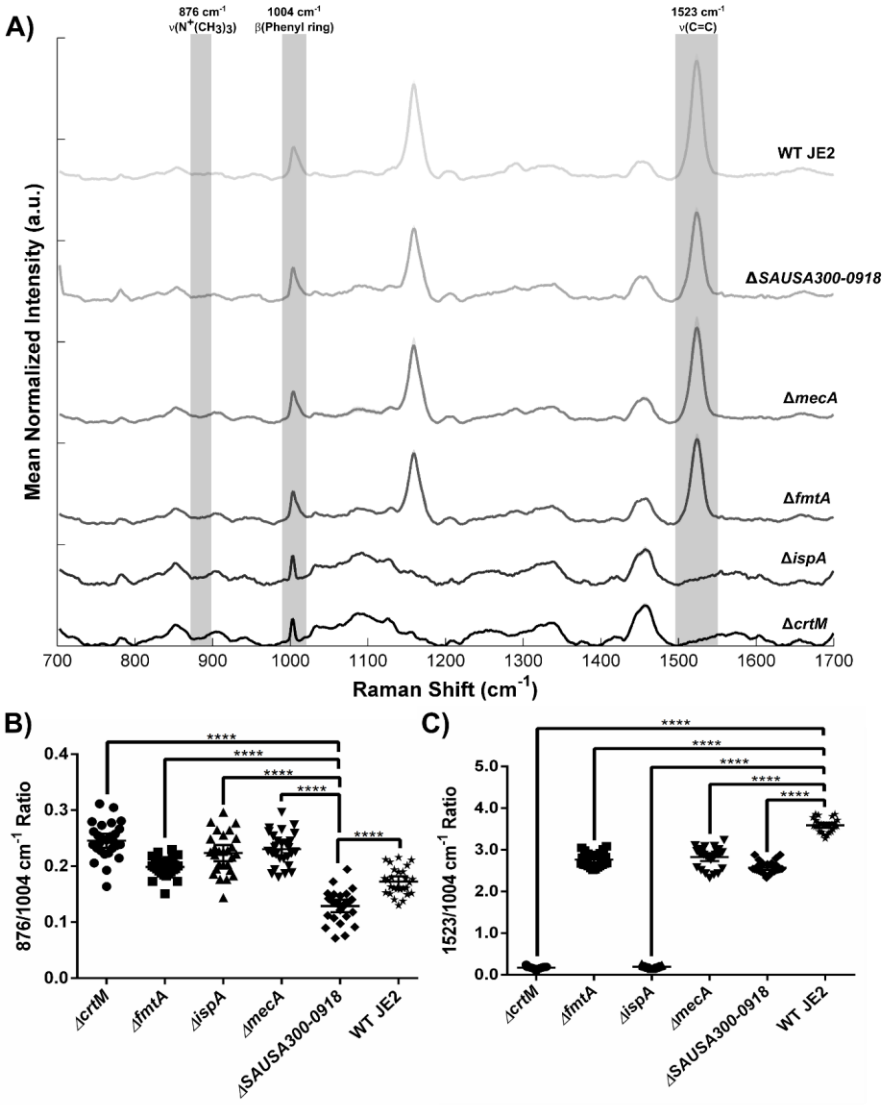


Figure 4.4: Comparison of S. aureus mutants based on pigmentation and lipid features. A) Mean ± standard deviation Raman spectra of WT JE2 and S. aureus mutants. B) Mean peak ratio of 876 $cm^{-1}$ $\nu(N^{+}(CH_3)_3)$ and 1004 $cm^{-1}$ $\beta$(phenyl ring) as part of phenylalanine with 95% confidence interval calculated using a one-way ANOVA performed to compare mutants vs. WT JE2. C) Mean peak ratio of 1523 $cm^{-1}$ $\nu$(C=C) and 1004 $cm^{-1}$ $\beta$(phenyl ring) with 95% confidence interval calculated using a one-way ANOVA performed to compare mutants vs. WT JE2. ****=p<0.0001. $\beta$, breathing; $\nu$, stretching.

4.4.3 Antibiotic-resistant *S. aureus* Strains can be Identified using RS.

Clinical relevance of this technology was evaluated by comparing methicillin-sensitive mutants Δ*mecA* and Δ*fmtA* to their methicillin-resistant parental strain using Raman microspectroscopy. A full-spectrum analysis of *S. aureus* mutants was performed using principal component analysis (PCA), a non-supervised statistical method that reduces high-dimensional data by converting it to an orthogonal vector space based on projections (principal components) that explain the most variance. The results from this approach show that the unpigmented strains (Δ*crtM* and Δ*ispA*) can be distinguished from methicillin-sensitive strains (Δ*mecA* and Δ*fmtA*), Δ*SAUSA300-0918*, and WT JE2 (data not shown) with high accuracy. The new coordinates for the original spectral data determined from PCA were then input into a quadratic discriminant analysis (QDA) classifier to demonstrate the ability of Raman microspectroscopy to distinguish between the strains described.

While a full-spectrum analysis can be used to reduce high-dimensional data to a few linear combinations of variables called principal components, the biochemical relevance of these components is unknown. To identify spectral features important for discrimination, correlation coefficients (loadings) of the components scores were used to determine how much of the variation of each variable is explained by each principal component (PC). Rather than using a single wavenumber peak, a more biochemically rich comparison can be made by utilizing regions of wavenumbers identified based on the magnitude of the correlation coefficients computed for each feature. Combining the selected spectral regions

from the PCA loadings that explain larger variances in the data minimizes overfitting, therefore creating a more reliable model for identification of biomarkers important for discrimination.

For the *S. aureus* mutants, the highest PC1 correlation coefficient was observed at 1523 $cm^{-1}$ followed by that at 1159 $cm^{-1}$ as determined by plotting the correlation coefficients (PC loadings) versus the Raman shift (Figure 4.5A). Since these two wavenumbers both described pigmented versus unpigmented *S. aureus* mutants, the highest PC1 feature was used to distinguish between these strains (1523 $cm^{-1}$). The highest PC2 correlation coefficient was located at 781 $cm^{-1}$ and the second highest was at 910 $cm^{-1}$. The spectral regions of analysis identified for the *S. aureus* mutant data were determined by evaluating the magnitudes of the correlation coefficients of PC1 and PC2. The first spectral region of interest was 765-934 $cm^{-1}$ (region 1), which contained PCA correlation coefficients that were at least 50% of the second highest correlation coefficient in PC2 located at 910 $cm^{-1}$ (Figure 4.5B). This threshold was part of the selection criteria for a spectral region. Since the second highest PC1 correlation coefficient (1159 $cm^{-1}$) was not used for analysis, the next highest PC2 correlation coefficient, 1431-1464 $cm^{-1}$, was selected as the second spectral region of interest (region 2) (Figure 4.5B). The third spectral region of interest (region 3) was 1495-1544 $cm^{-1}$, based on the maximum PC1 feature (1523 $cm^{-1}$) (Figure 4.5B).

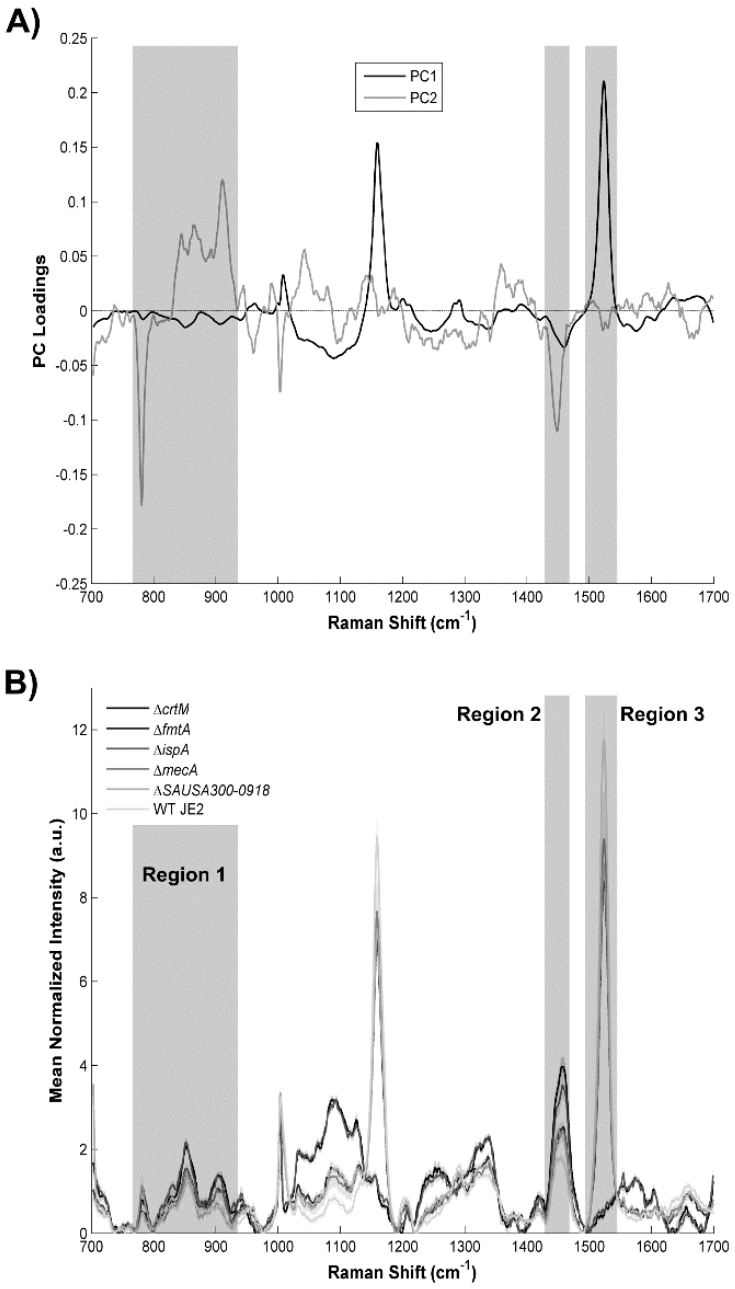


Figure 4.5: Spectral region analysis of *S. aureus* mutants based on PC correlation coefficients. (A) Gray bands identify regions used for analysis of WT JE2 and *S. aureus* mutants as determined by PC correlation coefficients. (B) Spectral regions, indicated by gray bands, used for discriminant analysis of *S. aureus* mutants and WT JE2.

A subsequent PCA using singular value decomposition (PCA-SVD), which has a higher precision in calculating the eigenvectors by not using the covariance matrix, was calculated based on the determined spectral regions. The scores from this analysis were used to fit a quadratic discriminant analysis (QDA) model for each spectral region. A quadratic discriminant analysis (QDA) analysis based on PCA singular value decomposition (PCA-SVD) was implemented to discriminate between the *S. aureus* mutants and classify spectra. Since the decision boundaries for specific spectral regions may be non-linear, a quadratic function analysis was used. Boundaries generated from the QDA fit based on spectral region 1 (765-934 $cm^{-1}$) present 100% classification of wild-type (WT) JE2, methicillin-sensitive strains (Δ*fmtA* and Δ*mecA*), Δ*SAUSA300-0918*, and non-pigmented strains (Δ*crtM* and Δ*ispA*) when compared to each other (Figure 4.6A-B). These results were based on PC1 and PC2, which explained 71.60% and 17.40% of the data within this spectral region, respectively. Various biochemical features in region 1 are assigned to cytosine (782 $cm^{-1}$), tyrosine (853 $cm^{-1}$), and C-O-C stretching and teicuronic acid (907 $cm^{-1}$) found in the cell wall of Gram-positive that characterize each of the *S. aureus* mutants (Fig. 5A). Region 2 (1431-1464 $cm^{-1}$) shows 100% discrimination with boundaries based on the QDA model that successfully separate non-pigmented strains (Δ*crtM* and Δ*ispA*), methicillin-sensitive (Δ*fmtA* and Δ*mecA*) and Δ*SAUSA300-0918* strains, and WT JE2 compared to each other (Figure 4.6C-D). For region 2, PC1 and PC2 explained 97.90% and 1.07% of the variance, respectively. This spectral region was dominated by $CH_2/CH_3$ bending (1456 $cm^{-1}$) (Figure 4.6C).

Region 3 (1495-1544 $cm^{-1}$) of interest for the *S. aureus* mutants presents boundaries based on the QDA model that present 100% discrimination of non-pigmented strains (Δ*crtM* and Δ*ispA*) compared to the rest of the *S. aureus* mutants investigated (Figure 4.6E-F). Within this spectral region of interest, PC1 and PC2 explained 99.90% and 0.03% of the variance in the data, respectively. The high percentage of variance explained by PC1 is related to the dominating Raman peak known to be due to the tentatively assigned carotenoid staphyloxanthin (1523 $cm^{-1}$) (Figure 4.6E). Similar biochemical features resembling carotenoids have also been detected in *Mycoplasma pneumoniae* and were used for strain identification using Raman spectroscopy.[51] The findings motivated us to compare spectral features of methicillin-resistant to methicillin-sensitive *S. aureus*.

Initially, WT JE2, a methicillin-resistant isolate of *S. aureus* was compared to Newman, a methicillin-sensitive *S. aureus* strain. From the Raman spectra of these strains, two distinguishing peaks can be observed at 1159 $cm^{-1}$ and 1523 $cm^{-1}$, both related to carotenoid features (Figure 4.7A). Another peak that presents changes in intensity includes 1456 $cm^{-1}$ ($CH_2/CH_3$ bending). Peak ratios of 1456 $cm^{-1}$ to 1004 $cm^{-1}$ are significantly ($p<0.0001$) lower for WT JE2 when compared to Newman (Figure 4.7B). In addition, a peak ratio of 1523 $cm^{-1}$ to 1004 $cm^{-1}$ shows that WT JE2 is significantly ($p<0.0001$) greater when compared to Newman (Figure 4.7C). This was similarly observed with the carotenoid peak at 1159 $cm^{-1}$. A decrease in pigmentation production is a characteristic phenotypical feature seen in SCVs[52], which is confirmed by the comparison of the carotenoid peak ratio

between WT JE2 and Newman. In addition, the amide III-bending (C-N) at 1290 $cm^{-1}$ is significantly greater in intensity for WT JE2 compared to Newman. Furthermore, spectral intensity differences were seen in the previously described carotenoid peaks (1159 $cm^{-1}$ and 1523 $cm^{-1}$) and $CH_2/CH_3$ bending peak (1456 $cm^{-1}$) when *S. aureus* mutants Δ*fmtA* and Δ*mecA* were compared to WT JE2 and Newman. These spectral bands potentially indicate lower carotenoid concentration and higher lipid (triacylglycerol) concentration for Newman compared to WT JE2, Δ*fmtA*, and Δ*mecA*. These differences in the Raman spectra provided insight into biochemical factors that could be used to differentiate methicillin-sensitive from methicillin-resistant *S. aureus* strains.

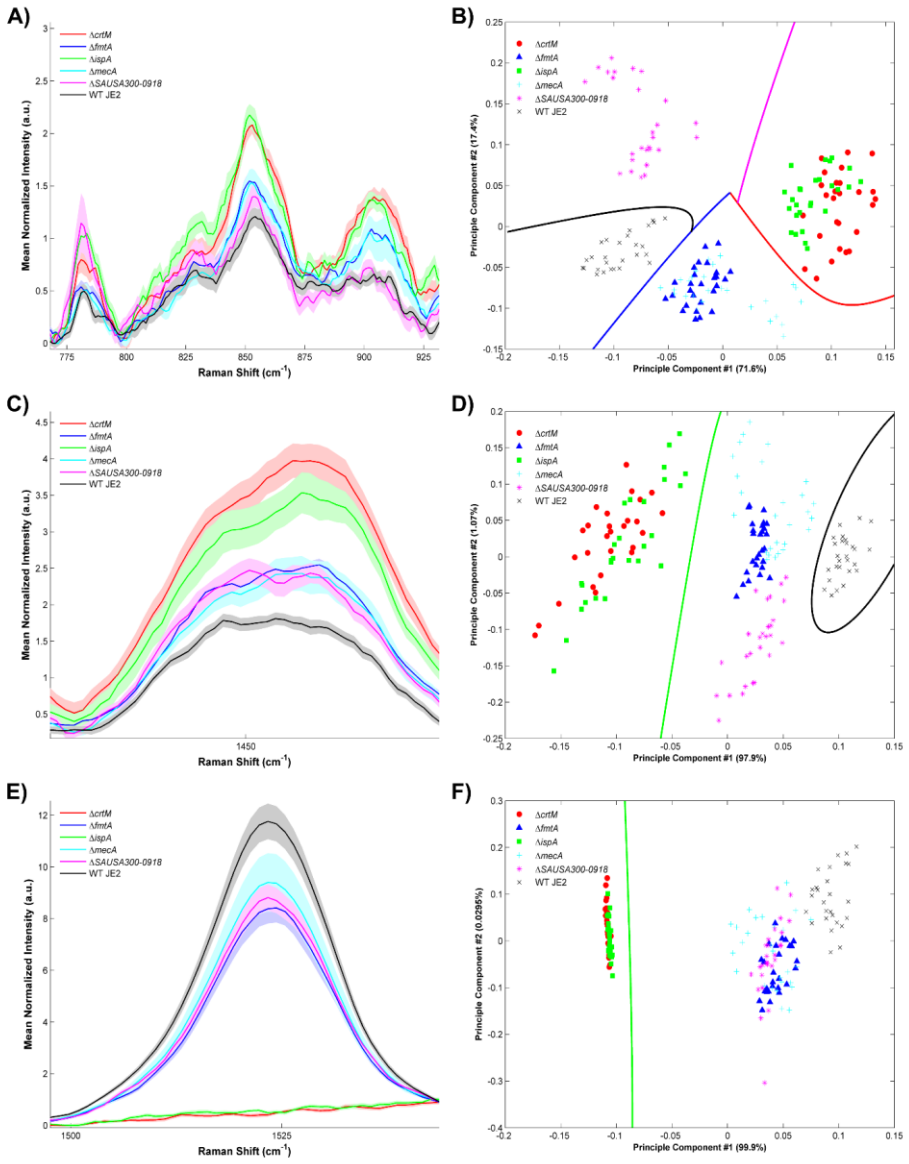


Figure 4.6: Spectral regions of interest and subsequent discriminant analysis for S. aureus mutants and WT JE2. A) Spectral region 1 (765-934 $cm^{-1}$). B) Quadratic discriminant analysis (QDA) performed on the PCA scores for spectral region 1 of S. aureus mutants and WT JE2. C) Spectral region 2 (1431-1464 $cm^{-1}$). D) QDA performed on the PCA scores for spectral region 2 of S. aureus mutants and WT JE2. E) Spectral region 3 (1495-1544 $cm^{-1}$). F) QDA performed on the PCA scores for spectral region 3 of S. aureus mutants and WT JE2.

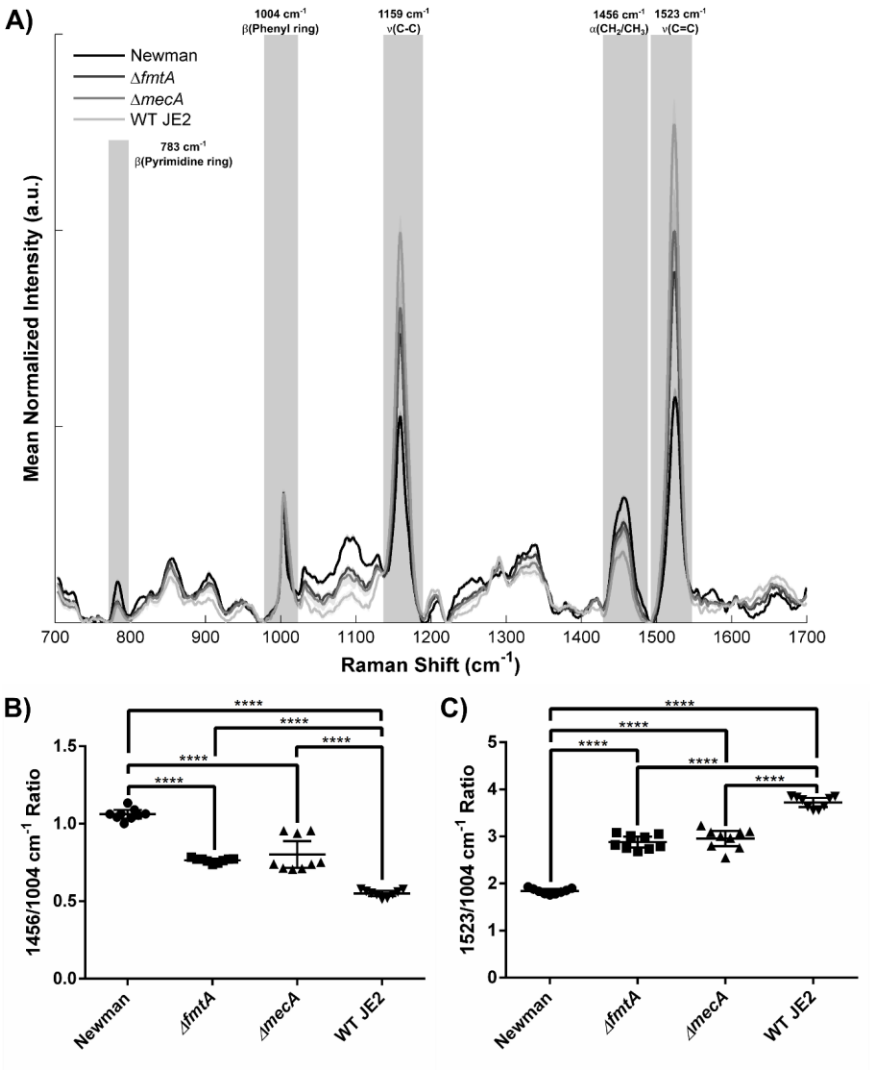


Figure 4.7**:** Comparison of *S. aureus* methicillin-sensitive, methicillin-resistant strains, and mutants. (A) Mean ± standard deviation Raman spectra of Newman (wild-type methicillin-sensitive), ΔfmtA, ΔmecA, and WT JE2 (wild-type methicillin-resistant). (B) Mean peak ratio of 1456 $cm^{-1}$ α($CH_2$/$CH_3$) to 1004 $cm^{-1}$ β(phenyl ring) with 95% confidence interval calculated using a one-way ANOVA performed to compare mutants vs. WT JE2 and Newman. (C) Mean peak ratio of 1523 $cm^{-1}$ ν(C=C) and 1004 $cm^{-1}$ β(phenyl ring) with 95% confidence interval calculated using a one-way ANOVA performed to compare mutants vs. WT JE2 and Newman. ****=p<0.0001. α, bending; β, breathing; ν, stretching.

4.4.4 Small-colony Variants (SCVs) can be Distinguished from WT Newman Strain.

Since results strongly indicate that Raman microspectroscopy can distinguish biochemical signatures of methicillin resistance or sensitivity in *S. aureus*, other types of antibiotic tolerance were investigated. Analysis was extended to the clinically relevant small-colony variant (SCV) phenotype, which is intrinsically-resistant to aminoglycoside antibiotics. The SCV phenotype conveyed by three different types of mutations was compared to their parental strain, the methicillin-sensitive strain Newman.[53] The SCV mutations chosen for this analysis were a double cytochrome deletion Δ*cyd* Δ*qox*, as well as the more clinically-relevant variants lacking heme (Δ*hemB*) or menaquinone (Δ*menB*) biosynthesis.

Raman spectra of SCVs with regions showing spectral differences are highlighted by gray bands and quantified using peak ratios (Figure 4.8A). The first peak ratio of 781 $cm^{-1}$ to 1004 $cm^{-1}$ (pyrimidine ring breathing as part of deoxyribonucleic acid (DNA)/phenylalanine) was significantly lower ($p<0.0001$) for Newman when compared to the other SCVs (Figure 4.8B). Another peak ratio of interest was the 1524 $cm^{-1}$ to 1004 $cm^{-1}$ (assigned as carotenoid/phenylalanine), which shows Newman at a significantly higher Raman intensity ($p<0.0001$) compared to the other three SCVs (Figure 4.8C). The lower Raman intensity at 1524 $cm^{-1}$ for the SCVs was expected since they are defective in their pigment production[8] compared to Newman.

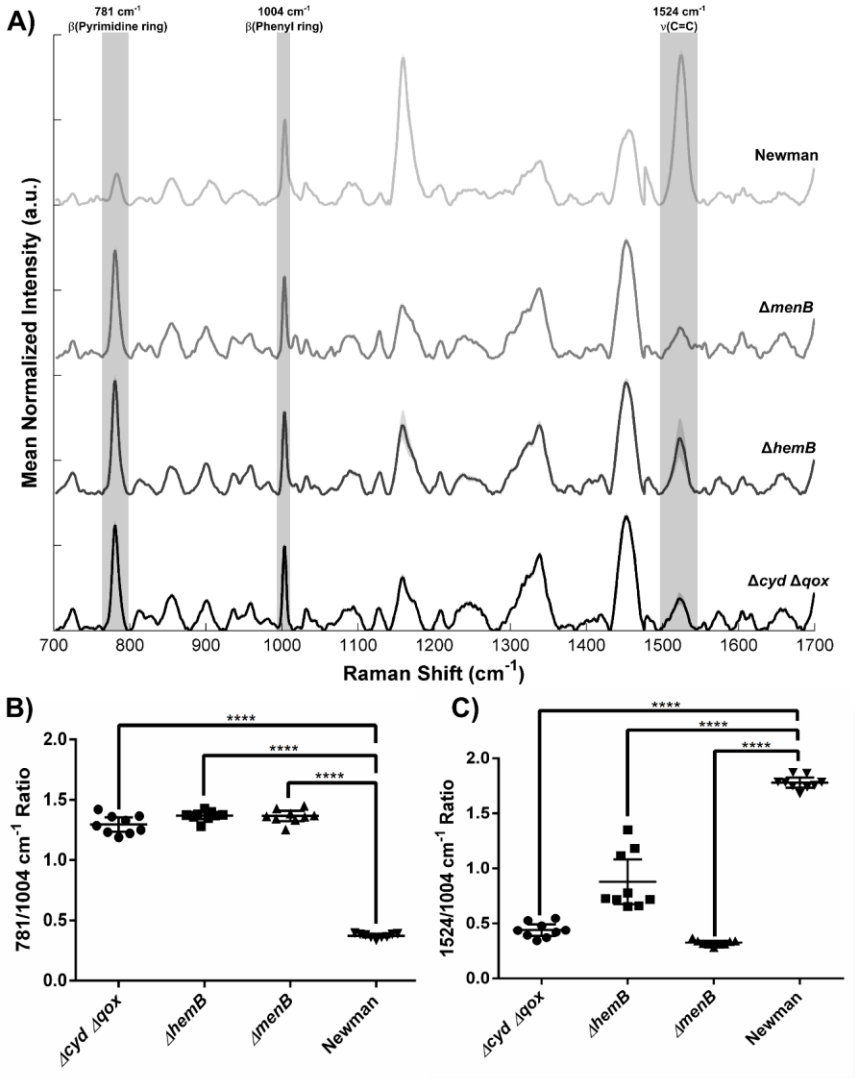


Figure 4.8: Comparison of SCVs based on DNA and pigmentation features. (A) Mean ± standard deviation Raman spectra of Newman and SCVs. (B) Mean peak ratio of 781 $cm^{-1}$ β(pyrimidine ring) and 1004 $cm^{-1}$ β(phenyl ring) with 95% confidence interval calculated using a one-way ANOVA performed to compare mutants vs. Newman. (C) Mean peak ratio of 1524 $cm^{-1}$ ν(C=C) and 1004 $cm^{-1}$ β(phenyl ring) with 95% confidence interval calculated using a one-way ANOVA performed to compare mutants vs. Newman. ****=p<0.0001. β, breathing; ν, stretching.

Evaluation of SCVs using their full-spectrum for PCA shows variation based on PC1 (93.3%) and PC2 (2.21%) between Newman, Δ*cyd* Δ*qox,* Δ*hemB*, and Δ*menB* (data not shown). Following the same approach as the *S. aureus* mutants, the magnitudes of the correlation coefficients from PC1 and PC2 of the SCVs were used to identify spectral regions for subsequent analysis. The highest PC1 correlation coefficient is located at 1524 $cm^{-1}$ and the second highest is at 1159 $cm^{-1}$ (Figure 4.9A). These are the same Raman peaks that were identified from the *S. aureus* mutant data. Since both of these features are characteristic of carotenoids, only the highest PC1 feature (1524 $cm^{-1}$) was included as part of the analysis. The next spectral region of interest for analysis was defined by the third highest PC1 feature at 781 $cm^{-1}$, which was also present in PC2 as the highest correlation coefficient for the SCV data. Since the feature with the second highest PC2 correlation coefficient (1522 $cm^{-1}$, Figure 4.9A) was previously selected from PC1, the third highest PC2 feature located at 1019 $cm^{-1}$ was used for spectral region analysis. The spectral SCV regions identified for analysis are 772-800 $cm^{-1}$ (region 1), 1012-1029 $cm^{-1}$ (region 2), and 1500-1558 $cm^{-1}$ (region 3) (Figure 4.9B).

A QDA analysis using PCA-SVD of each of the spectral regions of interest was again implemented to discriminate amongst SCVs. For region 1 (772-800 $cm^{-1}$) of the SCV data the QDA boundaries provided 100% classification of Newman from the rest of the SCVs (Figure 4.10A-B). Within spectral region 1, PC1 and PC2 explained 99.20% and 0.35% of the variance in the data, respectively. This was mainly dependent on the Raman peak that dominates this spectral region located at ~781 $cm^{-1}$ (assigned as pyrimidine ring breath as part of DNA), which was

significantly lower in Newman compared to the other SCVs (Figure 4.10A). Region 2 (1012-1029 $cm^{-1}$) was able to classify (100%) between each SCV strain based on QDA based on PC1 (80.80%) and PC2 (16.60%) (Figure 4.10C-D). The main band highlighted within this spectral region (~1015-1017 $cm^{-1}$) may be assigned to tryptophan (amino acid) and C-O stretch as part of the DNA backbone (Figure 4.10C). Similar to region 2, region 3 (1500-1558 $cm^{-1}$) of the SCVs presents 100% discrimination between each SCV strain using PC1 (99.00%) and PC2 (0.60%) (Figure 4.10F). The main biochemical features within this spectral region include 1524 $cm^{-1}$ (C=C stretching as part of a carotenoid molecule) and 1555 $cm^{-1}$ (assigned as the indole ring of tryptophan) (Figure 4.10E). These findings indicate that not only can Raman microspectroscopy be used to identify the presence of these SCVs, but also may be applied to identify other SCVs and categorize their type without the need for time-consuming detection methods.

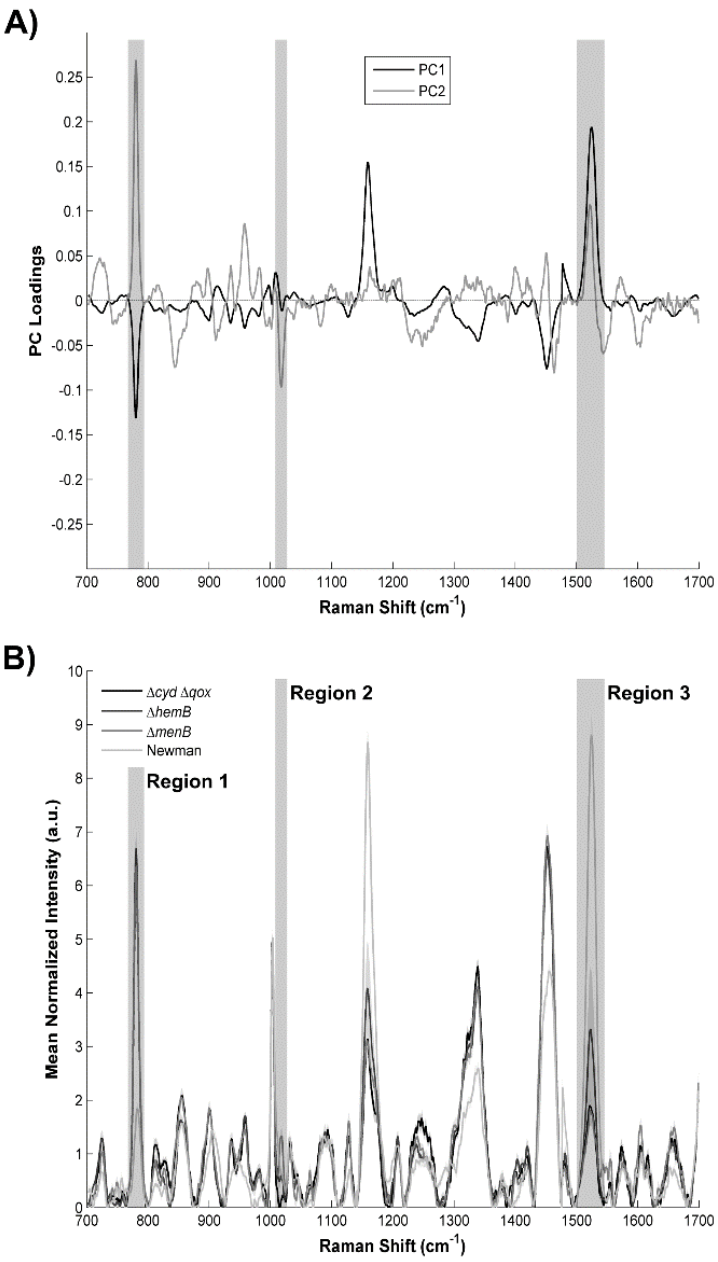


Figure 4.9: Spectral region analysis of SCVs based on PC correlation coefficients. (A) Gray bands identify spectral regions for analysis of Newman and SCVs as determined by PC correlation coefficients. (B) Spectral regions, indicated by gray bands, used for discriminant analysis of SCVs and Newman.

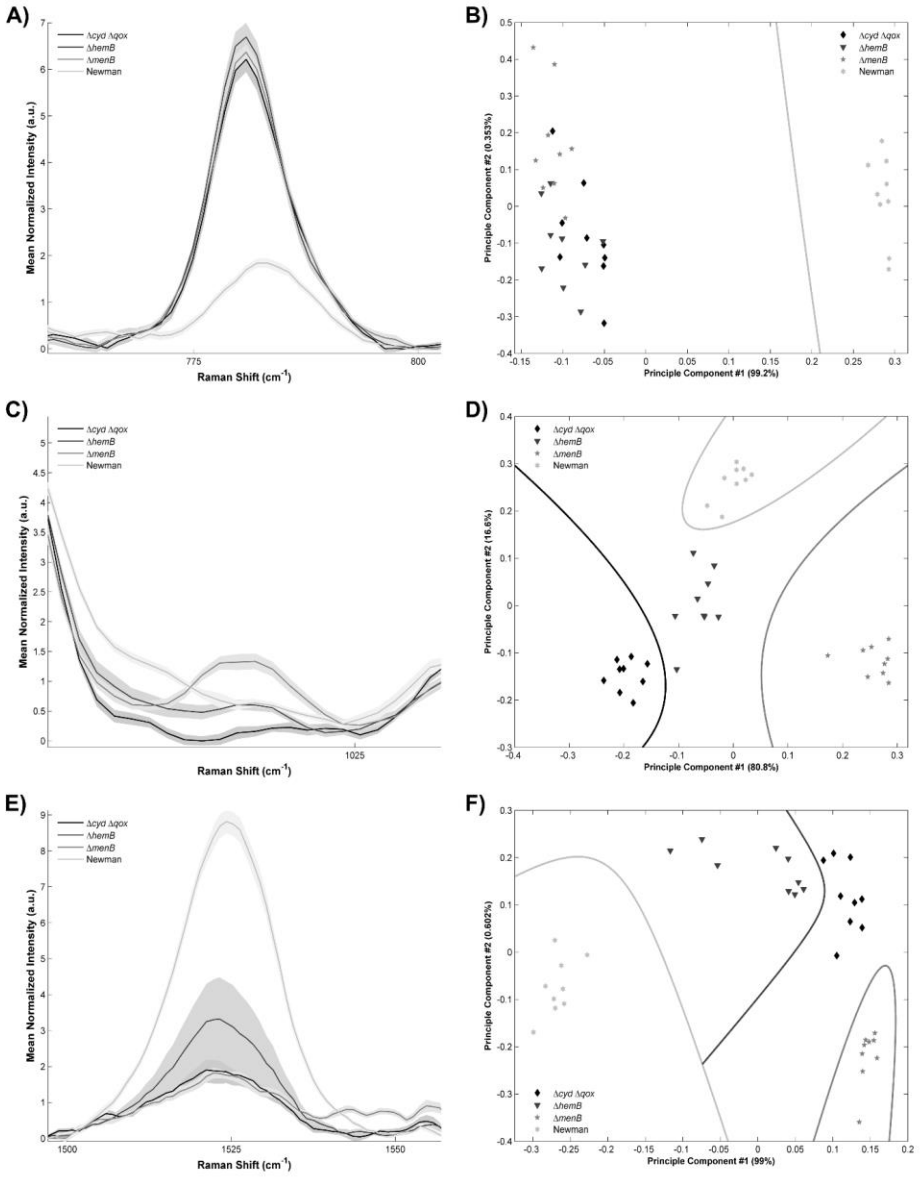


Figure 4.10: Spectral regions of interest and subsequent discriminant analysis for SCVs and Newman. (A) Spectral region 1 (772-800 $cm^{-1}$). (B) Quadratic discriminant analysis (QDA) performed on the PCA scores for spectral region 1 of SCVs and Newman. (C) Spectral region 2 (1012-1029 $cm^{-1}$). (D) QDA performed on the PCA scores for spectral region 2 of SCVs and Newman. (E) Spectral region 3 (1500-1558 $cm^{-1}$). (F) QDA performed on the PCA scores for spectral region 3 of SCVs and Newman.

The growth of antibiotic-resistant pathogens has motivated the creation of new antibiotics and diagnostic tests to track their development. Although molecular-based detection methods have been used extensively, novel approaches are needed that will provide rapid measurements, accurate results, and precise discrimination to identify antibiotic-resistant bacteria in various environments, aiding physicians to provide proper antibiotic treatment. Results using Raman microspectroscopy and QDA of PCA scores provided 100% accuracy in classifying *S. aureus* genetic variants and SCVs *in situ* based on the QDA boundaries. More specifically, antibiotic susceptibility and resistance based on biochemical differences could be distinguished from WT strains. Although WT JE2 and Δ*SAUSA300-0918* were distinguished from each other and from the other mutants, methicillin-sensitive strains (Δ*fmtA* and Δ*mecA*) were not discriminated from each other and neither were the non-pigmented strains (Δ*crtM* and Δ*ispA*). For the SCVs that were studied, each of the genetic variant strains and Newman could be distinguished from each other by utilizing two of the regions that were statistically designated (Figure 4.10C-F). Successful classification for each of the SCVs may be due to the highly varied modes of action to achieve the reduction of proton motive force in these strains. The proton motive force in Δ*cyd* Δ*qox* is reduced due to the absence of highly abundant membrane proteins; Δ*hemB* is impacted by the absence of a heme cofactor that is not only used in cytochromes, but also found in proteins such as catalase and therefore potentially impacting multiple cellular processes; and Δ*menB* lacks the lipophilic vitamin menaquinone. These diverse biochemical changes in Newman mutants, compared to JE2

isogenic variants, may be the reason why classification was more robust in Newman strains. These pathogens were successfully discriminated based on changes in their biochemical synthesis pathways, which Raman spectroscopy was able to detect directly from bacterial colonies.

In addition to bacterial detection and identification, efficacy of antibiotic treatment is critical to improving patient care. Although bacterial strains for this study were cultured for 24 hours to determine the robustness of our approach, Raman spectra have been collected from microcolonies incubated for only 6 hours[20], which would be important for detecting bacterial growth in a shorter time. Other groups have utilized Raman spectroscopy to study vancomycin-sensitive and resistant strains of *Enterococcus faecalis*[54] and *E. coli* that contained a plasmid with an ampicillin resistance gene.[55] Phenotypic profiling of the effects of antibiotic treatment on dried *E. coli* cells has also been evaluated using Raman spectroscopy, which discriminated Raman spectra based on the class of antibiotic treatment using PCA and discriminant analysis.[56] With the use of aluminum coated substrates, researchers have been able to determine levels of antibiotic susceptibility and minimum concentrations of antibiotics needed to prevent bacterial growth for methicillin-susceptible *S. aureus*, wild-type *E. coli*, and clinical isolates.[54] While this study evaluated antibiotic susceptibility/resistance based on biochemical differences only across a small set of strains (Figure 7A-C), findings from this work motivate the use of Raman spectroscopy as a diagnostic tool able to detect, identify, and discriminate clinically relevant, drug-resistant pathogens *in situ* at the species level. Future studies will evaluate additional strains with diverse

genetic variants that incorporate more subtle, non-phenotypic changes that can further inform the evolution of drug resistance across other bacteria while highlighting the potential of Raman spectroscopy. While the current limitations of Raman spectroscopy and our statistical analysis approach are challenging to quantify given the low number of reported studies on this topic, they may be based on the biochemical impact of a given genetic mutation or multiple mutations and the spectral resolution of a given Raman spectroscopy system.

In conclusion, biochemical features important for identification of drug-resistant *S. aureus* strains were identified using Raman microspectroscopy in combination with spectral regions for analysis. Raman measurements were made directly on the bacterial colonies in the agar and did not require additional preparation steps after incubation. Although visual evaluation of the *S. aureus* genetic variants' Raman spectra presented qualitative differences based on the presence or absence of carotenoid features (1159 $cm^{-1}$ and 1523 $cm^{-1}$) between two non-pigmented mutants and the rest, a statistical analysis approach is needed to discriminate other bacteria not represented by these Raman peaks. Plotting PCA correlation coefficients across the entire Raman spectrum for *S. aureus* mutants and SCVs highlights biochemical regions of interest used for subsequent QDA classification and minimizes data overfitting. Furthermore, the implementation of this classification system becomes invaluable in streamlining clinical decisions, removing the complexity of the initial spectral analysis. This approach may enhance the adoption of Raman spectroscopy as a point of care diagnostic device, especially when implemented in a handheld or portable setup.

This statistical approach of evaluating spectral regions relevant to the sample of interest may be important for identifying pathogens in environments that have a high Raman scattering background seen in the typical biological fingerprint window (700-1800 $cm^{-1}$).

To fully utilize this classification approach, a spectral library of *S. aureus* genetic variants and other strains will need to be developed that incorporates various biochemical features across spectral regions for discrimination. The size of the spectral library needed to have practical significance will depend highly on the function and setting of the application (e.g. research vs. clinical). For example, researchers in a lab setting may be focused on evaluating strains of a small set of bacteria from a specific genus and species. Therefore, the spectral library for their case may only require the reference Raman spectra from this subset of bacteria. However, if utilized in a clinical setting, the spectral database will need to be comprehensive and include bacteria from different genus and species, especially those that are most clinically important (e.g. drug-resistant strains). Since this becomes exponentially challenging to include every single bacterial strain in this database, the bacterial identification algorithm will need to be capable of pulling out “unknown” measurements for further evaluation. Extraction of “unknown” or unrecognized spectra will be important for minimizing misclassification of spectra and recognizing the need to identify the bacterial strain behind the Raman measurement. A diverse spectral database appropriate for the respective bacterial detection/identification application will enable the scientific community to fully utilize the rich biochemical data Raman spectroscopy provides while identifying

biomarkers important for classification. Furthermore, this technique and statistical analysis approach has the potential to play a major role in identifying multi-drug resistant pathogens to guide care providers with accurate information for proper and timely treatment.

## 4.5 Acknowledgements

The authors thank Shannon Manning, Ph.D., M.P.H. (Michigan State University) for generously providing strain GBS 37 and Ryan S. Doster, M.D. for information regarding the virulence of GBS strains. This work was funded by the Government under the Department of Defense, Air Force of Scientific Research, National Defense Science and Engineering Graduate (NDSEG) Fellowship, 32 CFR 168a (to O.D.A.), National Institutes of Health under Ruth L. Kirschstein National Research Service Award CA168238 (to I.J.P.), and Orrin H. Ingram endowment (to A.M-J.). Additional support was provided by the National Institutes of Health Grants R01 AI069233 and R01 AI073843 (to E.P.S.).

4.6 References


1. R. D. Scott II, “The direct medical costs of healthcare-associated infections in U.S. hospitals and the benefits of prevention,” 2009.

2. S. S. Magill *et al.*, “Multistate Point-Prevalence Survey of Health Care–Associated Infections,” *N. Engl. J. Med.*, vol. 370, no. 13, pp. 1198–1208, 2014.

3. L. L. Leape *et al.*, “The nature of adverse events in hospitalized patients: Results of the Harvard Medical Practice Study II,” vol. 324, no. 6, pp. 377–384, 1991.

4. G. A. Noskin *et al.*, “The burden of Staphylococcus aureus infections on hospitals in the United States,” vol. 165, pp. 1756–1761, 2005.

5. M. Sangappa and P. Thiagarajan, “Methicillin Resistant Staphylococcus Aureus: Resistance Genes and Their Regulation,” *Int. J. Pharm. Pharm. Sci.*, vol. 4, pp. 658–667, 2012.

6. J. Fishovitz, J. A. Hermoso, M. Chang, and S. Mobashery, “Penicillin-binding protein 2a of methicillin-resistant Staphylococcus aureus,” *IUBMB Life*, vol. 66, no. 8, pp. 572–577, 2014.

7. E. Klein, D. L. Smith, and R. Laxminarayan, “Hospitalizations and deaths caused by methicillin-resistant Staphylococcus aureus , United States, 1999-2005,” vol. 13, no. 12, pp. 1840–1846, 2007.

8. O. Melter and B. Radojevič, “Small Colony Variants of Staphylococcus aureus - review,” *Folia Microbiol. (Praha).*, vol. 55, no. 6, pp. 548–558, 2010.

9. F. Kipp *et al.*, “Evaluation of Two Chromogenic Agar Media for Recovery and Identification of Staphylococcus aureus Small-Colony Variants,” *J. Clin. Microbiol.*, vol. 43, no. 4, pp. 1956–1959, 2005.

10. M. R. Precit, D. J. Wolter, A. Griffith, J. Emerson, J. L. Burns, and L. R. Hoffman, “Optimized In Vitro Antibiotic Susceptibility Testing Method for Small-Colony Variant Staphylococcus aureus,” *Antimicrob. Agents Chemother.*, vol. 60, no. 3, pp. 1725–1735, 2016.

11. I. S. Douglas *et al.*, “Rapid automated microscopy for microbiological surveillance of ventilator-associated pneumonia,” *Am. J. Respir. Crit. Care Med.*, vol. 191, no. 5, pp. 566–573, 2015.

12. C. S. Price, S. E. Kon, and S. Metzger, “Rapid antibiotic susceptibility

phenotypic characterization of Staphylococcus aureus using automated microscopy of small numbers of cells," *J. Microbiol. Methods*, vol. 98, pp. 50–58, 2014.

13. P. W. Groundwater *et al.*, "Methods for the detection and identification of pathogenic bacteria: past, present, and future," *Chem. Soc. Rev.*, vol. 46, no. 16, pp. 4818–4832, 2017.

14. P. Kralik and M. Ricchi, "A Basic Guide to Real Time PCR in Microbial Diagnostics : Definitions , Parameters , and Everything," *Front. Microbiol.*, vol. 8, no. 108, pp. 1–9, 2017.

15. M. J. Sorrell, J. Tribble, L. Reinisch, J. A. Werkhaven, and R. H. Ossoff, "Bacteria identification of otitis media with fluorescence spectroscopy," *Lasers Surg. Med.*, vol. 14, no. 2, pp. 155–163, 1994.

16. L. R. Dartnell, T. A. Roberts, G. Moore, J. M. Ward, and J. P. Muller, "Fluorescence Characterization of Clinically-Important Bacteria," *PLoS One*, vol. 8, no. 9, pp. 1–13, 2013.

17. A. Clauditz, A. Resch, K.-P. Wieland, A. Peschel, and F. Götz, "Staphyloxanthin plays a role in the fitness of Staphylococcus aureus and its ability to cope with oxidative stress," *Infect. Immun.*, vol. 74, no. 8, pp. 4950–4953, 2006.

18. W. E. Huang, R. I. Griffiths, I. P. Thompson, M. J. Bailey, and A. S. Whiteley, "Raman microscopic analysis of single microbial cells," *Anal. Chem.*, vol. 76, no. 15, pp. 4452–4458, 2004.

19. K. Maquelin *et al.*, "Prospective study of the performance of vibrational spectroscopies for rapid identification of bacterial and fungal pathogens recovered from blood cultures.," *J. Clin. Microbiol.*, vol. 41, no. 1, pp. 324–9, 2003.

20. K. Maquelin, T. Van Vreeswijk, H. Endtz, and B. Smith, "Raman spectroscopic method for identification of clinically relevant …," *Anal. Chem*, vol. 72, no. 1, pp. 12–19, 2000.

21. S. Pahlow, S. Meisel, D. Cialla-May, K. Weber, P. Rösch, and J. Popp, "Isolation and identification of bacteria by means of Raman spectroscopy," *Adv. Drug Deliv. Rev.*, vol. 89, pp. 105–120, 2015.

22. C. Sandt, T. Smith-Palmer, J. Pink, L. Brennan, and D. Pink, "Confocal Raman microspectroscopy as a tool for studying the chemical heterogeneities of biofilms in situ," *J. Appl. Microbiol.*, vol. 103, no. 5, pp.

1808–1820, 2007.

23. M. Harz, P. Rosch, and J. Popp, “Vibrational Spectroscopy - A Powerful Tool for the Rapid Identification of Microbial Cells at the Single-Cell Level,” *J. Int. Soc. Adv. Cytom.*, vol. 75A, no. 1, pp. 104–113, 2009.

24. K. C. Schuster, E. Urlaub, and J. R. Gapes, “Single-cell analysis of bacteria by Raman microscopy: Spectral information on the chemical composition of cells and on the heterogeneity in a culture,” *J. Microbiol. Methods*, vol. 42, no. 1, pp. 29–38, 2000.

25. K. C. Schuster, I. Reese, E. Urlaub, J. R. Gapes, and B. Lendl, “Multidimensional Information on the Chemical Composition of Single Bacterial Cells by Confocal Raman Microspectroscopy,” *Anal. Chem.*, vol. 72, no. 22, pp. 5529–5534, 2000.

26. U. Neugebauer *et al.*, “The Influence of Fluoroquinolone Drugs on the Bacterial Growth of S . epidermidis Utilizing the Unique Potential of Vibrational Spectroscopy,” *J. Phys. Chem.*, vol. 111, no. 15, pp. 2898–2906, 2007.

27. M. Harz, P. Rösch, K.-D. Peschke, O. Ronneberger, H. Burkhardt, and J. Popp, “Micro-Raman spectroscopic identification of bacterial cells of the genus Staphylococcus and dependence on their cultivation conditions,” *Analyst*, vol. 130, no. 11, pp. 1543–1550, 2005.

28. S. Meisel, S. Stöckel, M. Elschner, F. Melzer, P. Rösch, and J. Popp, “Raman spectroscopy as a potential tool for detection of Brucella spp. in milk,” *Appl. Environ. Microbiol.*, vol. 78, no. 16, pp. 5575–5583, 2012.

29. C. L. C. Wielders, A. C. Fluit, S. Brisse, J. Verhoef, and F. J. Schmitz, “mecA gene is widely disseminated in Staphylococcus aureus population,” *J. Clin. Microbiol.*, vol. 40, no. 11, pp. 3970–3975, 2002.

30. B. Ballhausen, A. Kriegeskorte, N. Schleimer, G. Peters, and K. Becker, “The mecA homolog mecC confers resistance against β-lactams in Staphylococcus aureus irrespective of the genetic strain background,” *Antimicrob. Agents Chemother.*, vol. 58, no. 7, pp. 3791–3798, 2014.

31. L. Lan, A. Cheng, P. M. Dunman, D. Missiakas, and C. He, “Golden Pigment Production and Virulence Gene Expression Are Affected by Metabolisms in Staphylococcus aureus,” *J. Bacteriol.*, vol. 192, no. 12, pp. 3068–3077, 2010.

32. A. Qamar and D. Golemi-Kotra, “Dual Roles of FmtA in Staphylococcus

aureus Cell Wall Biosynthesis and Autolysis," *Antimicrob. Agents Chemother.*, vol. 56, no. 7, pp. 3797–3805, 2012.

33. B. R. Boles, M. Thoendel, A. J. Roth, and A. R. Horswill, "Identification of Genes Involved in Polysaccharide- Independent Staphylococcus aureus Biofilm Formation," *PLoS One*, vol. 5, no. 4, 2010.

34. G. Y. Liu *et al.*, "Staphylococcus aureus golden pigment impairs neutrophil killing and promotes virulence through its antioxidant activity," *J. Exp. Med.*, vol. 202, no. 2, pp. 209–215, 2005.

35. N. D. Hammer *et al.*, "Two Heme-Dependent Terminal Oxidases Power Staphylococcus aureus Organ-Specific Colonization of the Vertebrate Host," *MBio*, vol. 4, no. 4, pp. 1–9, 2013.

36. C. Von Eiff, C. Heilmann, R. A. Proctor, C. Woltz, G. Peters, and F. Götz, "A site-directed Staphylococcus aureus hemB mutant is a small-colony variant which persists intracellularly," *J. Bacteriol.*, vol. 179, no. 15, pp. 4706–4712, 1997.

37. C. A. Wakeman *et al.*, "Menaquinone biosynthesis potentiates haem toxicity in Staphylococcus aureus," *Mol. Microbiol.*, vol. 86, no. 6, pp. 1376–1392, 2013.

38. E. Duthie and L. Lorenz, "Staphylococcal Coagulase: Mode of Action and Antigenicity," *Microbiology*, vol. 6, pp. 95–107, 1952.

39. S. L. Jacques, "How tissue optics affect dosimetry of photodynamic therapy," *J. Biomedi. Opt.*, vol. 15, no. 5, 051608, 2010.

40. A. Mahadevan-Jansen and C. A. Lieber, "Automated Method for Subtraction of Flourescence from Biological Raman Spectra," *Appl. Spectrosc.*, vol. 57, no. 11, pp. 1363–1367, 2003.

41. A. Savitzky and M. J. E. Golay, "Smoothing and Differentiation of Data by Simplified Least Squares Procedures," *Anal. Chem.*, vol. 36, no. 8, pp. 1627–1639, 1964.

42. J. Shlens, "A Tutorial on Principal Component Analysis," 2014.

43. H. J. Butler *et al.*, "Using Raman spectroscopy to characterize biological materials," *Nat. Protoc.*, vol. 11, no. 4, pp. 664–687, 2016.

44. M. Tang, L. Xia, D. Wei, S. Yan, C. Du, and H.-L. Cui, "Distinguishing Different Cancerous Human Cells by Raman Spectroscopy Based on

Discriminant Analysis Methods," *Appl. Sci.*, vol. 7, no. 900, pp. 1–9, 2017.

45. T. Ichimura, L. Chiu, K. Fujita, and H. Machiyama, "Non-label immune cell state prediction using Raman spectroscopy," *Sci. Rep.*, vol. 6, pp. 1–7, 2016.

46. F. S. de Siqueira e Oliveira, H. E. Giana, and L. Silveira, "Discrimination of selected species of pathogenic bacteria using near-infrared Raman spectroscopy and principal components analysis.," *J. Biomed. Opt.*, vol. 17, no. 10, p. 107004, 2012.

47. H. E. Schaffer, R. R. Chance, R. J. Silbey, K. Knoll, and R. R. Schrock, "Conjugation length dependence of Raman scattering in a series of linear polyenes : Implications for polyacetylene," *J. Chem. Phys.*, vol. 94, no. 6, pp. 4161–4170, 1991.

48. M. Rosa-Fraile, J. Rodriguez-Granger, A. Haidour-Benamin, J. M. Cuerva, and A. Sampedro, "Granadaene : Proposed Structure of the Group B Streptococcus Polyenic Pigment," *Appl. Environ. Microbiol.*, vol. 72, no. 9, pp. 6367–6370, 2006.

49. O. Ayala *et al.*, "Characterization of bacteria causing acute otitis media using Raman microspectroscopy," *Anal. Methods*, vol. 9, pp. 1864–1871, 2017.

50. K. Czamara, K. Majzner, M. Z. Pacia, K. Kochan, A. Kaczor, and M. Baranska, "Raman spectroscopy of lipids : a review," *J. Raman Spectrosc.*, vol. 46, pp. 4–20, 2014.

51. K. Maquelin *et al.*, "Raman spectroscopic typing reveals the presence of carotenoids in Mycoplasma pneumoniae," *Microbiology*, vol. 155, no. 6, pp. 2068–2077, 2009.

52. R. Procter, A. Kriegeskorte, B. Kahl, K. Becker, B. Loffler, and G. Peters, "Staphylococcus aureus Small Colony Variants (SCVs ): a road map for the metabolic pathways involved in persistent infections," *Front. Cell. Infect. Microbiol.*, vol. 4, no. 99, pp. 1–8, 2014.

53. E. Duthie and L. Lorenz, "Staphylococcal Coagulase: Mode of Action and Antigenicity," *Microbiology*, vol. 6, pp. 95–107, 1952.

54. C.-Y. Liu *et al.*, "Rapid bacterial antibiotic susceptibility test based on simple surface-enhanced Raman spectroscopic biomarkers," *Sci. Rep.*, vol. 6, pp. 1–15, 2016.

55. A. Walter *et al.*, “Raman spectroscopic detection of physiology changes in plasmid-bearing *Escherichia coli* with and without antibiotic treatment,” *Anal. Bioanal. Chem.*, vol. 400, no. 9, pp. 2763–2773, 2011.

56. A. I. M. Athamneh, R. A. Alajlouni, R. S. Wallace, M. N. Seleem, and R. S. Senger, “Phenotypic Profiling of Antibiotic Response Signatures in Escherichia coli Using Raman Spectroscopy,” *Antimicrob. Agents Chemother.*, vol. 58, no. 3, pp. 1302–1314, 2014.

# CHAPTER 5

## 5. RAMAN MICROSPECTROSCOPY DIFFERENTIATES PERINATAL PATHOGENS ON *EX VIVO* INFECTED HUMAN FETAL MEMBRANE TISSUES

### 5.1 Abstract

*Streptococcus agalactiae*, also known as Group B *Streptococcus* (GBS), is a major cause of chorioamnionitis and neonatal sepsis. This study evaluates Raman spectroscopy (RS) to identify spectral characteristics of infection and differentiate GBS from *Escherichia coli* and *Staphylococcus aureus* during *ex vivo* infection of human fetal membrane tissues. Unique spectral features were identified from colonies grown on agar and infected fetal membrane tissues. Multinomial logistic regression analysis accurately identified GBS infected tissues with 100.0% sensitivity and 88.9% specificity. Together, these findings support further investigation into the use of RS as an emerging microbiologic diagnostic tool and intrapartum screening test for GBS carriage.

### 5.2 Introduction

*Streptococcus agalactiae*, also known as Group B *Streptococcus* (GBS), colonizes 10-40% of women during pregnancy, and GBS vaginal colonization is an important risk factor for chorioamnionitis, or infection of the fetal membranes, and neonatal sepsis.[1] The Centers for Disease Control and Prevention recommends culture-based rectovaginal GBS screening during the third trimester

followed by intrapartum antibiotic prophylaxis for women testing positive.[2] Although this strategy has reduced the incidence of early-onset sepsis by 80%, 15% of full-term and 50% of preterm births do not receive screening prior to delivery.[3] Additionally, prior studies of women delivering neonates with early-onset GBS sepsis found that 75-82% were screened, but tested negative[4,5], indicating the need for a more sensitive method. Traditional culture-based screening requires 24-72 hours to provide results; PCR testing could reduce this time to a few hours, but this technology is not available in all settings.[6] A rapid GBS diagnostic test could provide opportunities to identify GBS colonized women at the time of labor and focus the use of antibiotic therapy.

Raman spectroscopy (RS) is an inelastic light scattering technique that provides a biochemical "fingerprint" with sensitivity to features such as nucleic acids, carbohydrates, lipids, and proteins. Raman microspectroscopy (RμS), which provides higher spectral resolution, has been used to characterize bacteria and provide discrimination at the genus and species levels in vitro[7,8] and identify bacteria directly from clinical samples culture-free.[9] This technique could provide opportunities to identify GBS or other bacteria as a rapid diagnostic test, minimizing sample preparation and streamlining diagnostic information.

Due to the pressing need to accurately and rapidly determine the intrapartum GBS status of women, the ability of RμS to discriminate bacteria cultured on agar and in an *ex vivo* human tissue model of chorioamnionitis was investigated, comparing GBS with other pathogens implicated in perinatal infections and chorioamnionitis.[10] Here, we demonstrate that GBS has unique

Raman spectral features that can be observed whether RμS is used to interrogate bacterial colonies on agar or *ex vivo* infected fetal membrane tissues. Detecting characteristic GBS spectral patterns suggests that this technology might inform new lab-based or point-of-care diagnostic tests to identify GBS colonization or infection.

## 5.3 Methods

### 5.3.1 Bacterial Culture

For RμS colony measurements, diverse capsular serotype isolates of *Streptococcus agalactiae* (Table 5.1), an invasive clinical isolate of *Escherichia* coli[11], and methicillin-resistant *Staphylococcus aureus* (MRSA) strain USA300, (ATCC #BAA-1717, Manassas, VA) were cultured on Mueller-Hinton (MH) agar (BD, Franklin Lakes, NJ) to minimize signal contribution from media.

For human fetal membrane infection, three GBS strains, *E. coli*, and MRSA were cultured on tryptic soy agar supplemented with 5% sheep blood at 37ºC in ambient air overnight. Bacteria were sub-cultured from blood agar plates into Todd-Hewitt broth (BD) and incubated (shaking at 200 RPM) at 37ºC in ambient air overnight. Cells were then washed, suspended in phosphate buffered saline (pH 7.4), and bacterial density was measured spectrophotometrically at an optical density of 600 nm ($OD_{600}$).

### 5.3.2 Human Fetal Membrane Co-Culture

The Vanderbilt Institutional Review Board approved (approval 131607) isolation of de-identified human fetal membrane tissues, which was conducted as previously described.[9] Bacteria were added to the fetal membrane choriodecidual surface at a multiplicity of infection of $1x10^6$ cells per 12 mm diameter membrane, using a predetermined coefficient of bacterial density of 1 $OD_{600}$= $1x10^9$ cells. Uninfected membrane samples were also maintained. Co-cultures were incubated at 37 ºC in ambient air containing 5% $CO_2$ for 48-72 hours prior to RμS evaluation (Figure 5.1).

### 5.3.3 Raman Microspectroscopy

A Raman microscope (inVia Raman Microscope, Renishaw plc, Gloucestershire, UK) with an 830 nm laser diode was used for spectral measurements.[12] For bacterial colonies, a 100X objective (N PLAN EPI, NA=0.85, Leica, Weltzlar, Germany) was used to focus the laser at ~12 mW. Fetal membrane tissue spectra were measured using a 50X objective (N PLAN EPI, NA=0.75, Leica) to focus a 40 μm laser line on the sample at ~23 mW. Raman scattered light was detected as previously described with a spectral resolution of ~1 $cm^{-1}$.[12]

Spectral measurements for bacterial colonies included one spot per colony and three colonies per bacteria from a single culture plate using a 15-second exposure with 9 accumulations from 800-1700 $cm^{-1}$. Raman measurements from three different locations were performed on each punch biopsy tissue (total of 34).

These included control (uninfected, n=5), GB00037 (n=6), GB00590 (n=5), GB01084 (n=6), *E. coli* (n=5), and MRSA (n=7) representing at least three separate placental samples with 1-3 technical replicates (Table 5.2). Acquisition parameters for fetal membrane tissues included a 15-second exposure with 3 accumulations.

### 5.3.4 Raman Data Processing & Spectral Analysis

Spectral data processing prior to analysis including fluorescence background subtraction and noise smoothing was performed as previously described.[12] A 9$^{th}$ degree modified polynomial fit was used for spectral measurements from GBS colonies and tissue model. Post-processed, non-normalized Raman spectra were z-scored for subsequent analysis. Principal component analysis (PCA), a non-supervised data reduction statistical approach, was performed on z-scored bacterial colony spectra using singular value decomposition (SVD). The scores output from PCA-SVD were then used to calculate the distance between each data point in orthogonal vector space using the Euclidean distance measure. A hierarchical cluster analysis (HCA) was designed based on the PCA-SVD score distances calculated and an agglomerative clustering approach with single linkage.

A machine learning algorithm, sparse multinomial logistic regression (SMLR)[13], was utilized to discriminate across the different tissues.[12] Briefly, training data was compiled based on RμS measurements of the fetal membrane tissues. For this analysis, a value called SMLR feature importance (SMLR-FI), a linear

combination of importance (weight) and frequency of features, was used to determine biomarkers critical for successful classification of infected biofilm tissues.[14] A posterior probability of class membership was plotted for infected membrane tissues. Evaluation of this algorithm was performed using a *k*-fold cross validation (leave-one-tissue-out).

### 5.3.5 Scanning Electron Microscopy

Following RμS analysis, human fetal membrane samples were prepared for scanning electron microscopy as previously described.[10] Samples were imaged with a FEI Quanta 250 field-emission gun scanning electron microscope (FEG-SEM). Images are representative of three replicates from three different subjects.

Table 5.1: GBS strains used in this study.

| GBS Strain | Molecular Serotype | Multi-Locus Sequence Type | Setting of Isolation | Source |
|---|---|---|---|---|
| GB00037 | V | ST-1 | Neonatal sepsis | S. D. Manning, A. C. Springman, E. Lehotzky, M. A. Lewis, T. S. Whittam, and H. D. Davies, Journal of Clinical Microbiology **2009**, 47, 1143. |
| GB00590 | III | ST-19 | Vaginal/rectal Colonization | S. D. Manning, A. C. Springman, E. Lehotzky, M. A. Lewis, T. S. Whittam, and H. D. Davies, Clinical Infectious Diseases **2008**, 46, 1829. |
| GB00002 | Ia | ST-23 | Vaginal/rectal Colonization | S. D. Manning, A. C. Springman, E. Lehotzky, M. A. Lewis, T. S. Whittam, and H. D. Davies, Clinical Infectious Diseases **2008**, 46, 1829. |
| GB01084 (CNCTC 10/84) | V | ST-26 | Unknown | ATCC #49447<br>H. W. Wilkinson, Journal of Clinical Microbiology **1977**, 6, 183. |
| GB2603 V/R | V | Unknown | Unknown | ATCC #BAA-611<br>H. Tettelin, V. Masignani, M. J. Cieslewicz, J. A. Eisen, S. Peterson, M. R. Wessels, I. T. Paulsen, K. E. Nelson, I. Margarit, T. D. Read, L. C. Madoff, A. M. Wolf, M. J. Beanan, L. M. Brinkac, S. C. Daugherty, R. T. DeBoy, A. S. Durkin, J. F. Kolonay, R. Madupu, M. R. Lewis, D. Radune, N. B. Fedorova, D. Scanlan, H. Khouri, S. Mulligan, H. A. Carty, R. T. Cline, S. E. Van Aken, J. Gill, M. Scarselli, M. Mora, E. T. Iacobini, C. Brettoni, G. Galli, M. Mariani, F. Vegni, D. Maione, D. Rinaudo, R. Rappuoli, J. L. Telford, D. L. Kasper, G. Grandi, and C. M. Fraser, Proceedings of the National Academy of Sciences of the United States of America, **2002**, 99, 12391. |

Table 5.2: Fetal membrane tissue sample overview.

| | **Number of technical replicates per placenta sample** | | | | | |
|---|---|---|---|---|---|---|
| | Uninfected | GB00037 | GB00590 | GB01084 | MRSA | *E.coli* |
| **Placenta 1** | 3 | 3 | 3 | 3 | 0 | 0 |
| **Placenta 2** | 0 | 0 | 0 | 0 | 3 | 2 |
| **Placenta 3** | 1 | 2 | 1 | 1 | 2 | 2 |
| **Placenta 4** | 1 | 1 | 1 | 2 | 2 | 1 |

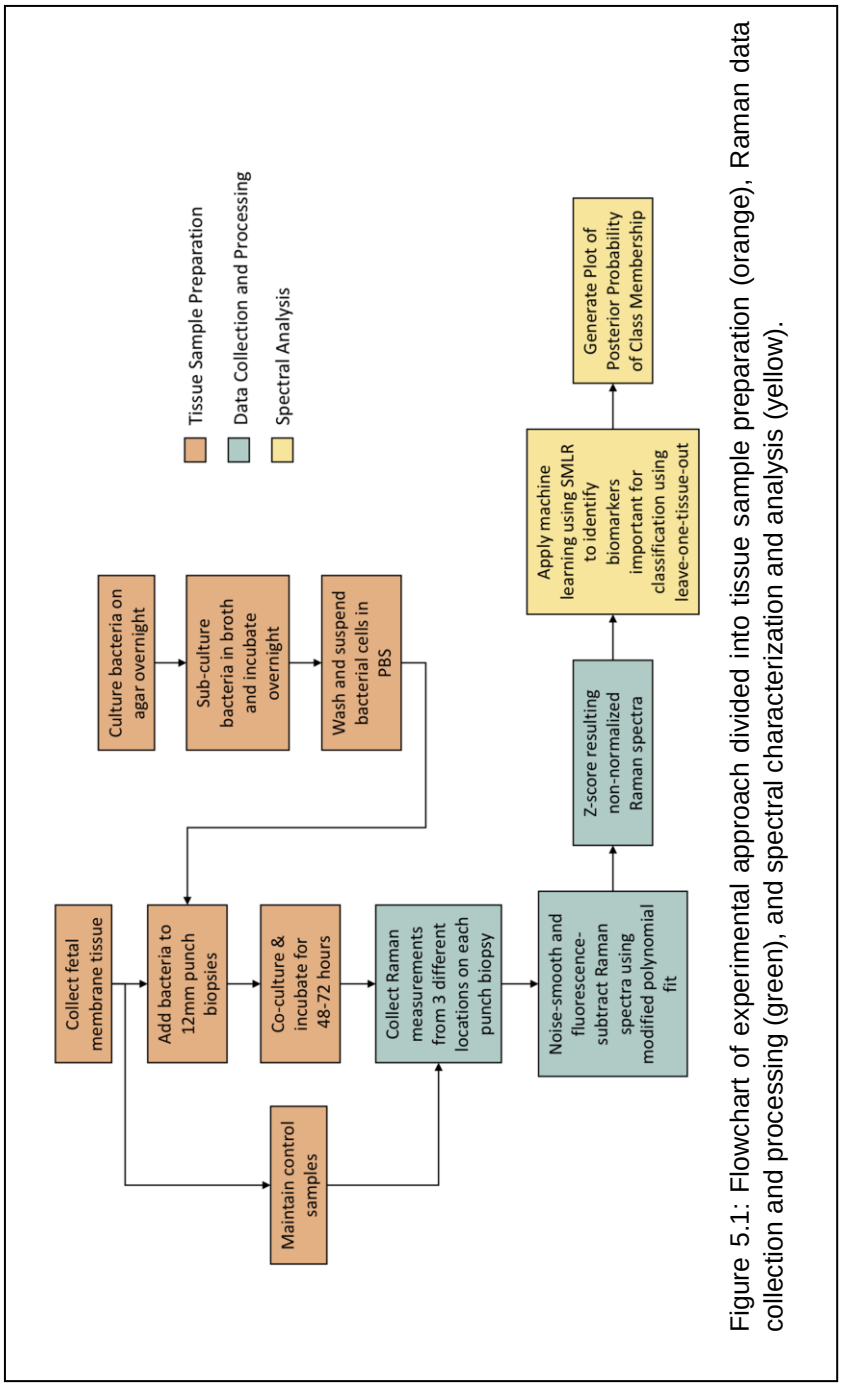


Figure 5.1: Flowchart of experimental approach divided into tissue sample preparation (orange), Raman data collection and processing (green), and spectral characterization and analysis (yellow).

## 5.4 Results

### 5.4.1 Raman Microspectroscopy (RμS) Differentiates Bacterial Species and Strains on Agar.

A diverse set of GBS strains were selected based on capsular type, multilocus sequence types (MLST), and β-hemolysin pigment production (Table 5.1). Visual differences in colony pigmentation are evident across strains (Figure 5.2A). Corresponding Raman spectra of GBS, MRSA, and *E. coli* bacterial colonies are shown in Figure 5.2B. Each of the strains presents familiar Raman peaks at 1004 $cm^{-1}$ (C-C skeletal stretching of aromatic ring related to phenylalanine), 1033 $cm^{-1}$ (C-H in plane deformation related to phenylalanine), and 1340 $cm^{-1}$ ($CH_2$ and $CH_3$ related to fatty acids and protein deformation) to name a few. Major strain biochemical variations are highlighted in the gray bands of Raman spectra. For example, GB01084 contains two Raman peaks at 1121 $cm^{-1}$ and 1506 $cm^{-1}$ that are higher in intensity compared to other GBS, *E. coli*, and MRSA strains. Similarly, MRSA contains unique Raman peaks at 1159 $cm^{-1}$ and 1525 $cm^{-1}$ that are not present in any other strain evaluated. The HCA dendrogram presents clusters of MRSA, GB01084, *E. coli*, and the remaining GBS strains studied based on the dissimilarity of the pairwise distances of observations (PCA-SVD scores from principal components 1 and 2) from their respective Raman spectra (Figure 5.2C).

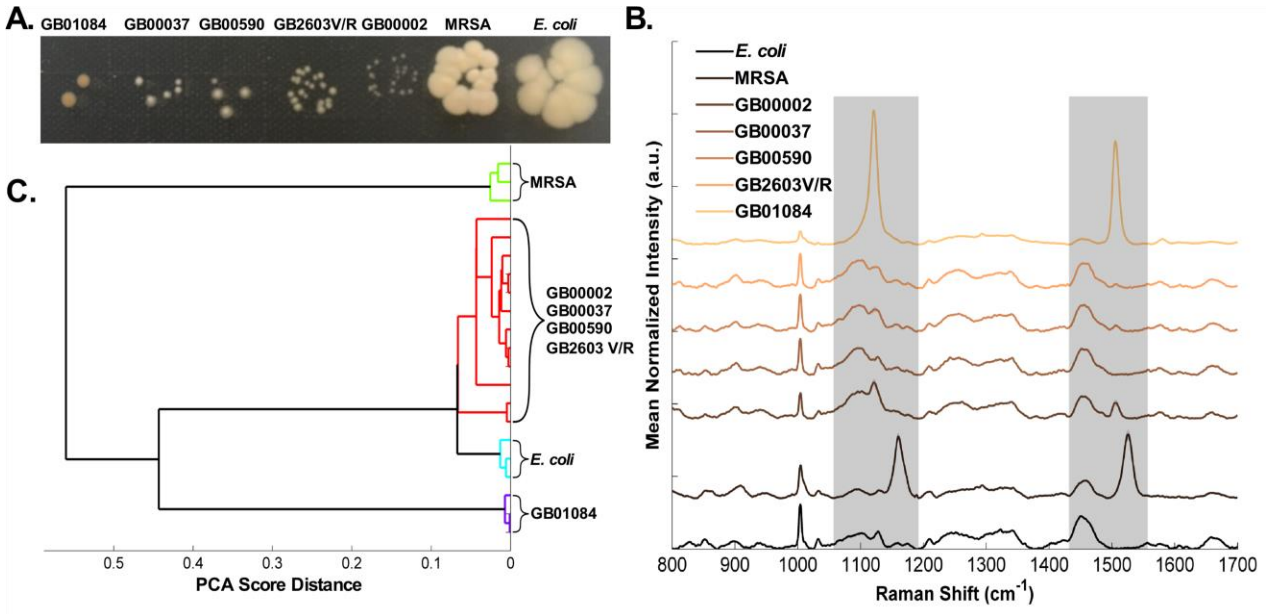


Figure 5.2: Raman spectra of GBS, MRSA, and E. coli bacterial colonies present distinct biochemical features. A: Bacterial cells from five Group B *Streptococcus* (GBS) strains, *S. aureus* strain USA300 (MRSA), and *E. coli* serotype O75:H5:K1 were grown on Mueller-Hinton (MH) agar to demonstrate pigmentation differences of the strains. B: Mean ± standard deviation Raman spectra of bacterial colonies. C: Hierarchical cluster analysis (HCA) of bacterial colony measurements based on principal component analysis scores.

5.4.2 RμS Distinguishes Bacterial Infection in Explanted Fetal Membrane Tissues.

Given similarities of the spectra collected from GBS on agar, *ex vivo* infection of human fetal membrane tissues were investigated as a biologically relevant model to determine if RμS was sensitive enough to distinguish GBS spectral features within infected tissues. As a first step, mean-normalized Raman spectra ± standard deviation (shaded color region) of uninfected and infected tissues were compared (Figure 5.3A). Vertical gray bands represent important biochemical features for classification of infected tissues based on a SMLR-FI of at least 25%. A probability of class membership plot highlights correctly classified spectral measurements compared to incorrectly classified measurements with respect to control and infected tissues (Figure 5.3B). A sensitivity of 97.7% and specificity of 66.7% for detection of infection on fetal membrane tissues was determined from the output confusion matrix (Figure 5.3C). The ability of RμS to differentiate GBS strains from *E. coli* and MRSA was further evaluated in these tissues. Mean-normalized Raman spectra of GBS, *E. coli*, and MRSA infected tissues are shown along with vertical gray bands indicating SMLR-FI features of at least 25% (Figure 5.4A). A probability of class membership plot shows correctly classified measurements compared to those incorrectly classified of GBS versus *E. coli* or MRSA (Figure 5.4B). Membrane tissues infected with GBS were detected with 100.0% sensitivity and 88.9% specificity (Figure 5.4C). Scanning electron microscopy imaging identifies bacterial cells present in biofilm structures at the area of Raman measurements (denoted by a small cut into membrane tissues

seen at low magnification) as demonstrated by the multilayered bacterial cells embedded in extracellular polymeric substances (Figure 5.4D).

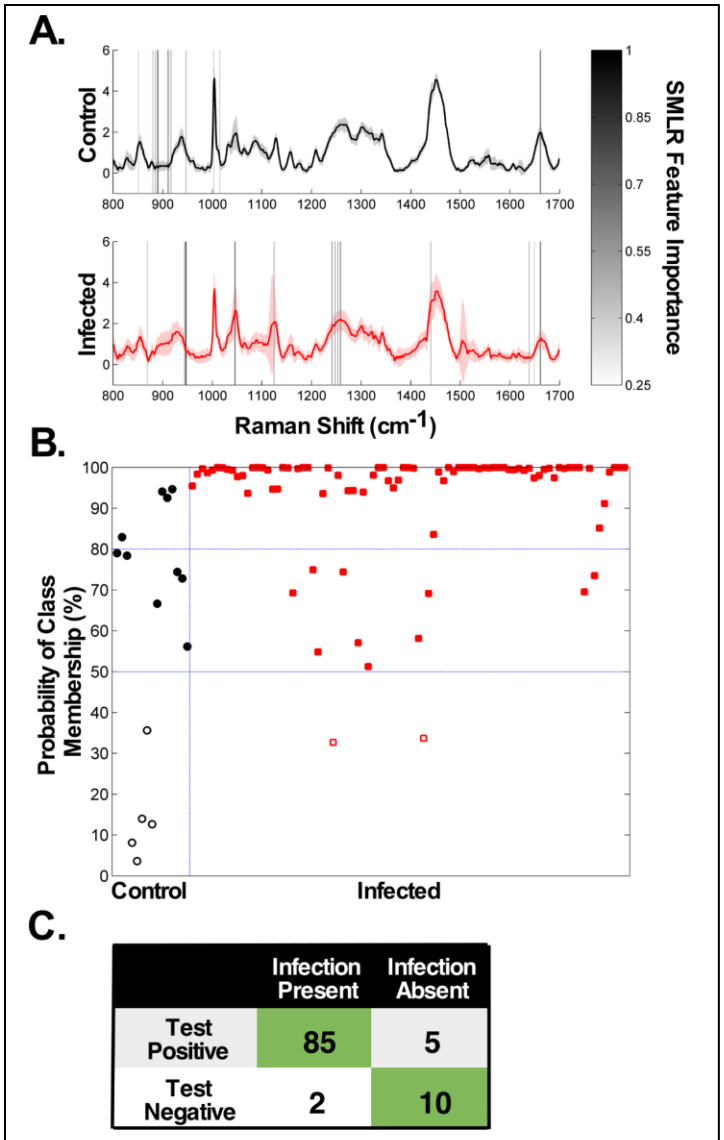


Figure 5.3: Raman microspectroscopy distinguishes infected versus uninfected fetal membrane tissues. A: Mean ± standard deviation Raman spectra of infected tissues compared to control (uninfected) specimens. Gray vertical bands represent biochemical features important for classification based on sparse multinomial logistic regression (SMLR). B: Posterior probability of class membership plot of Raman spectra with respect to infected and uninfected tissues. Filled markers represent correctly classified Raman spectra and unfilled markers represent incorrectly classified spectra. C: Confusion matrix showing the performance of the SMLR classifier.

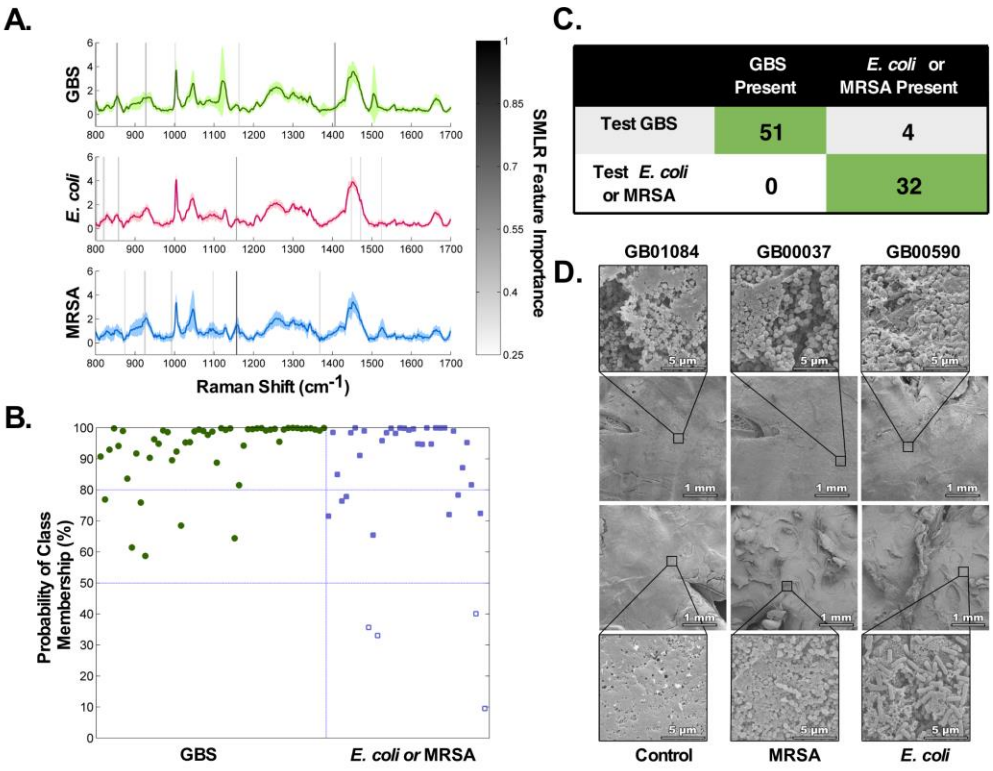


Figure 5.4: Raman microspectroscopy of *ex vivo* infected fetal membrane tissues identifies and differentiates bacterial cells within tissues. A: Mean ± standard deviation Raman spectra for Group B *Streptococcus* strains (GB01084, GB00037, and GB00590), *E. coli*, and *S. aureus* strain USA300 (MRSA) infected tissues. Gray vertical bands represent biochemical features important for classification based on sparse multinomial logistic regression (SMLR). B: Posterior probability of class membership plot for each tissue type. Filled markers represent correctly classified Raman spectra and unfilled markers represented incorrectly classified spectra. C: Confusion matrix representing the performance of the SMLR classifier for each tissue type. D: Scanning electron microscopy images of fetal membrane tissues used for Raman analysis to verify the presence of bacteria at the location of Raman measurements. A small cut was made into the membrane tissues to denote the relative location of Raman evaluation. Inserts demonstrate bacterial cells and extracellular polymeric substances, suggestive of biofilms, seen in these locations.

## 5.5 Discussion

GBS remains an important perinatal pathogen despite recommendations to screen and prophylactically treat colonized women during pregnancy. Here, RμS was investigated as a means to characterize and distinguish GBS on agar plates and human fetal membrane tissues infected *ex vivo*. Using RμS, GBS was found to have unique spectral features compared to another Gram-positive bacteria, *S. aureus*, and the Gram-negative perinatal pathogen, *E. coli*. Additionally, spectral patterns of GBS strains varied, suggesting that each strain has a unique spectral signature, while maintaining GBS-common identifiable markers. Qualitative analysis of Raman spectra from bacterial colonies presents differences in the 1121 $cm^{-1}$ (C-C stretching), 1159 $cm^{-1}$ (C-C stretching), 1506 $cm^{-1}$ (C=C stretching), and 1525 $cm^{-1}$ (C=C stretching) Raman bands, which correspond to pigmentation caused by a carotenoid.[15] This pigmentation of GBS cells results from production of beta-hemolysin, a carotenoid pigment and virulence factor. Past studies have shown that GBS pigment demonstrates absorption spectrum strongly resembling carotenoids.[16] GBS beta-hemolysin was originally thought to be a protein and potentially separate from the GBS pigment, but more recent reports indicate that beta-hemolysin is not a protein but a rather a ornithine rhamnolipid identical or very closely related molecules to the GBS pigment.[17] Nonetheless, non-pigmented strains are also capable of causing clinical disease, thus using RμS to screen for pigment alone would be insufficient.[18] Given that RμS can differentiate colonies on agar plates, it could be used to expedite

bacterial identification in microbiology labs once adequate spectral libraries of bacterial Raman spectra are constructed.

More importantly, RμS is able to discriminate fetal membrane tissues infected with GBS and distinguish these from uninfected tissues or those infected with *E. coli* or MRSA. Spectra from infected and uninfected membrane tissue specimens highlight major differences in peak intensity and width for the two groups in Raman bands 880-955 $cm^{-1}$, 1110-1128 $cm^{-1}$, 1492-1530 $cm^{-1}$, and 1645-1672 $cm^{-1}$ (Figure 3A). The Raman band 880-955 $cm^{-1}$ is mainly related to carbohydrates and proteins as seen at 920 $cm^{-1}$ due to C-C stretch of proline and 938 $cm^{-1}$ due to C-C stretch of alpha helix and C-O-C glycosidic linkages. In the second Raman band of 1110-1128 $cm^{-1}$, the peak at 1126 $cm^{-1}$ is due to C-O stretching in carbohydrates, which appear to be related to differences seen in the Raman spectra when comparing uninfected versus infected fetal membrane tissues. The third Raman band 1492-1530 $cm^{-1}$ includes peaks at 1504 $cm^{-1}$ and 1526 $cm^{-1}$ both due to C=C stretching related to carotenoids. The Raman band 1645-1672 $cm^{-1}$ mainly features the peak at 1662 $cm^{-1}$ due to C=O stretching related to amide I. Furthermore, a higher standard deviation is present in Raman spectra of GBS-infected tissues at 1121 $cm^{-1}$ (C-C stretching) and 1506 $cm^{-1}$ (C=C stretching) since these features are more intense in GB01084 compared to GB00037 and GB00590. To identify more subtle spectral differences, SMLR-FI was implemented across tissue types. Features important for characterizing uninfected fetal membrane tissue include 889 $cm^{-1}$ (SMLR-FI=0.56) related to biological protein structures in tissue, 910 $cm^{-1}$ (SMLR-FI=0.87) related to fatty

acids, and 1661 $cm^{-1}$ (SMLR-FI=0.56) as part of amide I (C=O stretch). Twelve features above a 25% SMLR-FI were found to be important for distinguishing GBS-infected tissue, including 853 $cm^{-1}$ (SMLR-FI=0.50) as part of tyrosine and 1406 $cm^{-1}$ (SMLR-FI=0.76) related to lipids. Tissues infected with *E. coli* presented ten features above the SMLR-FI threshold and include 858 $cm^{-1}$ (C-C stretch, SMLR-FI=0.58) and 1157 $cm^{-1}$ (C-C and C-N stretching in proteins, SMLR-FI=0.53). For MRSA-infected tissue, the Raman peak at 1157 $cm^{-1}$ (C-C related to carotenoid, SMLR-FI=1.0) was most important for distinguishing this infection in tissue relative to nine other features above 25% SMLR-FI. Here, the 1157 $cm^{-1}$ Raman peak is due to C-C stretching of carotenoids since the Raman spectra of MRSA-infected tissue also includes a peak at 1526 $cm^{-1}$ due to C=C stretching of carotenoids.

When compared against *E. coli* or MRSA infected tissue, RμS is able to distinguish GBS infected tissues with 100.0% sensitivity and 88.9% specificity using SEM imaging to confirm bacterial presence at the site of Raman measurements. SEM analysis of these *ex vivo* infected tissues demonstrated bacterial growth in biofilm structures. The biofilm structures seen in our model are similar to bacterial biofilms identified in human amniotic fluid and on fetal membrane tissues taken from women with confirmed intra-amniotic infection.[19,20]

In conclusion, Raman spectroscopy has the ability to detect bacterial infection of human fetal membrane tissue and distinguish between GBS versus MRSA or *E. coli*. As this technology progresses it holds promise to identify GBS and other bacteria on different tissues, thereby providing more rapid assessment than traditional diagnostic microbiology. More work is needed to reach this goal

including construction of bacterial spectral libraries to compare biochemical features between strains, further engineering to allow in vivo spectral measurements on various tissues, and evaluating polymicrobial infections to determine if spectral signatures of pathogenic bacteria can be isolated in the presence of normal bacterial communities or microbiota. Future studies will need to examine human tissues obtained from women with intra-amniotic infection to further demonstrate the relevance of our *ex vivo* models and the capabilities of this emerging technology. This study takes the first step to expand research in this area.

## 5.6 Acknowledgements

The authors would like to thank colleagues at the Vanderbilt Biophotonics Center and the Vanderbilt Pre$^3$ Initiative for providing feedback in preparation of this manuscript. This work was supported by a Department of Defense, Air Force of Scientific Research, National Defense Science and Engineering Graduate (NDSEG) Fellowship, [32 CFR 168a to O.D.A.], a VUMC Faculty Research Scholars Award (to R.S.D), a Career Development Award [IK2BX001701 to J.A.G] from the Office of Medical Research, Department of Veterans Affairs, and funding from The Global Alliance to Prevent Prematurity and Stillbirth (to D.M.A. and S.D.M.). Additional support was provided by the National Institutes of Health Grant R01 [HD090061 to J.A.G.] and National Institutes of Health Grant R01 [HD081121 to A.M-J.]. Core Services including use of the Cell Imaging Shared Resource were

performed through support from Vanderbilt Institute for Clinical and Translational Research program supported by the National Center for Research Resources, [UL1 RR024975-01], and the National Center for Advancing Translational Sciences, [2 UL1 TR000445-06]. De-identified, human fetal membrane tissue samples were provided by the Cooperative Human Tissue Network at Vanderbilt University, which is funded by the National Cancer Institute.

5.7 References


1. A. C. Seale, H. Blencowe, F. Bianchi-Jassir, N. Embleton, Q. Bassat, J. Ordi, C. Menéndez, C. Cutland, C. Briner, J. A. Berkley, J. E. Lawn, C. J. Baker, L. Bartlett, M. G. Gravett, P. T. Heath, M. Ip, K. Le Doare, C. E. Rubens, S. K. Saha, S. Schrag, A. S. Meulen, J. Vekemans, and S. A. Madhi, Clin. Infect. Dis., **2017**, 65(Suppl 2):S125.

2. J. Verani, L. McGee, and S. Schrag, Prevention of Perinatal Group B Streptococcal Disease - Revised Guidelines from CDC, 2010. MMWR Recommendations and Reports, Department of Health and Human Services, Centers for Disease Control and Prevention. **2010**, 59(RR-10), 1.

3. S. J. Schrag and J. R. Verani, Vaccine, **2013**, 31S:D20.

4. B. J. Stoll, N. I. Hansen, P. J. Sánchez, R. G. Faix, B. B. Poindexter, K. P. Van Meurs, M. J. Bizzarro, R. N. Goldberg, I. D. Frantz III, E. C. Hale, S. Shankaran, K. Kennedy, W. A. Carlo, K. L. Watterberg, E. F. Bell, M. C. Walsh, K. Schibler, A. R. Laptook, A. L. Shane, S. J. Schrag, A. Das, and R. D. Higgins, Pediatrics, **2011**, 127, 817.

5. K. Puopolo, L. Madoff, and E. Eichenwald, Pediatrics, **2005**, 115, 1240.

6. A. A. Rabaan, J. V. Saunar, A. M. Bazzi, and J. L. Soriano, J. Med. Microbiol., **2017**, 66, 1516.

7. K. Rebrosova, M. Siler, O. Samek, F. Ruzicka, S. Bernatova, V. Hola, J. Jezek, P. Zemanek, J. Sokolova, and P. Petras, Sci. Rep., **2017**, 7, 14846.

8. B. D. Beier, R. G. Quivey, Jr., and A. J. Berger, J. Biomed. Opt., **2010**, 15, 066001.

9. S. Klob, B. Kampe, S. Sachse, P. Rosch, E. Straube, W. Pfister, M. Kiehntopf, and J. Popp, Anal. Chem., **2013**, 85, 9610.

10. R. S. Doster, L. A. Kirk, L. M. Tetz, L. M. Rogers, D. M. Aronoff, and J. A. Gaddy, J. Infect. Dis., **2017**, 215, 653.

11. J. Iqbal, K. R. Dufendach, J. C. Wellons, M. G. Kuba, H. H. Nickols, O. G. Gómez-Duarte, and J. L. Wynn, Infect. Dis., **2016**, 48, 461.

12. O.D. Ayala, C. A. Wakeman, I. J. Pence, C. M. O'Brien, J. A. Werkhaven, E. P. Skaar, and A. Mahadevan-Jansen, Anal. Methods, **2017**, 9, 1864.

13. B. Krishnapuram, L. Carin, M. A. T. Figueiredo, and A. J. Hartemink, IEEE Trans. Pattern Anal. Mach. Intell., **2005**, 27, 957.

14. I. J. Pence, C. A. Patil, C. A. Lieber, and A. Mahadevan-Jansen, Biomed. Opt. Express, **2015**, 6, 2724.

15. F. S. de Siqueira e Oliveira, H. E. Giana, and L. Silveira, Jr., J. Biomed. Opt. **2012**, 17, 107004.

16. M. Rosa-Fraile, S. Dramsi, and B. Spellerberg, FEMS Microbiology Reviews, **2014**, 38, 932.

17. C. Whidbey, M. I. Harrel, K. Burnside, L. Ngo, A. K. Becraft, L. M. Iyer, L. Aravind, J. Hitti, K. M. Adams Waldorf, and L. Rajagopal, J. Exp. Med., **2013**, 210, 1265.

18. C. Gendrin, J. Vornhagen, B. Armistead, P. Singh, C. Whidbey, S. Merillat, D. Knupp, R. Parker, L. M. Rogers, P. Quach, L. M. Iyer, L. Aravind, S. D. Manning, D. M. Aronoff, and L. Rajagopal, J. Infect. Dis., **2017**, 217, 983.

19. R. Romero, C. Schaudinn, J. P. Kusanovic, A. Gorur, F. Gotsch, P. Webster, C. L. Nhan-Chang, O. Erez, C. J. Kim, J. Espinoza, L. F. Goncalves, E. Vaisbuch, S. Mazaki-Tovi, S. S. Hassan, and J. W. Costerton, Am. J. Obstet. Gynecol., **2008**, 198, 135.e1.

20. D. Schmiedel, J. Kikhney, J. Masseck, P. D. Rojas Mencias, J. Schulze, A. Petrich, A. Thomas, W. Henrich, and A. Moter, Clin. Microbiol. Infect., **2014**, 20, O538.

# CHAPTER 6

# 6. CONCLUSIONS

## 6.1 Summary

This dissertation investigated the use of Raman microspectroscopy to characterize bacteria that cause infectious diseases. As covered in the introduction for each of the chapters, there are a myriad of current clinical challenges dealing with detecting the presence of pathogens and identifying bacteria either at the genus or species level. The motivation for this is the need to improve diagnostic approaches by making them more accurate, fast, and intuitive to allow care providers to make a direct response on the outcome. Furthermore, clinical challenges dealing with bacterial infections are constantly battling with evolving resistance to antibiotics. This is major challenge that has come at the forefront of the Centers for Disease Control and Prevention (CDC), pushing researchers to develop more reliable diagnostic approaches that will guide the prescription of antibiotics with the goal of reducing antibiotic resistance. To this end, this dissertation focused on the potential of using Raman spectroscopy for identifying pathogens in different environments and assigning biomarkers important for discrimination using various statistical analysis methods.

Following the introduction and background chapters of this thesis, Chapter 3 started with characterizing the three main otopathogens that cause acute otitis media using Raman microspectroscopy. Initially, the three main pathogens (*H.*

*influenzae*, *M. catarrhalis*, and *S. pneumoniae*) were cultured on chocolate agar to suffice the needs of *M. catarrhalis*, a fastidious organism. The goal was to collect Raman spectra directly from the bacterial colonies on the agar plate as to minimize changes in the biochemical structure. While irradiating the colonies with 785 nm light, the majority of the source was absorbed due to the dark brown pigment of the chocolate agar. This caused a substantial drop in the signal to noise ratio in the Raman spectra that were detected, making it challenging to accurately characterize the biochemical signatures of bacteria. Therefore, there was a need to optimize the culture media used to grow the bacteria. The design criteria for this required that it would be able to grow the three microorganisms being studied and contain few ingredients as to minimize contribution to Raman measurements. Mueller-Hinton agar was found to contain few ingredients to grow pathogens and is transparent, minimizing laser absorption and fluorescence generation, and consequently noise contribution. After initial testing, it was found that MH agar provided a 10-fold reduction in Raman measurement noise compared to spectra collected from bacteria colonies on chocolate agar.

Next, the three main otopathogens were successfully characterized using Raman microspectroscopy from direct bacterial colony measurements. Implementation of a machine learning algorithm called sparse multinomial logistic regression (SMLR) allowed biochemical features to be ranked with importance for accurately identifying each of the three pathogens. These features were trained and evaluated using k-fold cross-validation that resembled identification of a bacterial colony. These features for identification were then used to identify a small

set of bacterial colonies cultured from clinical samples (n=3) derived from patients suffering from recurrent otitis media. The biomarkers were successful in identifying the pathogen that had been cultured from the clinical specimens.

Findings from work in Chapter 3 show the potential of Raman microspectroscopy to accurately characterize bacteria, identify biochemical features important for discrimination, and feasibility of using this technique for identifying bacterial colonies from clinical samples. This work would be useful for researchers in need of accurately characterizing bacterial samples without using non-ionizing radiation, non-invasively probing bacterial samples, minimizing sample preparation time, and building a spectral library of biochemical features important for detection of bacterial signatures.

Chapter 4 took a deeper look into the ability of Raman microspectroscopy and multi-step statistical analysis to detect and identify isogenic variants of *S. aureus*. There is a critical need to be able to accurately identify these pathogens *in situ* due to their high infection rate in clinical settings. Furthermore, small colony variants (SCVs) of *S. aureus* can produce more persistent infections typically seen in patients seeking treatment. For this assessment, various isogenic variants of *S. aureus* that were methicillin-resistant and methicillin-sensitive were evaluated along with SCVs that were methicillin-sensitive and aminoglycoside-resistant using Raman microspectroscopy. Bacterial strains were cultured on MH agar and measured after incubation using 785 nm excitation. After processing the spectra for each of the strains, major Raman peaks related to pigmentation were detected. Principal component analysis (PCA) was performed which included reducing the

full-spectrum to spectral regions of interest was implemented. These spectral regions were then evaluated using a discriminant analysis to determine classification of each bacteria. Results from this work showed that Raman microspectroscopy can be used to identify genetic variants of *S. aureus*, discriminate between methicillin-resistant and methicillin-sensitive strains, and determine biochemical features important for discrimination of various bacterial strains. This body of work opened the path towards investigating other isogenic variants that include non-phenotypic differences for studying the evolution of bacterial resistance.

Chapter 5 explored a new clinical challenge related to group B *Streptococcus* (GBS) infections and the risk they impose on laboring mothers. This a major problem especially for mothers that deliver at preterm since they have a higher rate of not being screened for GBS infections. Furthermore, the ability to detect and identify bacteria in tissue biofilms, which is how these GBS infections typically form, would potentially open other doors of research. This project was a true multidisciplinary collaboration between a physician, infectious diseases researchers, and biophotonics researchers. Similar to the previous two chapters, clinical strains of GBS were characterized with Raman microspectroscopy. After unique signatures were seen from pigmented strains versus other GBS strains that were not pigmented, the challenge grew to be able to identify these pathogens in tissue versus other common pathogens seen on placental tissue. For this study, fetal membrane tissues excised from human placental tissues from term, healthy, non-laboring caesarean-section births were collected to make punch biopsies for

our measurements. Each collected tissue was treated for any bacterial infection and then treated with a respective pathogen (GBS, *E. coli*, and *S. aureus*). Discrimination analysis was performed on each treatment group of tissue and resulted in a classification accuracy of 91% from 34 tissue samples and verified using scanning electron microscopy (SEM). As a potential point of care diagnostic tool, RS may improve current approaches used for detection of GBS infection that rely on time consuming (24-72 hours) culture and polymerase chain reaction (PCR) systems that may not be readily available in all clinical settings. These findings open the doors for future studies that will investigate polymicrobial infections and their effects on tissue environments.

Appendix 1 reconnected with Chapter 3's clinical challenge of otitis media. However, it included an optical design challenge that would test whether Raman spectroscopy would be able to provide biochemical information from patients suffering from recurrent otitis media *in vivo*. The initial pilot study included the use of a forward facing fiber-optic Raman probe at 785 nm using 80 mW to irradiate the tympanic membrane of young patients undergoing myringotomy and tympanostomy tube insertion. From the first data set using this probe, the Raman signal to noise ratio was low and a new design needed to be implemented to guide probe placement toward the tympanic membrane. From the new Raman that was designed, which included illumination and real-time imaging of the measurement location in addition to Raman excitation and collection fibers, a pilot study of 17 patients have been recruited while optimizing acquisition parameters. Findings from these pilot studies show that *in vivo* RS via a fiber-optic probe to evaluate the

tympanic membrane is possible and has the potential to streamline clinical decisions by informing physicians in the clinic if there is an acute infection based on the presence/absence of fluid, fluid type, and detection of bacterial invasion in the fluid.

## 6.2 Recommendations

There are various recommendations that can be made across the main topics in this dissertation. The following next steps for each part of this thesis illustrate advancements in experimental design and outcomes.

1) Characterize AOM bacteria in more complex environments

In regards to the characterization of the main bacteria that cause acute otitis media (AOM), there is a need to be able to detect the presence and identify these otopathogens in polymicrobial environments. The short term goal for this project would be to culture the three main bacteria that cause AOM in a fluid environment and characterize their signatures using Raman spectroscopy. The long term goal would be to be able to detect and identify pathogens in any fluid environment *in situ*. The environment most relevant to ear infections would be detecting these bacteria in fluid. To accomplish this, first, pure bacterial strains could be prepared in growth media and then measured using Raman spectroscopy (RS). Various concentrations would need to be tested to determine the limit of detection of RS. Next, known concentrations of two different bacteria types can be tested following a similar protocol. Finally, all three bacteria in a mixed fluid sample can be measured using RS and evaluated at specific concentrations, which can be

validated using optical density measurements and colony counts from serial dilutions. A more advanced form of this experiment would include collecting middle ear effusion samples from patients suffering from recurrent OM, evaluate these samples for bacteria presence, and take RS measurements *ex vivo*. This would provide a more realistic environment, which would contain red blood cells (RBCs), white blood cells (WBCs), viruses, and other byproducts that will add to the level of complexity for RS measurements. Statistical analysis for this spectral data may include a model that is able to evaluate various components (fluid (type), bacteria, RBCs, WBCs, and viruses to name a few) to determine their contribution to the Raman signal based on results from non-negative least squares analysis. An extension of this bacterial characterization could also evaluate the impact on identifying pathogens cultured on different agar types and incubation times. Ideally, an RS system could be integrated in an incubator to study their growth.

2) Expand bacterial mutant Raman spectral library

In regards to using Raman spectroscopy to identify bacterial mutants, there are at least a few paths that can build on the work presented in this thesis. The short-term goal would be to evaluate isogenic variants that are linked to non-phenotypic differences to further test RS and the current statistical analysis approach's ability to identify and discriminate these bacteria. The long-term goal would be to characterize various point mutations, single gene mutations, and multiple gene mutations in various strains to evaluate biochemical changes occurring as bacteria develop resistance to antibiotics.

3) Work towards detecting GBS in *in vivo* mouse and humans pregnancy studies

For detecting group B *Streptococcus* (GBS) in a tissue environment, there are various paths that can continue to explore the initial findings of this research. The short term goal includes creating RS maps of the surface tissue to evaluate the changes in biochemical profiles, especially for changes in biofilm density. A higher level study would include evaluation of biofilm tissues to better understand Raman signal contributions from bacteria versus changes in tissue due to bacterial proliferation. This would be provide invaluable insight for understanding the sequelae of invasive infections in tissue using a rapid, non-invasive approach. For the long term, it would be important to investigate if a fiber-optic probe based RS scanning system would be able to measure multiple millimeters of tissue area at a time in an *in vivo* mouse model while maintaining the sensitivity and specificity to identify and discriminate GBS reported in this dissertation. This would have strong value as a point of care diagnostic test that can be first evaluated in an animal model of GBS infection in pregnancy as a controlled study with known bacteria, and further tested in human pregnant patients undergoing routine GBS testing.

4) Create an advanced clinical Raman probe for middle ear infection assessment

Regarding the application of *in vivo* RS for investigating ear infections, an emphasis on optical probe design will be needed. The short term goal will be to further optimize the illumination and Raman collection fiber geometry design in a probe that is <4 mm in diameter in order to fit in most ear specula. A brighter light

source may allow fewer illumination fibers to be used, allowing for an increase in the number of Raman collection fibers. In addition, a curved probe tip may allow more excitation light to be directed at more focused regions of the tympanic membrane, potentially reducing the signal contribution from the strong bone peak seen at 960 $cm^{-1}$. I envision the long-term goal for this project to be a clinical tool that combines RS with optical coherence tomography (RS-OCT) in a handheld otoscope-like device to measure both the biochemical changes due to otitis media and study any biofilm development in the middle ear, respectively. Together, the complementary nature of these optical technologies will provide clinicians with all the information necessary to diagnose, treat, track, and guide patient care.

## 6.3 Contributions to the Field and Societal Impact

This dissertation includes research that contributes to the fields of biophotonics, microbiology, and otolaryngology. Characterization of the three main pathogens that cause acute otitis media (AOM) using Raman microspectroscopy was instrumental in determining the feasibility and reproducibility of using this technique directly from bacterial colonies. Furthermore, these findings are important in leveraging this spectral technique for tracking biochemical changes during growth of bacteria to better understand their response to various environments. The application of machine learning algorithms to identify biochemical features important for discrimination of the three main bacteria that cause ear infections played a critical role in identifying these pathogens in clinical specimens from patients affected by AOM.

The exploration of using Raman spectroscopy to characterize isogenic variants of *Staphylococcus aureus* led to utilizing a combination of statistical approaches to discriminate antibiotic-resistant pathogens from other strains. This finding is important for future diagnostic developments for detecting the presence of bacteria in patients potentially suffering from an ear infection and distinguishing antibiotic-resistant forms of bacteria to guide clinical treatment.

The ability to distinguish pathogens using an established biofilm tissue model further makes the case of using Raman spectroscopy to investigate bacteria on tissue at various levels. To my knowledge, this is the first report to distinguish perinatal pathogens on human fetal membrane tissue *ex vivo* using Raman microspectroscopy. Although this work does not investigate tissue infected with otopathogens, it directly lends itself for determining the feasibility of identifying pathogens in biofilms seen on the tympanic membranes of patients suffering from chronic otitis media. This work and previous findings by other researchers lay the ground work for the next steps to investigate multi-pathogen environments on tissue, test the potential of distinguishing these pathogens in a biofilm environment in a proven animal model using a clinical Raman spectroscopy system with a fiber-optic probe, and evaluate naturally infected tissue from human patients. These research advances will bring diagnostic solutions to an area of infectious diseases that is in critical need of development.

The development and testing of a research prototype for a fiber-optic Raman spectroscopy probe with image guidance in 17 patients affected by recurrent otitis media highlighted various design and data collection

improvements. Illumination and imaging feedback from the newly designed fiber-optic Raman probe provided guidance for Raman measurements directly from the tympanic membrane without making contact with the membrane. An increase in illumination and Raman collection fibers will further drive this prototype to collect spectral data from the tympanic membrane and middle ear contents more efficiently. These findings along with those from using Raman microspectroscopy have established the ground work and built momentum for utilizing Raman spectroscopy as a point of care diagnostic tool for physicians to guide clinical care for patients suffering from ear infections.

# APPENDIX 1 DEVELOPMENT OF AN IMAGING FIBER-OPTIC RAMAN PROBE FOR CHARACTERIZING RECURRENT OTITIS MEDIA IN VIVO

## A1.1 Abstract

A forward-facing fiber-optic Raman spectroscopy probe was evaluated on patients recruited through a Vanderbilt IRB approved pilot study. Patients undergoing myringotomy with tympanostomy tube insertion were recruited for this study. Prior to optical measurements, any excess ear wax was removed from the ear canal and a white light image of the tympanic membrane was collected. A fiber optic Raman probe was then inserted into the ear speculum and measurements at multiple locations were collected. Raman spectra were analyzed for signal contributions from typical biological markers such as proteins and lipids. After a small pilot group (n=17) was recruited, a new design for a fiber-optic Raman probe that included illumination would help in guiding placement of the probe towards the tympanic membrane. The same protocol as above was followed for spectral acquisition of tympanic membranes. Collected Raman spectra were evaluated comparing factors such as the presence of fluid and the region of the tympanic membrane the Raman measurement was collected.

## A1.2 Objectives

The ability to detect the presence and the identification of bacteria in an infection will permit physicians to prescribe more targeted antibiotics and eliminate unnecessary treatment. This may also reduce the rising number of antibiotic-

resistant bacteria. A tool that is capable of non-invasively probing the molecular makeup of bacteria that cause AOM to identify the bacterial species will aid in providing physicians with the information needed to prescribe the correct antibiotic and decrease the course of infection.

The purpose of this study is to characterize the tympanic membrane (TM), middle ear contents, and middle ear effusion (MEE) (if any) using Raman spectroscopy (RS). RS is a light scattering technique that provides real-time biochemical information about a sample. This sensitive technique has the potential to non-invasively characterize the biochemical profile of both the physiological symptoms and microbiological source of the ear infection. Investigation of the TM, middle ear contents, and MEE will provide insight into the contributing microorganisms and other biological factors that play a role in the pathogenesis of OM. Since a majority of these patients may have previously received antibiotics to treat OM, our approach may aid in identifying MDROs. Raman spectra of the TM, middle ear contents, and MEE (if any) will be collected and analyzed. These measurements will then be used to characterize these components and determine if they are related to specific otopathogens involved in OM.

## A1.3 Methods

### A1.3.1 Raman Spectroscopy

A portable, fiber-optic probe-based Raman spectroscopy (RS) system with a 785 nm diode laser (Innovative Photonics Solutions, Monmouth Junction, NJ)

was used for *in vivo* measurements of the tympanic membrane (TM). The system included an imaging spectrograph (Holospec f/1.8i, Kaiser Optical Systems, Ann Arbor, MI) that was coupled to a thermoelectrically cooled CCD camera (PIXIS: 256BR, Princeton Instruments, Princeton, NJ) (Figure A1.1). A custom designed fiber-optic Raman probe (EmVision, Loxahatchee, FL) was used to deliver 80 mW of near-infrared (NIR) light to the tympanic membrane. Raman probe #1 is a forward-facing design that probes a large volume for Raman scattered light collection. Raman probe #2 is designed to include an illumination fiber set and an imaging bundle, which is in addition to the 785 nm excitation fiber and four Raman collection fibers (Figure A1.2). The portable RS system was wavelength calibrated using a neon argon lamp. The exact wavelength from the excitation source for calculating Raman shifts was determined using two standards, naphthalene and acetaminophen. Prior to measurement collection, the RS system was corrected for spectral response using a tungsten lamp calibrated by the National Institute of Standards and Technology (NIST). Raman spectra were smoothed using a $2^{nd}$ order Savitzky-Golay filter and fluorescence subtracted using a $7^{th}$ degree modified polynomial fit.

Patients recruited for the study were under anesthesia and prepared for myringotomy with tympanostomy tube insertion. Before measurements were collected, all of the operating room lights were turned off to avoid Raman signal from them. The ear canal of the recruited patient was then cleaned and a white light image of the TM was collected. Next, the fiber-optic RS probe was inserted into an ear speculum and fitted to not allow the probe tip to extend beyond the

narrowest part of the speculum (Figure A1.3). Multiple Raman measurements were collected for each ear that was being evaluated. One measurement was collected for each region of the TM (anterior superior, anterior inferior, and posterior inferior) with an integration time of 3 seconds per measurement for RS probe #1 and 3 seconds with 2 accumulations per measurement for RS probe #2.

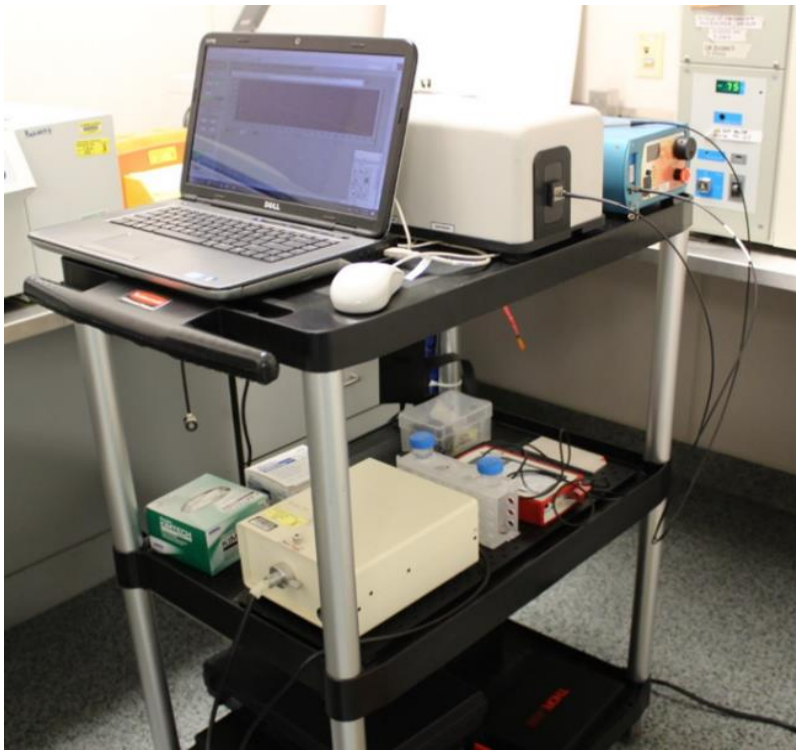

Figure A1.1: Portable Raman spectroscopy (RS) system with a 785 nm excitation source and fiber-optic RS probe. Components of this system include a spectrograph, 785 nm excitation laser source, fiber-optic RS probe, detector, and laptop.

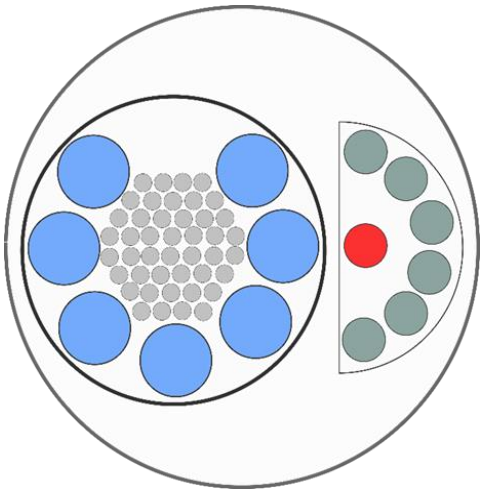

Figure A1.3: Raman fiber-optic probe #2 design. Illumination fibers (blue circles. 7 x 500 µm diameter) surround an imaging bundle (gray hexagons, 6,000 element, 270 µm total diameter) to assist in guiding placement of the RS probe near the TM. The 785 nm excitation (red circle, 300 µm diameter) is surrounded with a semi-circle of 6 Raman scattered light collection fibers (gray circles, 300 µm diameter). The outer diameter of probe #2 is 4 mm.

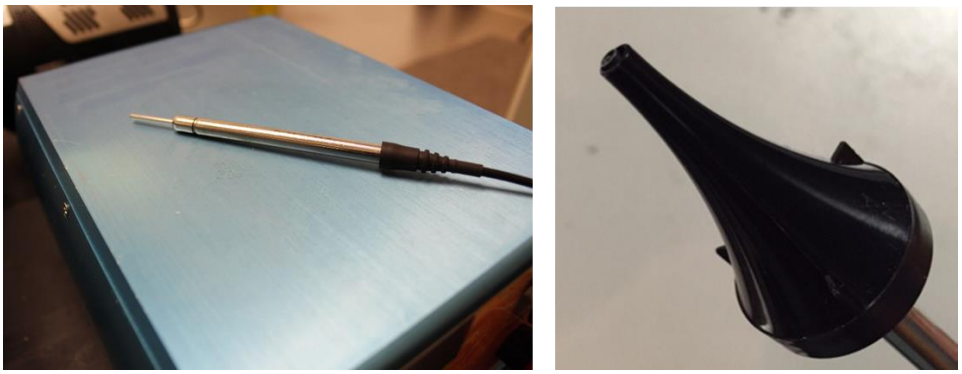

Figure A1.2: Fiber-optic Raman probe used for clinical measurements of the tympanic membrane. Image on right includes the Raman probe placed in an ear speculum (black) with the probe tip flush with the speculum.

### A1.3.2 Spectral Data Analysis

Since this study was performed to determine the feasibility of using Raman spectroscopy for evaluating the tympanic membrane raw fluorescence-subtracted, non-normalized Raman spectra were used for comparison. In addition, the mean and standard deviation of spectra from the same ear for comparison of factors such as normal (no middle ear effusion), the presence of fluid in the middle ear, and fluid type (serous, mucoid, pus, or other).

### A1.3.3 Patient Recruitment and Collection of Middle Ear Effusion Samples

Patients scheduled for myringotomy with tympanostomy tube insertion were recruited using informed, written consent under approved Vanderbilt IRB #161563. Using the first Raman spectroscopy (RS) probe design (RS probe #1) 17 patients were recruited for the study. With the newer RS imaging probe (RS probe #2) 17 patients were also recruited to evaluate the performance of this newly designed optical probe. Middle ear effusion (MEE) samples were also collected for the same group patients that consented. These clinical specimens were collected at the time of the procedure. Samples were labeled, stored in a biohazard container, and prepared for Raman measurements the same day as collection.

### A1.3.4 Middle Ear Effusion Collection and Evaluation

Collected middle ear effusion (MEE) samples were collected as described and prepared for analysis. About 30 µL of each sample was stored in the fridge for downstream Raman microspectroscopy measurements. Part of the clinical

specimen was then spread on a chocolate agar plate for bacterial growth up to 1 week. Another part (10 µL) of the MEE sample was stored in 50 µL of RNAlater and prepared for polymerase chain reaction (PCR), a method which replicates a specific region of deoxyribonucleic acid (DNA) determined by the primers utilized. A subset of four primers: 1) 16s ribosomal ribonucleic acid (rRNA) of *H. influenzae*, 2) 16s rRNA of *M. catarrhalis*, 3) 16s of *S. pneumoniae* #1, and 4) 16s *S. pneumoniae* #2. The remaining (10 µL) of the MEE specimen was mixed with 1 mL of phosphate buffered saline (PBS) solution and 1.5 mL of SYTO9 (green dye) and propidium iodide (red dye) for evaluation of live and dead bacteria using confocal laser scanning microscopy (CLSM). CLSM is an optical imaging technique that collects fluorescence from the sample at a specific depth that is focused in the detector's pinhole. Preliminary results included in this study were used to test each of these molecular techniques. Therefore, the results collected in the next section are not part of the same sample set.

## A1.4 Results

### A1.4.1 Bacteria Detected in MEE Samples using PCR

Middle ear effusion (MEE) samples were collected upon consent from patients suffering from OM and undergoing myringotomy with tympanostomy tube insertion. A total of 12 MEE clinical specimens were collected (from 8 patients) and processed to determine the feasibility of using PCR with these samples. About 62% of samples were either mucoid or serous and ~38% were determined to be

pus by Dr. Jay Werkhaven. Each of the bacterial identification primers was tested with the 12 MEE samples (Figures A1.4-6). Across all samples, PCR findings revealed that *S. pneumoniae* (100% of samples), *H. influenzae* (75% of samples), and *M. catarrhalis* (17% of samples) were present. A summary of these findings is included in Table A1.1.

Detection of live vs. dead bacteria was evaluated in three separate MEE samples from those described above to determine feasibility of using CLSM for analysis of these samples. Preliminary findings from these MEE samples show the presence of both live and dead bacteria in each of the samples (Figure A1.7). As can be seen in each of the CLSM images, a biofilm like matrix appears potentially due to the mucoid nature of the MEE samples.

Preliminary findings from PCR and CLSM show that it is possible to use MEE samples and characterize them by identifying bacteria and determining live versus dead bacteria in these specimens.

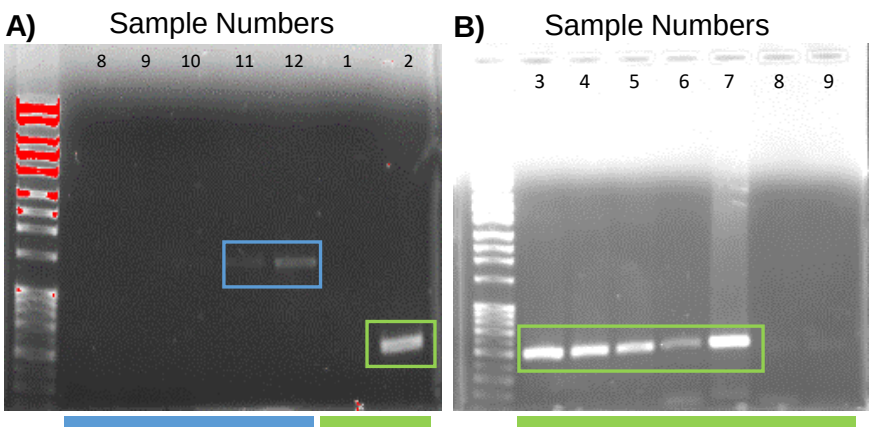


Figure A1.4: Polymerase chain reaction (PCR) of MEE samples for detection of bacteria. A) Bands highlight detection of M. catarrhalis and S. pneumoniae in respective MEE samples. B) Bands highlight detection of S. pneumoniae in respective MEE samples.

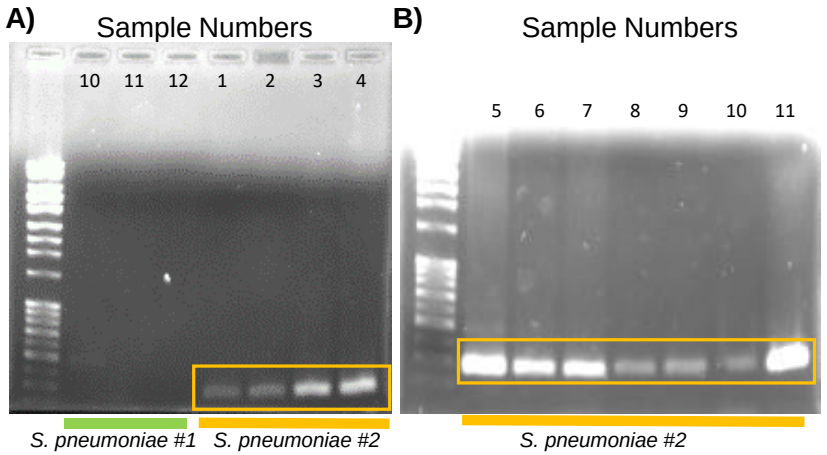


Figure A1.5: Polymerase chain reaction (PCR) of MEE samples for detection of bacteria. A) and B) Bands highlight detection of S. pneumoniae in respective MEE samples.

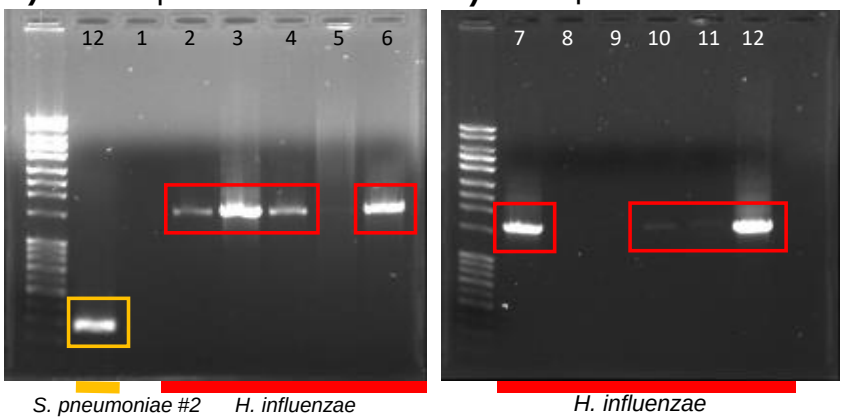


Figure A1.6: Polymerase chain reaction (PCR) of MEE samples for detection of bacteria. A) Bands highlight detection of S. pneumoniae and H. influenzae in respective MEE samples. B) Bands highlight detection of H. influenzae in respective MEE samples.

Table A1.1: Summary of collected MEE samples evaluated with PCR for bacterial identification.

| Sample # | | | |
|---|---|---|---|
| 1 | - | - | + (S.pn.2) |
| 2 | + | - | + |
| 3 | + | - | + |
| 4 | + | - | + |
| 5 | +* | - | + |
| 6 | + | - | + |
| 7 | + | - | + |
| 8 | - | - | + (S.pn.2) |
| 9 | - | - | + (S.pn.2) |
| 10 | + | - | + (S.pn.2) |
| 11 | + | + | + (S.pn.2) |
| 12 | + | + | + (S.pn.2) |

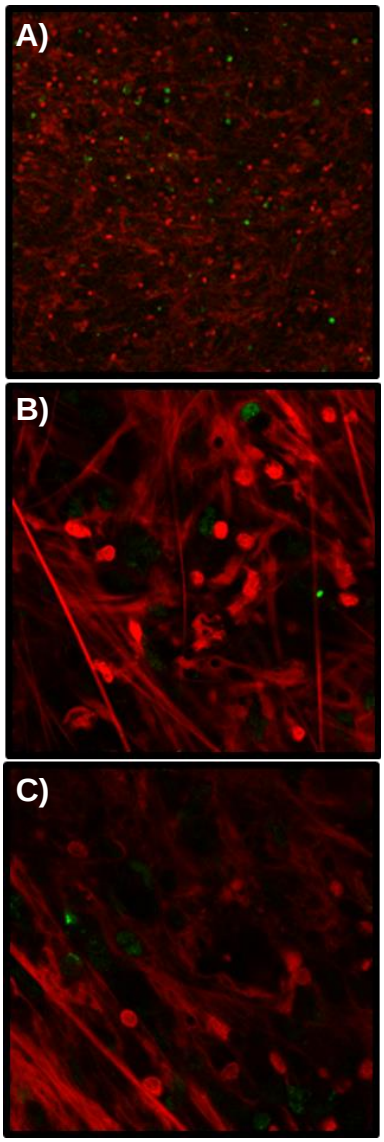


Figure A1.7: CLSM images of live (green) and dead (red) bacteria in MEE samples. A) MEE sample 1, B) MEE sample 2, and C) MEE sample 3. Streaks shown in images are thought to be due to biofilm present in the clinical samples.

### A1.4.2 Raman Spectra Collected Using Raman Probe #1

Raman scattered light was detected from our first *in vivo* RS measurements of a human TM in the operating room. Raman spectra of three different regions (Region #1: anterior superior; Region #2: anterior inferior; Region #3: posterior inferior) of the TM were collected and compared for the first 7 patients that were enrolled in the study. White light images show the TM prior to RS measurements and surgical incision for each of the patients. In addition, a summary table for each patient is provided that includes age, diagnosis, MEE type and color (if any), and outcome of the culture from MEE (if any).

Patient #1 presented with bilateral recurrent OM (Figure A1.8). It was found that the patient contained red mucoid MEE in both ears. Raman measurements were only obtained from the right ear of the patient. However, MEE was collected from both ears and cultured (Figure A1.9). Raman spectra presented various peaks at 960 $cm^{-1}$ (P-O symmetric stretch, bone), 1003 $cm^{-1}$ (phenylalanine), 1069 $cm^{-1}$ (phosphate), 1251 $cm^{-1}$ (Amide III), 1335 $cm^{-1}$ (nucleic acids), 1398 $cm^{-1}$ (uracil, adenine), 1451 $cm^{-1}$ ($CH_3CH_2$ deformations), and 1661 $cm^{-1}$ (C=O stretch, Amide I) (Figure A1.10). The strong and narrow Raman peak at 960 $cm^{-1}$ is most likely due to bone signal from the malleus, which is in direct contact with the TM on the middle ear space side. Cultures from both ears of patient #1 presented growth of bacteria. The specific bacteria type was not initially evaluated for these samples.

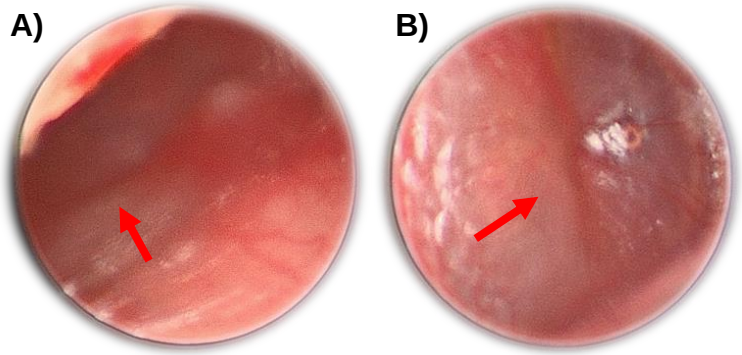


Figure A1.8: White light images of a human tympanic membrane (red arrows) of patient #1 affected with recurrent otitis media with MEE in both ears. A) Left ear and B) right ear.

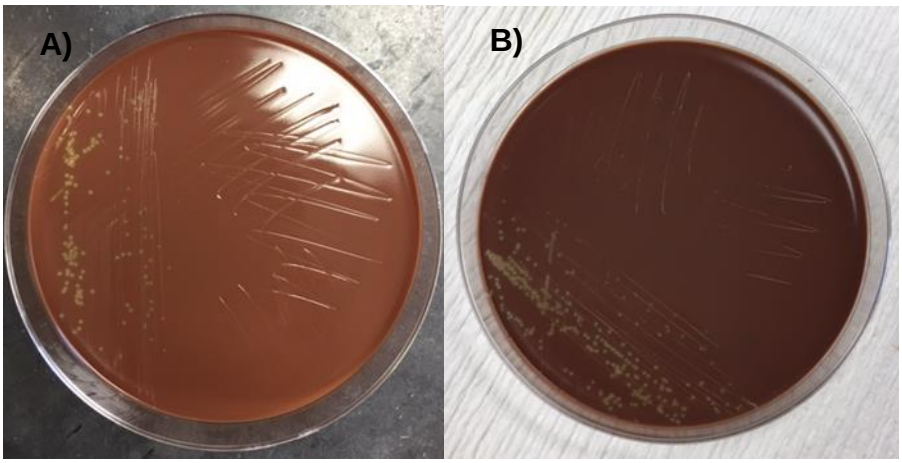


Figure A1.9: Cultures of middle ear effusion collected from patient #1. A) Left ear and B) right ear.

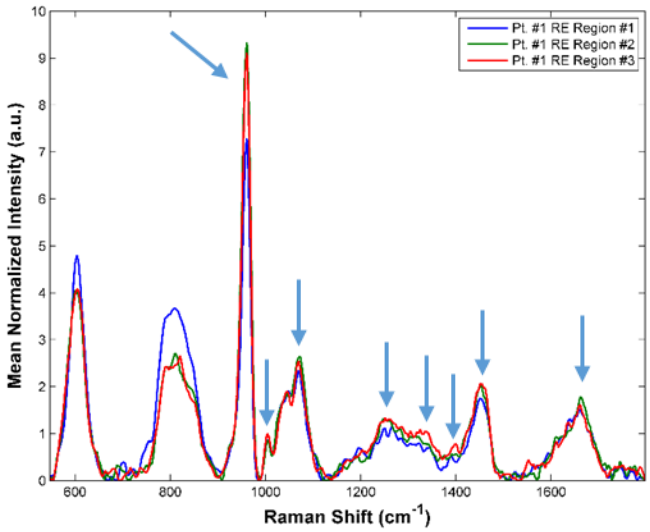


Figure A1.10: Raman spectra collected from the right ear (recurrent OM with MEE) of patient #1 using RS probe #1. Blue arrows highlight major Raman bands of potential interest for spectral analysis.

Patient #2 presented with a case of recurrent OM and bilateral red fluid that produced a positive culture in the left ear and a negative culture in the right ear. White light images of both ears show high severe inflammation and erythema in the left ear compared to minimal inflammation in the right ear of patient #2 (Figure A1.11). The Raman spectra were comparable, but the right ear presented with a stronger phosphate band at ~960 $cm^{-1}$ (Figures A1.12-13). This peak may have presented stronger in the right ear due to less inflammation compared to the left ear, which presented a positive culture on chocolate agar (Figure A1.14).

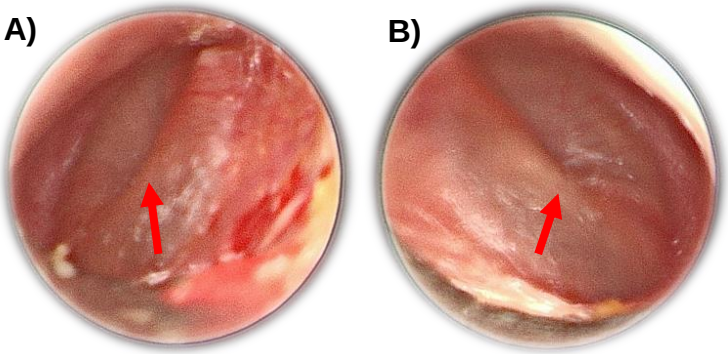


Figure A1.11: White light images of a human tympanic membrane (red arrows) of patient #2 affected with recurrent otitis media with MEE in both ears. A) Left ear and B) right ear.

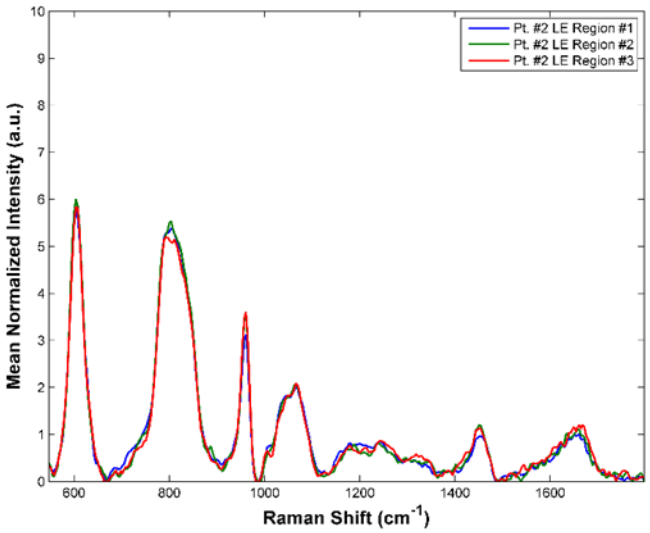


Figure A1.12: Raman spectra collected from the left ear (recurrent OM with MEE) of patient #2 using RS probe #1.

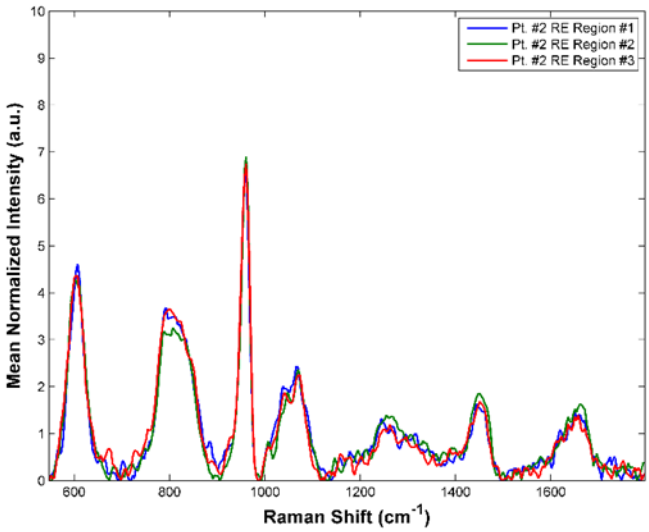


Figure A1.13: Raman spectra collected from the right ear (recurrent OM with MEE) of patient #2 using RS probe #1.

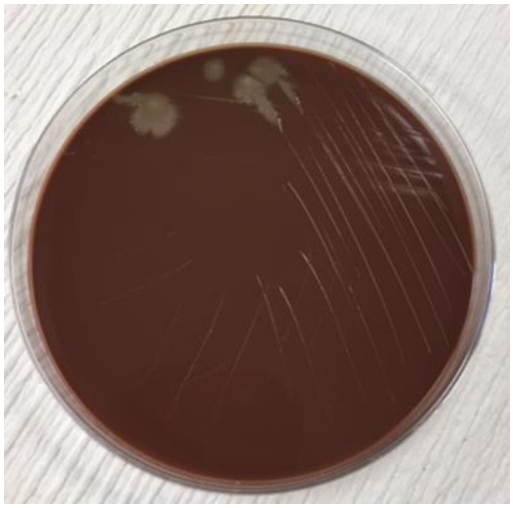

Figure A1.14: Culture of middle ear effusion collected from patient #1's left ear.

To highlight a normal case (no fluid present at the time of myringotomy), patient #4 presented with bilateral recurrent OM, but contained no fluid in either ear. White light images present inflammation in the right ear and erythema in both TMs (Figure A1.15). Raman spectra present with different peak intensities at 960 $cm^{-1}$ for two of the regions (region #2 and 3) (Figures A1.16-17).

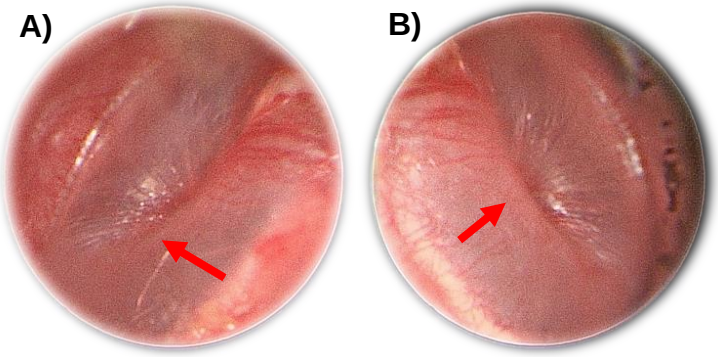


Figure A1.15: White light images of a human tympanic membrane (red arrows) of patient #4 affected with recurrent otitis media with no MEE in either ear. A) Left ear and B) right ear.

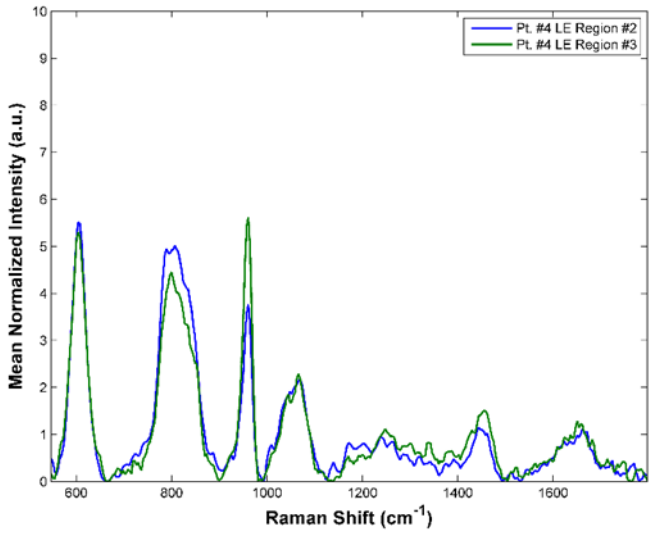


Figure A1.16: Raman spectra collected from the left ear (recurrent OM with no MEE) of patient #4 using RS probe #1.

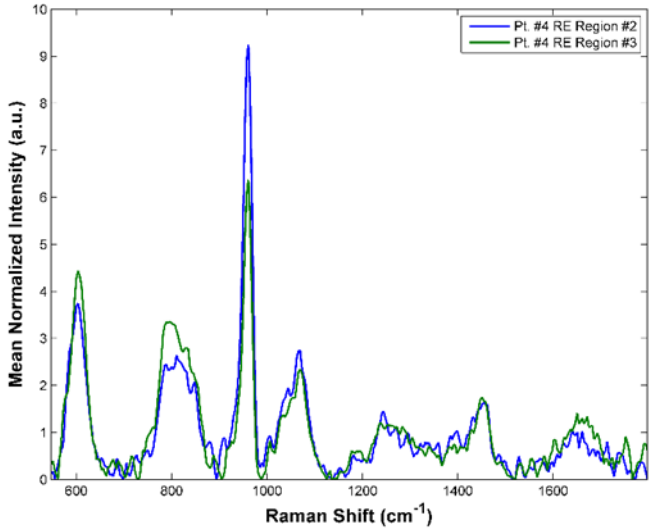


Figure A1.17: Raman spectra collected from the right ear (recurrent OM with no MEE) of patient #4 using RS probe #1.

Patient #6 presented with recurrent OM and bilateral MEE (red pus) as seen in the white light images (Figure A1.18). A culture was positive for the left ear (Figure A1.19). Raman bands across the different regions were similar to previous measurements, although the 960 $cm^{-1}$ peak in the right ear (region #3, posterior inferior) had a higher intensity (Figures A1.20-21).

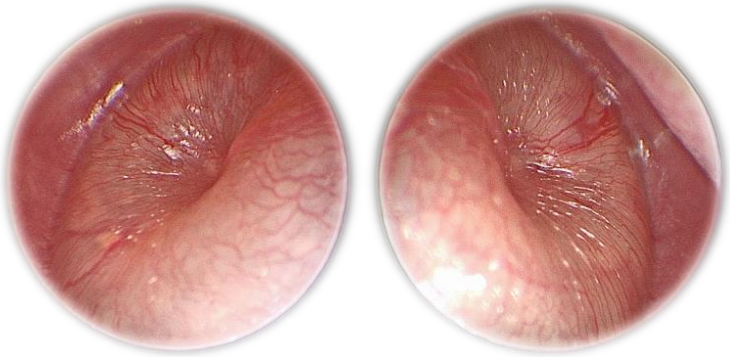

Figure A1.18: White light images of a human tympanic membrane (red arrows) of patient #6 affected with recurrent otitis media with MEE. A) Left ear and B) right ear.

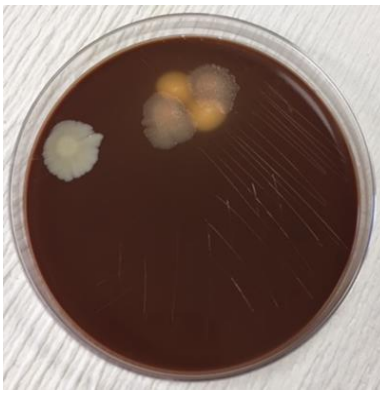

Figure A1.19: Culture of middle ear effusion collected from patient #6's left ear.

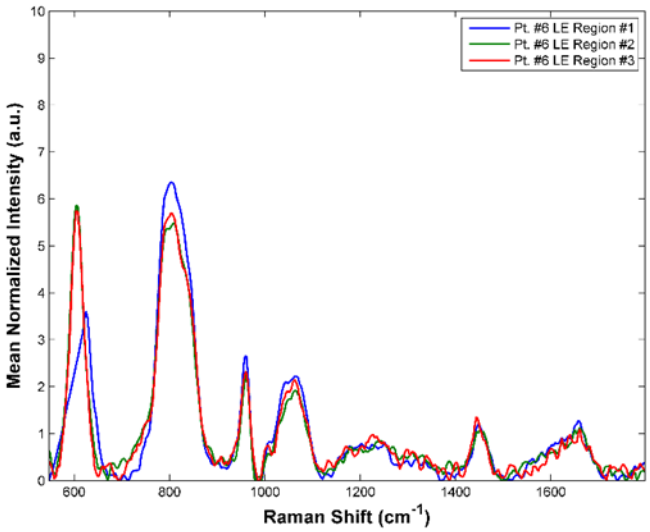


Figure A1.20: Raman spectra collected from the left ear (recurrent OM with MEE) of patient #6 using RS probe #1.

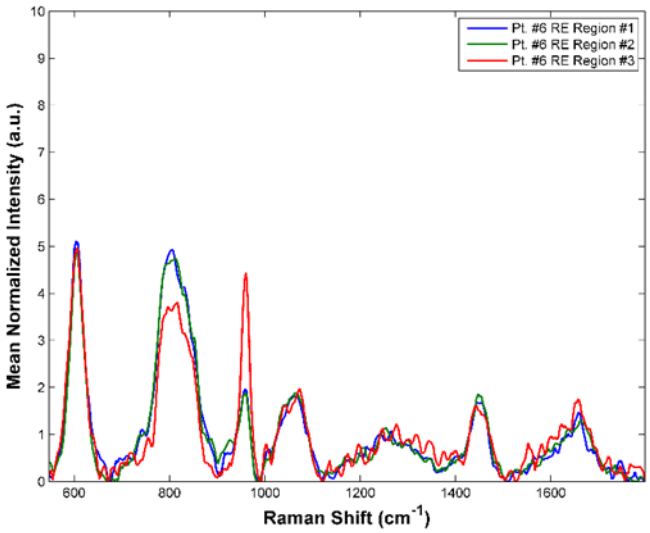


Figure A1.21: Raman spectra collected from the right ear (recurrent OM with MEE) of patient #6 using RS probe #1.

A1.4.3 Raman Spectra Collected Using Raman Probe #2

Alignment of the fiber-optic Raman probe #2 was tested on the spectrograph of the RS portable system. Pointing the tip of the RS probe towards a neon argon source illuminated only 4 Raman collection fibers (Figure A1.22). The RS probe was adjusted to point at the neon argon source at different angles to determine why two fibers were not efficiently collecting any light. It was determined that the two Raman collection fibers that were not collecting light were located at the ends of the semicircle, which was also offset from the surface of the probe toward the inside of the probe. This may make it more challenging to efficiently collect Raman scattered light into the Raman collection fibers.

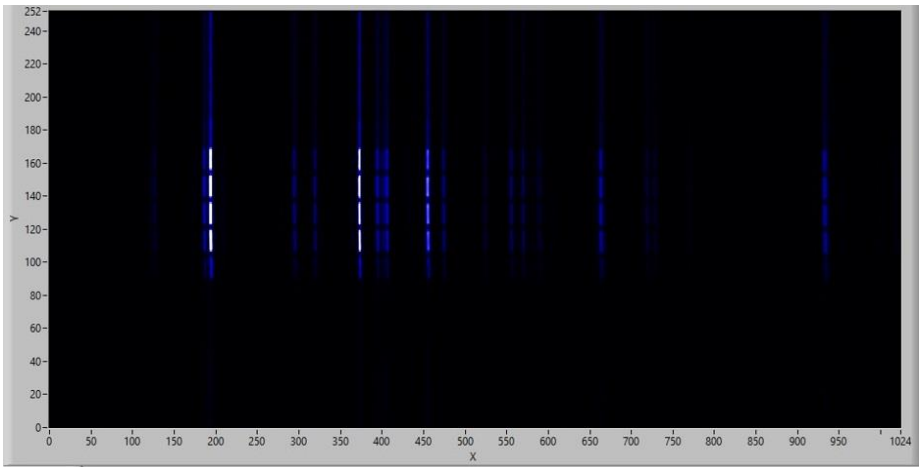


Figure A1.22: Fiber alignment of the RS probe #2 pointing at a neon argon source. Only 4 of the 6 fibers are shown due to design constraints.

This fiber-optic RS probe was still tested to evaluate the design of the illumination fibers and imaging bundle to guide RS measurements in the ear. A phantom tissue model was created using turkey deli meat and Vitamin E (high Raman scattering) to estimate the penetration depth of this new probe. Multiple layers of deli meat were placed on top of the Vitamin E sample and RS measurements were collected. A non-negative least squares model was used to calculate the coefficients for each the tissue and Vitamin E over depth (mm). From the plot, it was determined that the penetration depth at the 1/e falloff is ~1 mm (Figure A1.23).

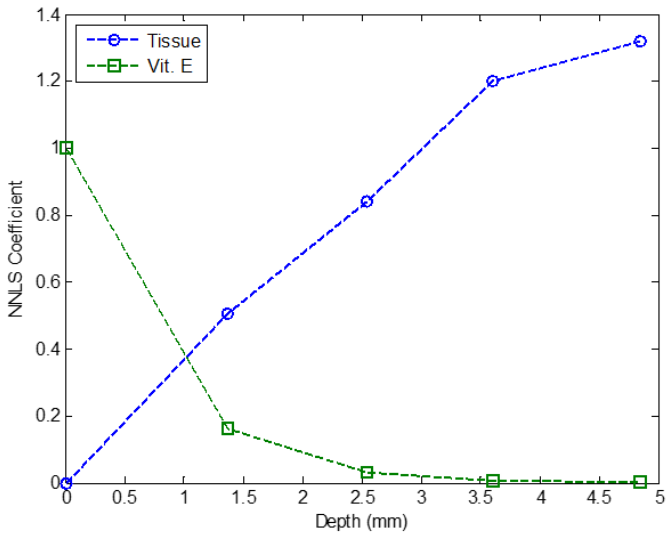


Figure A1.23: Non-negative least squares coefficient plot to determine light penetration depth when measuring Raman signal of a vitamin E capsule under deli meat.

After adjusting the acquisition parameters to 3 seconds and 2 accumulations (total 6 second measurement) compared to the 3 seconds and 1 accumulation used on the first 14 patients of this study, Raman spectra were compared for patients with MEE compared to normal (no MEE) (Figure A1.24). In this preliminary analysis, 17 Raman spectra were collected where 14 measurements from patients contained MEE and 3 measurements did not contain fluid (n=3 patients total). Gray bands indicate spectral regions that are visually different based on the mean and standard deviation of each class (normal (no fluid) vs. fluid). The two bands represent 960 $cm^{-1}$ (phosphate) and 1660 $cm^{-1}$ (amide I).

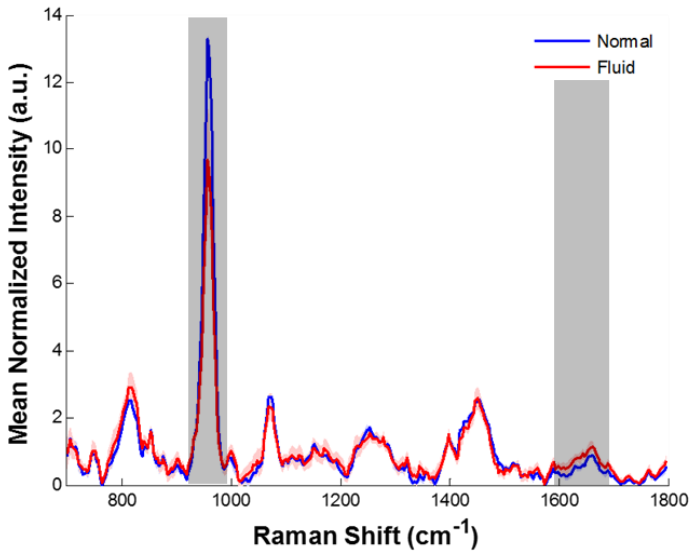


Figure A1.24: Mean-normalized ± standard deviation Raman spectra of in vivo measurements of the TM comparing normal (no MEE) versus the presence of fluid (MEE). Gray bands highlight visual differences between the two categories.

## A1.5 Discussion

The development of an image-guided fiber-optic Raman probe is important for guiding the user to collect biochemical information of desired locations in the ear canal to characterize the presence or absence of otitis media. To accomplish this, the placement of fibers for illumination, imaging, Raman excitation, and Raman scattered detection is critical to optimize the use of this tool. One design criteria is for the outer diameter of the bundled image-guided fiber-optic Raman probe is to fit inside of the patient's ear canal. This design constraint inhibits the use of large imaging detects for Raman scattered light to be included in the probe, which would increase the diameter of the probe. The number of illumination fibers, imaging geometry, and Raman collection fibers in a tight space is critical not to compromise the signal to noise ratio (SNR). Appendix I describes the first stages of exploration within our lab group to investigate these design challenges and characterize Raman measurements of patients suffering from otitis media.

The newly designed 7 x 500 µm illumination fibers and imaging geometry of 6,000 elements with a 270 µm total diameter are coupled with a 300 µm 785 nm excitation source and 6 x 300 µm Raman collection fibers. These elements fit into a 4 mm (outer diameter) Raman probe. An illumination source in the lab was coupled with a long-pass filter to minimize ultraviolet (UV) light to reach the fiber tip. An imaging system with a series of optics available in the lab was designed to focus the light collected by the imaging bundle on a Thorlabs detector. Software by Thorlabs was used to collect live video from imaging on a laptop and guide Raman measurements. After illumination of a sample and placement of the Raman

probe was determined to be accurate, an image was collected and the illumination source was turned off to not interfere with Raman excitation and collection.

The initial optical design for imaging and Raman measurements that was designed and built allowed for initial testing in the lab and in the operating on patients affected by otitis media. Raman spectra collected of acetaminophen, one of the standards utilized in a portable Raman spectroscopy system, compares the old probe (1 x 400 µm Raman excitation fiber and 7 x 300 µm Raman collection fibers) and newly designed probe as described above (Figure A1.25). The Raman spectra are comparable in intensity (non-normalized) and Raman shifts. However, when Raman spectra are collected *in vivo* from acute otitis media patients, the spectral intensity differences are clear (Figure A1.26). The intensity of the non-normalized Raman spectra is three times as intense for some Raman peaks (~1050 $cm^{-1}$ and ~1660 $cm^{-1}$) and six times as intense in another peak (~800 $cm^{-1}$) for the old Raman probe compared to the new image-guided Raman probe. As was found with imaging the Raman collection fibers when illuminated with a NeAr light source, only four of the six Raman collection fibers can efficiently collect Raman scattered light. This design issue was further confirmed after determining the Raman collection fibers on each end of the semicircle may have been incorrectly epoxied when built. This would have inhibited Raman scattered light to be collected into the two fibers, therefore decreasing the Raman signal intensity as seen in the *in vivo* Raman spectra (Figure A1.26). Furthermore, this would increase the exposure time needed during measurements to have a SNR compatible for accurately characterizing biochemical information from the desired

location on the sample. The increase in measurement time is not ideal for a tool planning to be implemented in a clinic or operating room where time is critical.

While the first prototype design of an image-guided RS probe for characterization of otitis media has a design issue centered on Raman collection, it is a first step towards guiding the user to visualize where Raman measurements are being collected from in an environment that makes it challenging to do so. As previously discussed, the placement of Raman probe is critical to accurately record measurements of the tympanic membrane and other areas of interest for characterization of otitis media. The second-generation prototype of this Raman probe design may include a more robust illumination design and a minimum of six Raman collection fibers in a circular design configuration to minimize angular dependence of Raman scattered light. Additionally, a more sensitive detector may be included to increase the resolution of the imaging field. These changes combined may lead to a more optimal design and implementation for a Raman probe geared towards investigating patients suffering from otitis media.

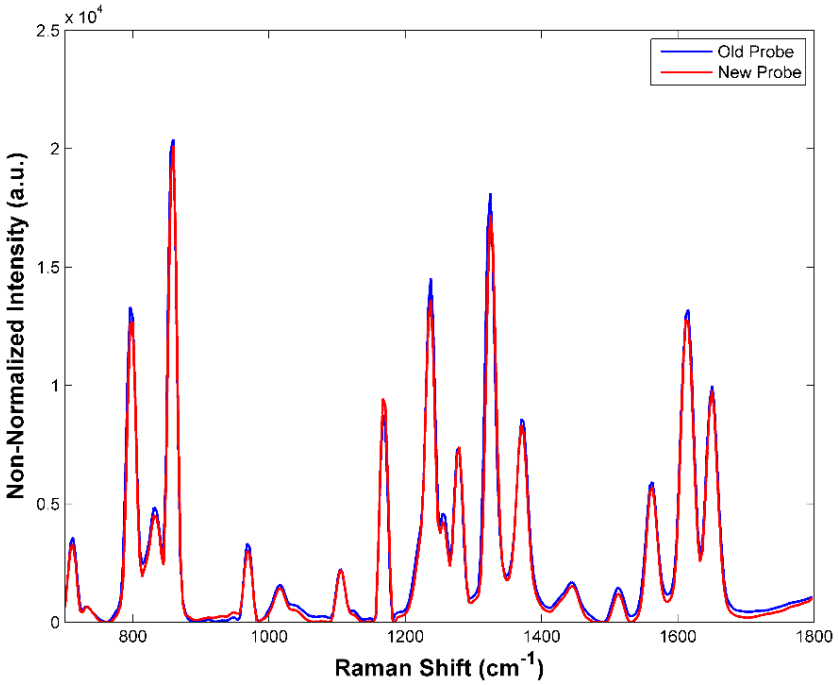


Figure A1.25: Non-normalized ± standard deviation Raman spectra of acetaminophen. Raman measurements were collected to compare spectra from an old Raman probe design and new image-guided Raman probe.

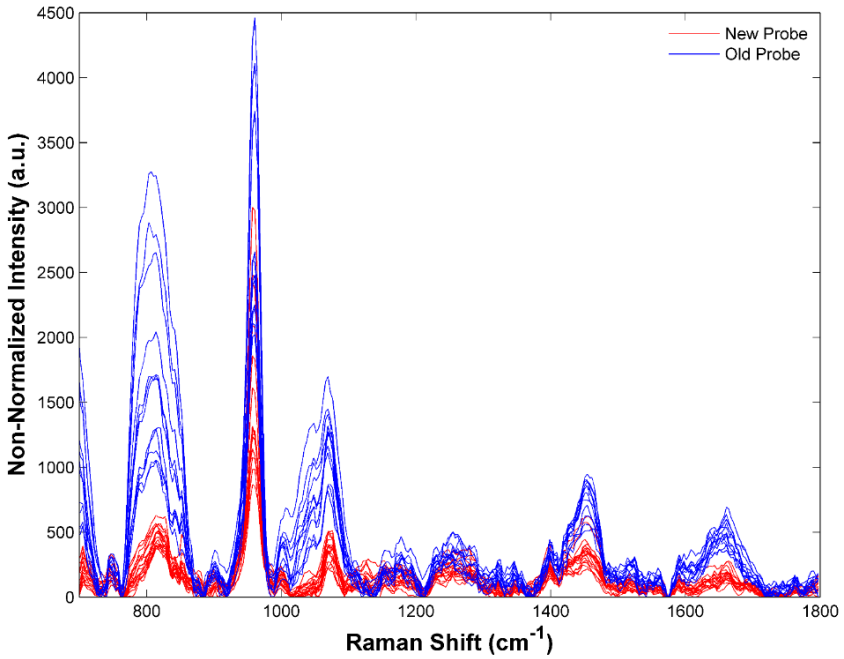


Figure A1.26: Non-normalized Raman spectra of the tympanic membrane from patients affected by acute otitis media measured in vivo. Raman measurements were collected to compare spectra from an old Raman probe design and new image-guided Raman probe.